

Surface Plasmon-Assisted Nanolithography on Silicon

by

Fenglin Liu

A thesis submitted in partial fulfillment of the requirements for the degree of

Doctor of Philosophy

Department of Chemistry

University of Alberta

© Fenglin Liu, 2016

## **Abstract**

Nanoscale lithography on silicon is of interest for applications ranging from computer chip design to tissue interfacing. Block copolymer-based self-assembly, also called directed self-assembly (DSA) within the semiconductor industry, can produce a variety of complex nanopatterns on silicon, but these polymeric films typically require transformation into functional materials.

The fabrication of plasmonic stamps is demonstrated, which is an optically transparent flexible PDMS stamps with patterned gold hemispheroids that were produced via block copolymer self-assembly on silicon surfaces. Gold salt metallization and subsequent plasma treatment of solvent annealed block copolymers led to the gold nanopatterns on flat silicon surfaces. With sequential steps of precursor spin-coating, curing, and peeling off of the PDMS layer, a plasmonic stamp with embedded ordered gold hemispheroid arrays can be obtained. By varying the molecular weight of the block copolymer templates, controllable size and spacings of Au nanopatterns in the plasmonic stamp can be captured.

By using these plasmonic stamps, direct functionalization of silicon surfaces can be achieved via hydrosilylation of selected 1-alkenes or 1-alkynes on a sub-100 nm scale, leading to nanopattern transfer from self-assembled block copolymer templates to the 1-alkyl or 1-alkenyl molecular patterns on flat silicon surfaces. The molecular patterns were captured by AFM, and can be further visualized by surface

modification involving thiol-ene chemistry to obtain thiol-terminated patterns, followed by attachment of gold nanoparticles or gold electroless deposition in the thiol-terminated regions.

In terms of energy exchange between metals and semiconductors, there are a number of ways to complete the energy transfer in radiative or non-radiative manners. Based on the mechanistic discussions and results on simulation and Au-Si distance studies, we propose that the intense electric near-field that results from the localized surface plasmons resonance of the gold nanoparticles in the plasmonic stamps upon illumination with green light, leads to generation of electron-hole pairs in the silicon that drive spatially-localized hydrosilylation. Free charge carrier impact ionization, induced by the electric field of the local plasmons of the gold nanohemispheroids is proposed to explain the role of doping. This approach demonstrates how localized surface plasmons can be used to enable functionalization of technologically relevant surfaces with nanoscale control, implying the potential applications for direct imaging intense electric fields in the plasmonic nanostructures.

## Preface

Chapter 1 provides a brief overview of the two emerging topics related to the plasmonic stamp lithography: surface nanolithography and surface plasmon resonance (SPR) of the plasmonic metal nanoparticles. Chapter 2 introduces the fabrication of plasmonic stamps containing patterned gold nanopatterns derived from block copolymer self-assembly, as well as the characterization and challenges for the plasmonic stamp. Chapters 3 and 4 describe the plasmonic stamping on flat silicon surfaces, with different foci. The chemistry and scope for the plasmonic stamping with several selected organic molecules are investigated in Chapter 3, in addition to the stamp recycling, and methods for molecule pattern visualization on a stamped surface. Chapter 4 focuses on the investigations of the possible mechanisms taking place in the stamping system, including plasmonic scattering, hot carrier injection, plasmonic heating, as well as the plasmon induced resonant energy transfer (PIRET) pathway. Chapter 5 summarizes the work in this thesis, and proposes several research directions to explore with respect to the applications for and mechanisms of the plasmonic stamp assisted lithography.

Chapters 2 and 3 are based on the publication “Nanoscale Plasmonic Stamp Lithography on Silicon” in *ACS Nano* 2015, volume 9, issue 2, pages 2184-2193, with authors Fenglin Liu, Erik J. Luber, Lawrence A. Huck, Brian C. Olsen, and Jillian M. Buriak. Lawrence A. Huck and Jillian M. Buriak proposed ideas, and I

performed experiments and wrote the first draft, and the final manuscript was written with contributions of all authors. All authors have given approval to the final version of the manuscript.

Chapter 4 is based on a submitted paper to *Chemistry of Materials*, with co-authors Jillian M. Buriak, Tate C. Hauger, Erik J. Luber, and Brian C. Olsen. I performed the experiments and wrote the first draft, and the final manuscript was written with contributions from all authors.

## Acknowledgements

Foremost, I would like to express my special appreciation to my supervisor, Dr. Jillian Buriak, for giving me the opportunity pursuing my Ph.D. degree in her lab, as well as her direction throughout these five years. She has been always interested in my research, and I would not be able to complete my research and finish my thesis without her encouragement and guidance. She is a tremendous mentor for me in both science and daily life in Canada. I am really grateful for her patience, motivation, and enthusiasm, making me become better and stronger.

I would like to thank my committee members, Dr. Mark McDermott, Dr. Eric Rivard, and Dr. Ken Cadien for their valuable advice and help during my Ph.D. studies. I am very grateful to Dr. Anna Ritcey from Université Laval for agreeing to be my external committee member for my thesis defence.

For the past five years, I have constantly received help and advice from my excellent colleagues in the Buriak Group. A special thanks to Dr. Hidenori Mizuno for the pioneering work on the catalytic stamps. I would like to thank Dr. Erik Lubber, Tate Hauger, Dr. Lawrence Huck, Brian Olsen and Minjia Hu for their collaboration and suggestions, as well as their contributions to my papers and thesis. I would like to thank other lab members, Dr. Bing Cao, Cong Jin, Jennifer Ozdoba, Kelli Lubber, Dr. Binbin Yu, Dr. Lei Chen, Chris Fatterly, Hezhen Xie, Chengcheng Rao, and Mahmoud Almadhoun for the support and friendship. I would also like to express

my acknowledgement to the former Buriak lab members that I have worked with, Dr. Ken Harris, Dr. Jeremy Bau, Shuai Chen, Dr. Nathanael Wu, Dr. Brian Worfolk, Sharon Saunders, Dr. Xiaojiang Zhang, Dr. Gang He, Dr. Xiaoming He, Dr. Qun Chen, Dr. Tonggang Jiu, Dr. Hosnay Mobarok, and Dr. Ibrahim Al-Rafia, for helping me start and fit in the lab and life in Edmonton. I would also like to thank Dr. Anqiang He, Scott Munro, Dr. Peng Li from nanoFAB in the University of Alberta, and Dr. Kai Cui, Dr. Mike Xia, Paul Concepcion in NINT for facility training and characterization assistance. My special thanks go to Dr. Jeremy Bau and Kelli Luber for help revising this thesis.

I would like to express my appreciation to Alberta Innovates Technology Futures (AITF), Alberta Recruitment Graduate Student Scholarship, and China Scholarship Council (CSC) for the financial support throughout my Ph.D. studies.

A special thanks to my family. I am grateful to my parents for their sacrifices and unwavering support as always. I also would like to thank my wife Junhua and my daughter Anna for their love, accompany and encouragement.

# Table of Contents

Abstract

Preface

Acknowledgement

List of Tables

List of Figures

List of Abbreviations

<b>1 General Introduction</b>	<b>1</b>
1.1 Overview	1
1.2 Current Nanolithography Techniques on Surface	3
1.2.1 “Top-down” Lithography	4
1.2.2 “Bottom-up” Lithography	12
1.3 Introduction to Plasmonics	18
1.3.1 Surface Plasmons	18
1.3.2 Plasmonics for Enhanced Solar Energy Conversion	20
1.4 Scope of the Thesis	28
<b>2 Plasmonic Stamp Lithography I: Fabrication</b>	<b>31</b>
2.1 Introduction	31

2.1.1 The Basics of Block Copolymers .....	32
2.1.2 Block Copolymer Lithography .....	34
2.2 Results and discussion .....	41
2.2.1 Synthesis of Gold Nanopatterns .....	41
2.2.2 Fabrication of Plasmonic Stamps .....	44
2.2.3 Characterization of Plasmonic Stamps .....	46
2.3 Conclusions .....	50
2.4 Experimental Section .....	50
<b>3 Plasmonic Stamp Lithography II: Chemistry and Scope .....</b>	<b>54</b>
3.1 Introduction .....	54
3.2 Hydrosilylation on Hydride-terminated Silicon Surfaces .....	55
3.2.1 Surface Hydrosilylation without Incident Light .....	55
3.2.2 UV light Induced Surface Hydrosilylation .....	56
3.2.3 Visible Light Induced Surface Hydrosilylation .....	59
3.3 Results and Discussion .....	62
3.3.1 Plasmonic Stamping of Alkenes on Silicon .....	64
3.3.2 Plasmonic Stamping of Alkynes on Silicon .....	69

3.3.3 Pattern Visualization for the Stamped Molecules on Silicon .....	72
3.3.4 Recycling of Plasmonic Stamps .....	76
3.4 Conclusions .....	77
3.5 Experimental Section .....	78
<b>4 Plasmonic Stamp Lithography III: Mechanisms .....</b>	<b>81</b>
4.1 Introduction .....	81
4.2 Conventional Energy Transfer Mechanisms .....	82
4.2.1 Light Scattering .....	84
4.2.2 Hot Carrier Injection .....	86
4.2.3 Plasmonic Heating .....	87
4.2.4 Plasmon Induced Resonant Energy Transfer .....	88
4.3 Results and Discussion .....	90
4.3.1 Discussion of Plasmonic Scattering Mechanisms .....	91
4.3.2 Discussion of Plasmonic Heating Mechanism .....	92
4.3.3 Discussion of Hot Carrier Injection Mechanism .....	95
4.3.4 Proposed Mechanism for the Plasmonic Stamping .....	97
4.3.5 Simulation .....	99

4.3.6 Ferrocene Quenching .....	101
4.3.7 Au-Si Distance Studies .....	102
4.3.8 Doping Effects of Substrates .....	106
4.4 Conclusions .....	112
4.5 Experimental Section .....	112
<b>5 Summary and Outlook .....</b>	<b>116</b>
5.1 Summary of Chapters .....	117
5.2 Proposed Research Directions .....	119
5.2.1 Plasmonic Structure in Photovoltaics .....	119
5.2.2 Variation of Sizes of Au Nanopatterns .....	122
5.2.3 Variation of Shapes of Au Nanopatterns .....	124
5.2.4 Variation of Orders of Au Nanopatterns .....	126
5.2.5 Extension to Other Noble Metals .....	127
<b>References .....</b>	<b>129</b>

## List of Tables

- Table 2.1.** Schemes and examples of typical block copolymers
- Table 3.1.** Statistics of center-to-center spacings of nanopatterns during stamping process.
- Table 3.2.** Water contact angles of the 1-alkyne stamped Si(111)-H surfaces under various conditions
- Table 4.1.** Contact angle measurements of hydrosilylated silicon surface with and without the quenching agent addition.
- Table 4.2.** Contact angle measurements of hydride-terminated silicon substrates stamped with thiol-modified plasmonic stamps.

## List of Figures

- Figure 1.1.** Applications of nanopatterning on surfaces. a) Ordered silicon hole arrays for optical devices. b) Precise site control of Au nanopatterns in nanofluidic channels. Scale bar: 1  $\mu\text{m}$ . c) Patterned PDMS cylinders via directed block copolymer self-assembly. Scale bars: 50 nm. d) Phonic devices with complex nanopatterns of semiconductors.
- Figure 1.2.** Scheme of bottom-up approach versus top-down approach in nanofabrication.
- Figure 1.3.** Schematic illustration for the formation of patterned silicon substrates with positive and negative photoresists via photolithography.
- Figure 1.4.** Schematic illustration for the formation of Au nanopatterns on silicon using electron-beam lithography.
- Figure 1.5.** Scheme of four variations in scanning probe lithography: a) Dip-pen nanolithography; b) nanografting; c) constructive nanolithography; and d) scanning near-field lithography.
- Figure 1.6.** Schematic illustration of large-scale substrate conformal imprint lithography (SCIL).
- Figure 1.7.** Scheme of an ideal self-assembled monolayer of thiolates on Au(111) surface.

- Figure 1.8.** a) Block copolymer self-assembly on flat and on confined surfaces.  
b) Directed block copolymer self-assembly on the silicon nanopillar patterned substrate.
- Figure 1.9.** Binary superlattices of FePt-Fe<sub>3</sub>O<sub>4</sub> via the self-assembly of monodispersed FePt and Fe<sub>3</sub>O<sub>4</sub> nanoparticles.
- Figure 1.10.** Overview of properties of surface plasmon resonance. SPR peaks vary with different types of metals a), shapes b) and sizes c), and distribute heterogeneously with the geometry of the metal nanostructures (d and e).
- Figure 1.11.** Schematic illustration of photovoltaic architectures incorporated with plasmonic nanostructures.
- Figure 1.12.** a) Scheme of plasmonic nanostructures in photovoltaics. Au@Ag core-shell nanoparticles or Au nanoparticles were incorporated in the PEDOT:PSS layer of the polymer:PC<sub>70</sub>BM system. b) J-V curve for two photoactive polymers: PTB7 and PCDTBT. c) Enhancement with density of Au@Ag core-shell particles.
- Figure 1.13.** Plasmonic Ag@SiO<sub>2</sub> core-shell nanostructures for enhanced electron-hole pair generation.
- Figure 1.14.** Plasmonic local heating leads to the generation of water steam at Au nanoparticle surface.
- Figure 1.15.** Plasmonic photothermal therapy for enhanced assembled gold nanovesicles for clearance of tumor issues.

- Figure 2.1.** Morphologies of block copolymer self-assembly with the increase of volume fraction of block A.
- Figure 2.2.** SEM images of various types of metal nanowires that are obtained from self-assembly of PS-*b*-P2VP (32 k-12.5 k) on flat silicon surface.
- Figure 2.3.** Order SiO<sub>x</sub> nanopatterns of parallel lines a) and hexagonal dots b) from self-assembly of PS-*b*-PDMS, with the variation of double and triple density of the patterns.
- Figure 2.4.** Schematic illustration of directed BCP self-assembly, and the SEM images of the obtained Pt nanolines via graphoepitaxy.
- Figure 2.5.** Scheme of the patterned nanohole formation using the self-assembled BCP film of PS-*b*-P4VP (109 k-27 k) as an etch stop.
- Figure 2.6.** Schematic illustrations of catalytic stamp fabrication and the stamping process on a hydride terminated silicon surface.
- Figure 2.7.** Scheme of a typical procedure for the fabrication of Au nanopatterns on silicon surfaces via block copolymer self-assembly.
- Figure 2.8.** SEM images of gold nanopatterns on silicon surfaces. Scale bar: 400 nm. BCPs: PS-*b*-P2VP (125 k-*b*-58.5 k), PS-*b*-P2VP (91 k-*b*-105 k), and PS-*b*-P2VP (190 k-*b*-190 k)

- Figure 2.9.** AFM height micrographs of gold nanopatterns on silicon surfaces with controlled spacings. BCPs: PS-*b*-P2VP (125 k-*b*-58.5 k), PS-*b*-P2VP (91 k-*b*-105 k), and PS-*b*-P2VP (190 k-*b*-190 k)
- Figure 2.10.** Self-assembled BCP film with oxygen plasma treatment time: 5 s for a), 10 s for b), 30 s for c), and 1 min for d). Scale bar: 200 nm. BCP: PS-*b*-P4VP (20 k-*b*-19 k)
- Figure 2.11.** Scheme of a typical procedure for the fabrication of a plasmonic stamp
- Figure 2.12.** Photographs of the important steps necessary for preparing the plasmonic stamps.
- Figure 2.13.** Optical photograph and UV-vis spectrum of a plasmonic stamp.
- Figure 2.14.** AFM height micrographs of plasmonic stamps with controlled spacings. Scale bar 400 nm. BCP: PS-*b*-P2VP (125 k-*b*-58.5 k) PS-*b*-P2VP (91 k-*b*-105 k) PS-*b*-P2VP (190 k-*b*-190 k)
- Figure 2.15.** Survey scan a) and high resolution b) XPS spectra of a plasmonic stamp.
- Figure 2.16.** Comparison of AFM height micrographs and corresponding height profile of Au nanopatterns on silicon surface a) and a plasmonic stamp b). BCP: PS-*b*-P2VP (125 k-*b*-58.5 k)
- Figure 2.17.** Figure 2.17 Tilted SEM image of patterned gold hemispheroids on Si/SiO<sub>x</sub> substrate. Cross-section SEM image in the inset showed the flatness of the underneath surface of a single gold hemispheroid.

Scale bars: 100 nm, and 20 nm for inset. BCP: PS-*b*-P2VP (125 k-*b*-58.5 k)

- Figure 3.1.** Scheme of hydrosilylation of different types of molecules on Si(111)-H surface.
- Figure 3.2.** Scheme of radical-based hydrosilylation on Si(111)-H surface.
- Figure 3.3.** Scheme of electron photoemission mechanism for UV-induced hydrosilylation on flat, hydride-terminated silicon surfaces.
- Figure 3.4.** Scheme of exciton based mechanism for the white light promoted hydrosilylation on porous silicon surface in the presence of R-X as an electron acceptor.
- Figure 3.5.** Mechanistic scheme of the gold nanoparticle mediated hydrosilylation on flat Si(111)-H surface.
- Figure 3.6.** Scheme of a typical procedure for plasmonic stamping on Si(111)-H surfaces.
- Figure 3.7.** Photograph of the experimental setup for plasmonic stamping.
- Figure 3.8.** Schematic outline of the hydrosilylation chemistry on flat Si(111)-H surfaces with two typical 1-alkenes used for plasmonic stamping.
- Figure 3.9.** AFM height micrograph and corresponding height profile of 1-dodecene stamped Si(111)-H surface. BCP: PS-*b*-P2VP (125 k-*b*-58.5 k)

- Figure 3.10.** AFM height micrographs of 1-dodecene stamped Si(111)-H surfaces with variation of illumination time. BCP: PS-*b*-P2VP (125 k-*b*-58.5 k)
- Figure 3.11.** AFM height micrographs of 1-dodecene stamped Si(111)-H surfaces with controlled spacings. BCPs: PS-*b*-P2VP (125 k-*b*-58.5 k) PS-*b*-P4VP(20 k-*b*-19 k) PS-*b*-P2VP (91 k-*b*-105 k) PS-*b*-P2VP (190 k-*b*-190 k)
- Figure 3.12.** AFM height micrographs and XPS spectra of 1H,1H,2H-perfluoro-1-decene on silicon surfaces with variation of illumination time. BCP: PS-*b*-P2VP (125 k-*b*-58.5 k)
- Figure 3.13.** Water contact angles of the 1-alkene stamped Si(111)-H surfaces under various conditions.
- Figure 3.14.** Schematic outline of the hydrosilylation chemistry on flat Si(111)-H surfaces with selected 1-alkynes used for plasmonic stamping.
- Figure 3.15.** AFM height micrographs and XPS spectra of 1-alkyne-stamped Si(111)-H surfaces after plasmonic stamping under various conditions.
- Figure 3.16.** Outline of pattern visualization via citrate-capped gold nanoparticles
- Figure 3.17.** SEM images of an of the patterned silicon surface before and after exposure to ~10 nm Au nanoparticles. SEM scale bar: 100 nm.

- Figure 3.18.** Schematic outline of pattern visualization via gold electroless deposition
- Figure 3.19.** SEM and AFM images of the patterned silicon surface after electroless gold deposition. Scale bars: 200 nm for a,b), and 20 nm for c).
- Figure 3.20.** XPS spectra of S (2p) after thiol-ene chemistry and Au (4f) after final Au deposition
- Figure 3.21.** a: Scheme of recycling process of plasmonic stamps. Prior to the next stamping, the stamp was soaked in dichloromethane for three times and then washed in hexane for at least 6 hours. b-d: AFM height micrographs of 1-dodecene stamped nanopatterns on Si(111)-H surfaces with recycled plasmonic stamps. Scale bar: 400 nm. BCP: PS-*b*-P2VP (125 k-*b*-58.5 k)
- Figure 4.1.** Various mechanisms for energy transfer between metals and semiconductors.
- Figure 4.2.** Schematic geometries of light scattering for applications in photovoltaics and photocatalysis.
- Figure 4.3.** Energy diagram for water splitting via the hot carrier injection mechanism. CB: conduction band. VB: valence band. SP: surface plasmon.
- Figure 4.4.** Photo excitation and relaxation process of SPR induced hot carriers.

- Figure 4.5.** a) Plasmon-induced resonant energy transfer (PIRET). The plasmon is excited and its energy transfers from the metal to the conduction band of the semiconductor. b) Photocatalytic activity is enhanced by PIRET from Au to Cu<sub>2</sub>O.
- Figure 4.6.** a) Calculated cross-section coefficient scattering/absorption ratio of Au nanoparticles. b) Calculated spectra of scattering (black), absorption (red) and total extinction (green) of a gold nanosphere with 20 nm in diameter.
- Figure 4.7.** a-b): SEM images of Au nanopatterns with spacings of a) 200 nm and b) 400 nm. c,e,g) Experimental and d,f,h) FDTD simulation of plasmonic heating and delocalization.
- Figure 4.8.** Macroscale temperature measurements. a) Scheme of the temperature measurement setup. b) Temperature profile observed with increase of illumination time. (Band pass filter: CW526, 50 mW/cm<sup>2</sup>). The thermocouple was sandwiched between plasmonic stamp and silicon surface as per the described experimental procedure
- Figure 4.9.** Scheme of the possible carrier injection mechanism.
- Figure 4.10.** a) Energy transfer between gold and semiconductor via plasmon-induced resonant energy transfer (PIRET) adopted from ref. 1. In the diagram, plasmons excited from gold hemispheroids and transferred the energy to the hydride terminated silicon via dipole-

dipole coupling. b) Schematic mechanism of plasmonic stamp-assisted hydrosilylation via PIRET.

**Figure 4.11.** AFM height maps of stamped Si(111)-H surfaces using band-pass filters with different wavelength ranges (CW 526, 50 mW/cm<sup>2</sup> and CW 440, 40 mW/cm<sup>2</sup>). The block copolymer used for the stamp was PS-*b*-P2VP (125 k-*b*-58.5 k). Scale bar is 200 nm.

**Figure 4.12.** a) AFM height micrographs of 1-dodecyl patterned Si(111)-H surface after plasmonic stamping; b) Zoomed-in AFM height micrograph shows ring-like dodecyl patterns on Si(111)-H surfaces. BCP: PS-*b*-P4VP (20 k-*b*-19 k) Scale bars: 200 nm for a); 20 nm for b). c, d) FDTD simulations of a single gold hemispheroids (20 nm in diameter) from top and side views.

**Figure 4.13.** a) UV-vis spectra of the stamps clamped between two glass slips before and after the addition of Rhodamine B. b) Absorbance of Rhodamine B, calculated from their UV-vis spectra.

**Figure 4.14.** Distance dependence of the plasmonic stamping

**Figure 4.15.** Scheme and plots of water contact angle measurements of 1-dodecene (black) and 1H,1H,2H-perfluoro-1-decene (blue) stamped Si(111)-H surfaces with alkanethiol (C<sub>n</sub>H<sub>2n+1</sub>SH) treated plasmonic stamps. Monolayers of ethanethiol, 1-butanethiol, 1-hexanethiol, 1-dodecanethiol and 1-hexadecanethiol was attached to the Au surface in the plasmonic stamp prior to the stamping, n = 0 indicates control experiments without thiol treatment.

- Figure 4.16.** Water contact angle measurements of 1-alkene stamped silicon surfaces with different doping levels (++: highly doped)
- Figure 4.17.** AFM height micrographs of 1H,1H,2H-perfluoro-1-decene stamped silicon surfaces with various doping concentrations.
- Figure 4.18.** Schematic mechanism of plasmonic hole generation in silicon via free charge carrier impact ionization.
- Figure 4.19.** a) Absorption coefficient of hydrogen terminated (111) oriented silicon with various doping types and densities. b) Cosine of ellipsometric phase shift for pseudo-hexagonal arrays of Au dots on (111) oriented silicon substrates of various doping densities (solid lines), and corresponding bare silicon substrates (dotted lines)
- Figure 5.1.** Schematic representation of Light trapping by: a) Forward scattering, and b) Local enhancement of electromagnetic field via LSPR
- Figure 5.2.** SEM images of plain ITO a) and ITO glasses with gold nanopatterns. BCP: PS-*b*-P2VP (20 k-*b*-19 k). Scale bar: 100 nm
- Figure 5.3.** UV-vis spectroscopy of a) gold nanoparticles with different sizes on glass substrates, and b) PEDOT:PSS layer with and without gold nanoparticles.
- Figure 5.4.** Enlargement of gold nanoparticles by varying the concentration of metal ions. BCP: PS-*b*-P2VP (20 k-*b*-19 k). Scale bar: 50 nm

- Figure 5.5.** Schematic illustrations and corresponding SEM images of nanoparticle enlargement process. BCP: PS-*b*-P2VP (20 k-*b*-19 k). Scale bar: 50 nm.
- Figure 5.6.** SEM images of polystyrene spheres ( $D=0.4\ \mu\text{m}$ ) and patterned gold nanotriangles ( $a=100\ \text{nm}$ ) after gold evaporation and template removal. Scale bar:  $1\ \mu\text{m}$ .
- Figure 5.7.** SEM images and transmission spectra of an infinite a) and periodic b) Au nanopatterns. c) FDTD simulations show the charge distributions of the lattice plasmons.
- Figure 5.8.** Ordered nanopatterns with different metals from the block copolymer PS-*b*-P4VP (20 k-*b*-19 k). Scale bar: 200 nm

## List of Abbreviations

AFM	Atomic force microscope
aq.	Aqueous
BCP	Block copolymer
BNSL	Binary nanocrystal superlattices
CA	Contact angles
CB	Conduction band
CW	Center wavelength
DEG	Diethylene glycol
DSA	Directed self-assembly
EHP	Electron-hole pairs
FDTD	Finite-difference time-domain
FRET	Forster resonant energy transfer
FWHM	Full width at half-max
HSQ	Hydrogen silsesquioxane
IR	Infrared
ITO	Indium tin oxide
LSPR	Localized surface plasmon resonance
NIR	Near-infrared
NP	Nanoparticle

PCDTBT	Poly(dimethylsiloxane)
PCX	Plano-Convex
PC <sub>70</sub> BM	[6,6]-Phenyl C71 butyric acid methyl ester
PDMS	Polydimethylsiloxane
P3HT	poly(3-hexylthiophene-2,5-diyl)
PEDOT:PSS	poly(3,4-ethylenedioxythiophene) polystyrene sulfonate
PIRET	Plasmon-induced resonant energy transfer
PS- <i>b</i> -P2VP	Polystyrene- <i>block</i> -poly-2-vinylpyridine
PS- <i>b</i> -P4VP	Polystyrene- <i>block</i> -poly-4-vinylpyridine
PS- <i>b</i> -PDMS	Polystyrene- <i>block</i> -poly(dimethylsiloxane)
PS- <i>b</i> -PMMA	Polystyrene- <i>block</i> -polymethylmethacrylate
PTB7	Poly[[4,8-bis[(2-ethylhexyl)oxy]benzo[1,2-b:4,5-b']dithiophene-2,6-diyl][3-fluoro-2-[(2-ethylhexyl)carbonyl]thieno[3,4-b]thiophenediyl]]
RCA	Radio Corporation of America
RET	Resonant energy transfer
SAM	Self-assembled monolayer
SEM	Scanning electron microscope
STM	Scanning tunneling microscope
SP	Surface plasmon

SPL	Scanning probe lithography
SPP	Surface plasmon polariton
SPR	Surface plasmon resonance
tBoc	10-N-Boc-aminodec-1-ene
TFAAD	N-(dec-9-enyl)-trifluoroacetamide
UV	Ultraviolet
VB	Valence band
XPS	X-ray photoelectron spectroscopy

# 1

## General Introduction

### 1.1 Overview

This thesis introduces a new strategy for patterning silicon surfaces with flexible, recyclable plasmonic stamps carrying gold nanopatterns that were prepared *via* block copolymer self-assembly. I will mainly focus on the preparation of plasmonic stamps, plasmonic stamping on hydride terminated silicon surfaces with selected molecules, and mechanistic studies of plasmon-induced hydrosilylation *via* plasmonic stamps, aiming to provide a clean, versatile method for transferrable nanopatterning, and expand the mechanism in the white-light promoted hydrosilylation on flat silicon surfaces.

As a general introduction to the related topics, this chapter will give a brief overview of the two main fields that are covered in the thesis, nanopatterning and nanoplasmonics. Specifically, this chapter will discuss first existing techniques for surface nanopatterning, focusing on “top-down” and “bottom-up” nanolithography, as well as the introduction of pattern transfer techniques. Then, I will give an

introduction regarding surface plasmons and the applications of nanostructured plasmonics using examples from the literature. Finally, I will discuss what role the nanoplasmonics can play in various plasmonic nanostructures, and how they affect the performance/yield *via* surface plasmons.

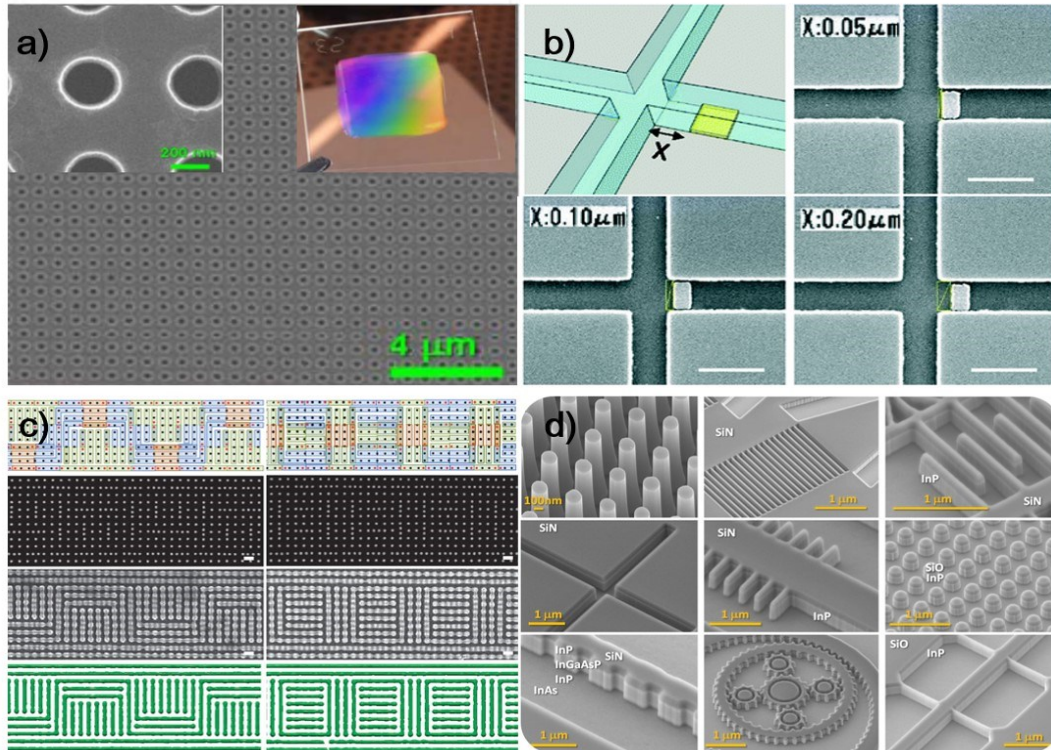


**Figure 1.1.** Applications of nanopatterning on surfaces. a) Ordered silicon hole arrays for optical devices. b) Precise site control of Au nanopatterns in nanofluidic channels. Scale bar: 1 μm. c) Patterned PDMS cylinders *via* directed block copolymer self-assembly. Scale bars: 50 nm. d) Phonic devices with complex nanopatterns of semiconductors. Reprinted with permission from ref. 2, Copyright © 2014, American Scientific Publishers, and ref.3. Copyright © 2015 RSC publishing, and from ref. 4 Copyright © 2014. Nature Publishing Group.

## 1.2 Current Nanolithography Techniques on Surfaces

The word of lithography means “stone drawing” in Greek, and was invented in the year of 1798 and used originally for cheap artwork publications.<sup>1</sup> After two hundred years of development, this technique has become one of the most expressive and efficient ways for large-scale fabrication of repeatable products. Figure 1.1 showed several examples of nanopatterning applications on semiconductor industry.<sup>2-5</sup> As for nanolithography, “top-down” and “bottom-up” are two main routes that are used to categorize the nanolithography techniques,<sup>6-10</sup> and a comparison of these two categories is shown in Figure 1.2.<sup>11</sup> In the field of nanofabrication, “top-down” route is recognized as a destructive way (i.e. remove material to make smaller structures) to build architectures in nanoscale, while *via* a “bottom-up” route, molecules or atoms are the main building blocks with which nanostructures in a constructive way are formed. In terms of driving forces, the “top-down” techniques rely on the etching of laser beams, electron beams or other physical forces that are external to the system. On the other hand, the driving forces for “bottom-up” routes usually involve intermolecular interactions (such as Columbic interaction, hydrophobic interactions, hydrogen bonding, etc. ) to build up nanoscale assemblies.<sup>9, 12</sup> Existing nanofabrication techniques have been divided into these two categories, and are briefly introduced below with examples provided of nanofabrication on surfaces.

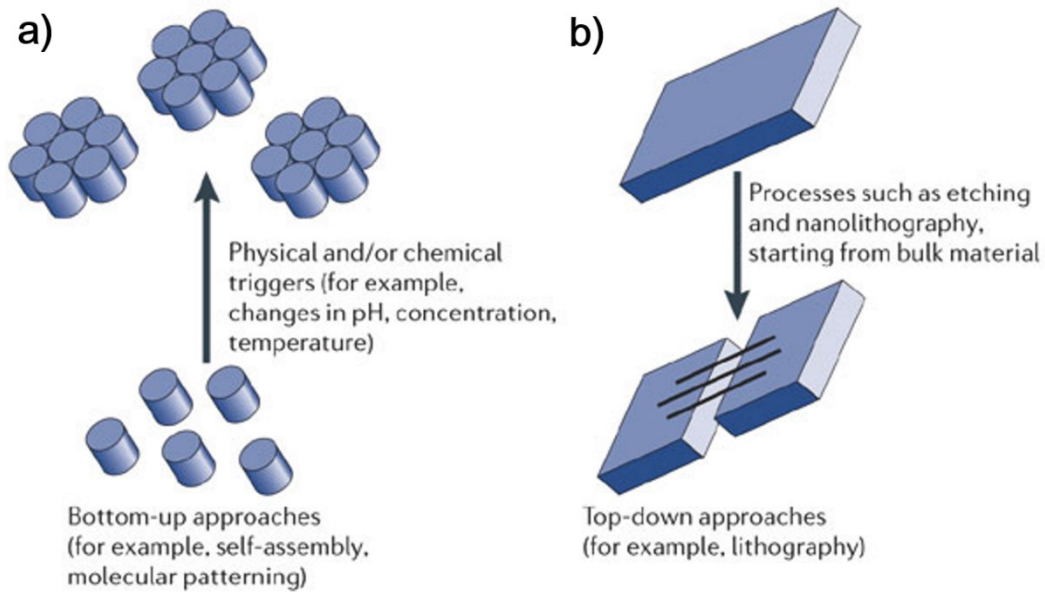


**Figure 1.2.** Scheme of a) bottom-up approach versus b) top-down approach in nanofabrication.

Reprinted from ref. 10. Copyright © 2006 Nature Publishing Group

### 1.2.1 “Top-down” Lithography

In top-down lithography, there is typically a sacrificial mask with nanopatterned features on top of the target material, and the subsequent, sequential etching steps can result in the two-dimensional nanopatterns on the material surface. Thus far, various etching methods have been used for nanofabrication on surfaces *via* top-down lithography. Categorized by their etching sources, four typical top-down lithography techniques will be discussed below, including photolithography,<sup>13-18</sup> electron beam lithography,<sup>19-23</sup> nanoimprint lithography,<sup>24-32</sup> and scanning probe lithography.<sup>33-38</sup>

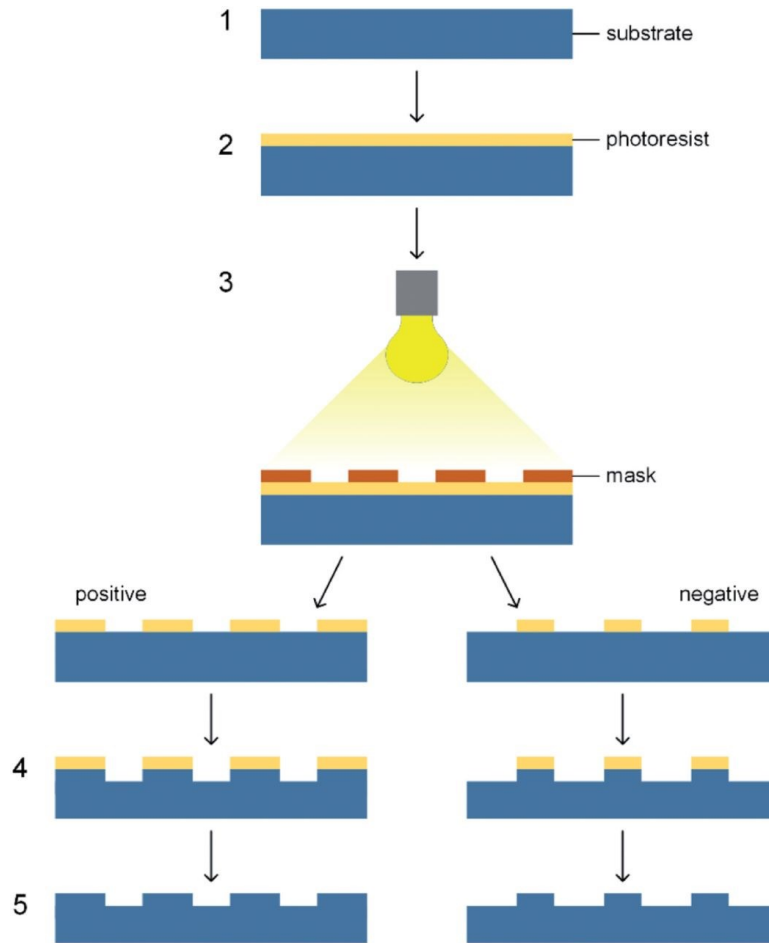


**Figure 1.3.** Schematic illustration for the formation of patterned silicon substrates with positive and negative photoresists *via* photolithography. Reprinted with permission from ref. 18.

Copyright © 2014 Oxford University Press.

### ***Photolithography***

The illumination source for photolithography is optical light or ultra-violet light, and therefore also referred to as UV lithography<sup>14, 39, 40</sup> and optical lithography.<sup>16, 41, 42</sup>

Photolithography has been applied in semiconductor industries for the fabrication of nanopatterned circuits since 1960s. In a typical photolithographic approach

shown in Figure 1.3, optical or UV light is shone through a patterned mask onto a photoresist film, resulting in the desired patterns on the photoresist-coated substrates. The following steps can be varied by either etching the exposed substrate to form the underlying patterns, or deposition of another material to form patterns after resist removal. In this strategy, the light source is one of the critical factors for micro- and nanofabrication. The wavelength of the incident light can determine the final feature size.<sup>11</sup> For example, in conventional photolithography, 400 nm incident light can give a 1 micron spatial resolution on the substrate using photography, but the resolution is not consistent across the substrate due to light diffraction and scattering.<sup>10</sup> The photoresist is another crucial factor in photolithography. As shown in Figure 1.3, typical photoresists consist of light-sensitive organic molecules or polymers that can act as “positive” or “negative” photoresists depending on their final state after photo-illumination.<sup>43, 44</sup>

In order to break the resolution limit from the conventional photolithography, many efforts have been made in the past three decades to push the spatial-resolution limit to the nanoscale for the semiconductor industry such as chip manufactures.<sup>45</sup> A spatial resolution of sub-50 nm can be achieved under the illumination of argon fluoride and fluorine laser with wavelengths of 193 nm and 157 nm.<sup>45, 46</sup> The addition of high-refractive-index liquid (such as highly purified water) between the mask and the substrate, referred to as immersion lithography, can further reduce the

resolution by a factor of 1.4 (equal to the refractive index of the liquid).<sup>47</sup> Moreover, extreme ultra-violet (EUV) lithography, considered as the next generation lithography, utilizes light sources with the wavelength range of 1~50 nm to push the theoretical resolution limit to sub-10 nm.<sup>48</sup>

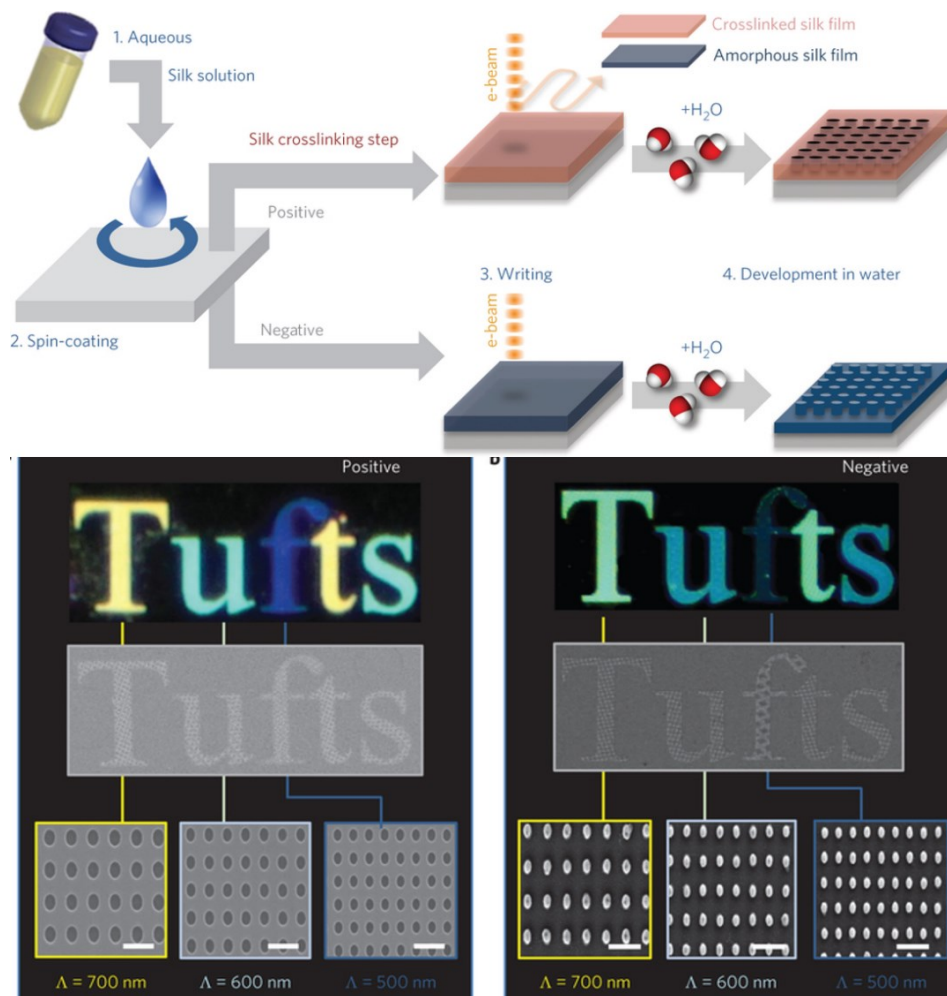


**Figure 1.4.** Schematic illustration for the water-based electron-beam lithography for photonic crystals. Reprinted with permission from ref. 50. Copyright © 2014 Nature Publishing Group.

### *Electron-Beam Lithography*

Similar to the photolithography, electron-beam lithography (or e-beam lithography) utilizes an energetic electron-beam source for nanopatterning in the nanoscale, as shown in Figure 1.4. Compared with UV light, the electron beam has much higher energy and shorter wavelengths that are capable of patterning in the nanoscale, and spatial resolution of up to several nanometers can therefore be achieved with this technique.<sup>21,49</sup> In this method, hydrogen silsesquioxane (HSQ) has been widely used as a negative resist, leading to various nanopatterns that can be written *via* e-beam lithography.<sup>49</sup> Other interesting resists such as silk was also applied with e-beam lithography and can be used as either positive or negative resist, as shown in Figure 1.4.<sup>50</sup>

Electron-beam lithography has overcome the resolution limit caused by light diffraction without masks for pattern writing on substrates, and has been applied for the fabrication of complex nanopatterns (e.g. writing nanopatterns on photomasks for photolithography).<sup>51</sup> However, compared to photolithography with a parallel process through pre-patterned masks, electron-beam lithography is a serial process with manual assistance. Therefore, this technique is a relatively low throughput technology and not suitable for large-scale manufactures.

### ***Scanning Probe Lithography***

Judging by its name, scanning probe lithography refers to lithographic techniques using sharp scanning probes for nanopatterning on surfaces.<sup>27, 29, 52</sup> It provides a versatile approach for patterning molecules or atom clusters with a spatial resolution down to 10 nm. Scanning probe lithography usually takes only one-step processing to achieve desired patterns on surfaces and operates under atmosphere or vacuum conditions, and can therefore reduce the cost for last-scale fabrication. As for the drawbacks of this method, the slower scanning rate (<10 Hz) of the probe can result in a low throughput, as there is a balance between the spatial resolution and scanning rate.<sup>10, 38</sup> Research and development on the scanning probe lithography are mainly classified into two categories: (1) the properties of the probe and the underlying substrate, and (2) interaction between the probe and the surface. The role of the probe is important as it directly impacts the spatial resolution limit. Probes from atomic force microscopy,<sup>53, 54</sup> scanning tunneling microscopy,<sup>55-58</sup> and scanning optical microscopy<sup>37</sup> have been applied for the scanning probe lithography and the variations are summarized in Figure 1.5. Interactions between the probes and substrates will vary and can involve thermal, chemical, and electrical interactions, depending on their composition and physiochemical properties. For example, with the scanning tunneling probes, Fe atoms can be physically pushed to produce the desired patterns on Cu(111) substrates.<sup>59, 60</sup> With AFM tips, molecular patterns can be written either directly on a substrate *via* dip-pen lithography,<sup>61-63</sup> or can be removed selectively *via* the nanoshaving by the tip.<sup>64, 65</sup> If connected with a carbon

nanotube at the tip, the spatial resolution can be pushed to several nanometers by the oxidation scanning probe lithography.<sup>66, 67</sup>

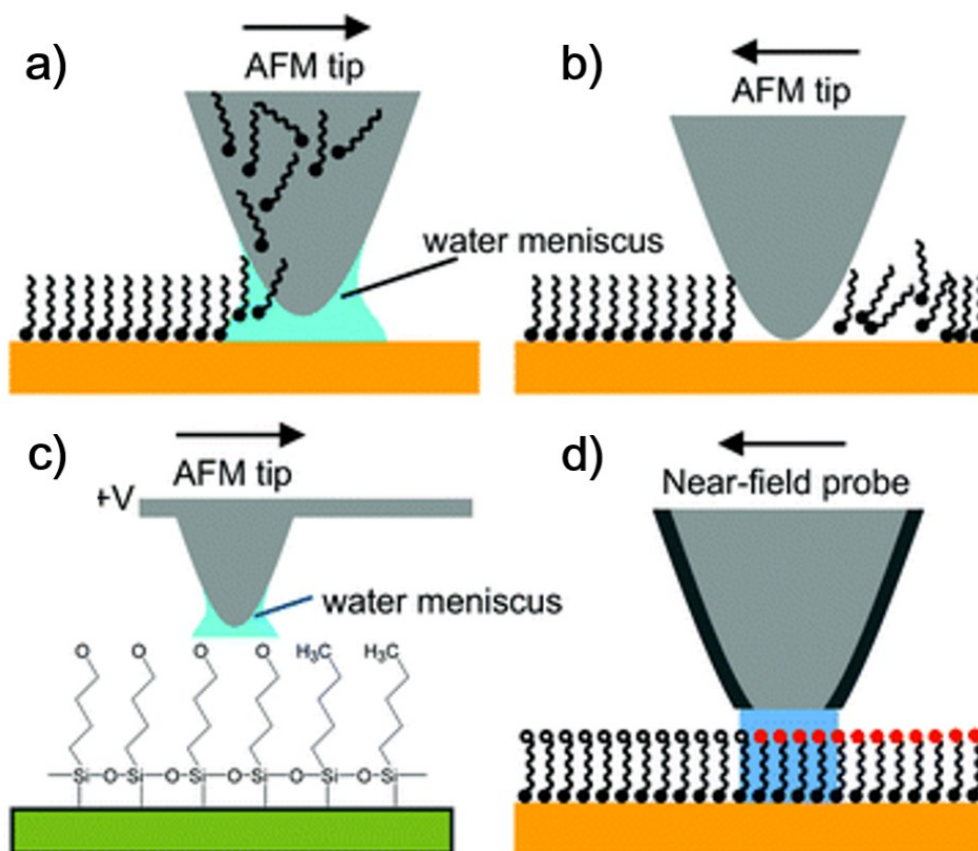


**Figure 1.5.** Scheme outlining of four variations of scanning probe lithography: a) Dip-pen nanolithography; b) nanografting; c) constructive nanolithography; and d) scanning near-field lithography. Reprinted with permission from ref. 52. Copyright © 2012. RSC Publishing.

### ***Nanoimprint Lithography***

Nanoimprint lithography has been proven to be a top-down strategy with low cost and high throughput for surface micro-/nano-fabrication.<sup>22</sup> This method starts with the fabrication of a pre-patterned, rigid mold (e.g. silicon), and the mold is then pressed against a flexible polymer film and heated above the glass transition temperature of the polymer. Finally the cooling process and the mold removal result in the pattern transfer from the mold to the film *via* mechanical deformation. As discussed above, one of the limitations for the conventional lithography techniques (such as photolithography, electron-beam lithography, etc.) is the difficulty for mass production due to expensive light sources. Nanoimprinting does not require incident light, and the patterned mold can be applied repeatedly once prepared, and can be conducted under ambient conditions. Another advantage for the nanoimprint lithography is that it avoids distortion due to beam diffraction or scattering that can occur in photo- or electron-beam lithography. Therefore the transferred nanopattern was better in terms of spatial resolution and pattern qualities. For example, a research group from HP Laboratories and MIT developed sub-10 nm nanoimprinting lithography *via* wafer bowing, as shown in Figure 1.6a. Figure 1.6b shows nanopatterns with a spatial resolution of sub-10 nm (half-pitch) on a 150 mm-diameter substrate through this method.<sup>68</sup>

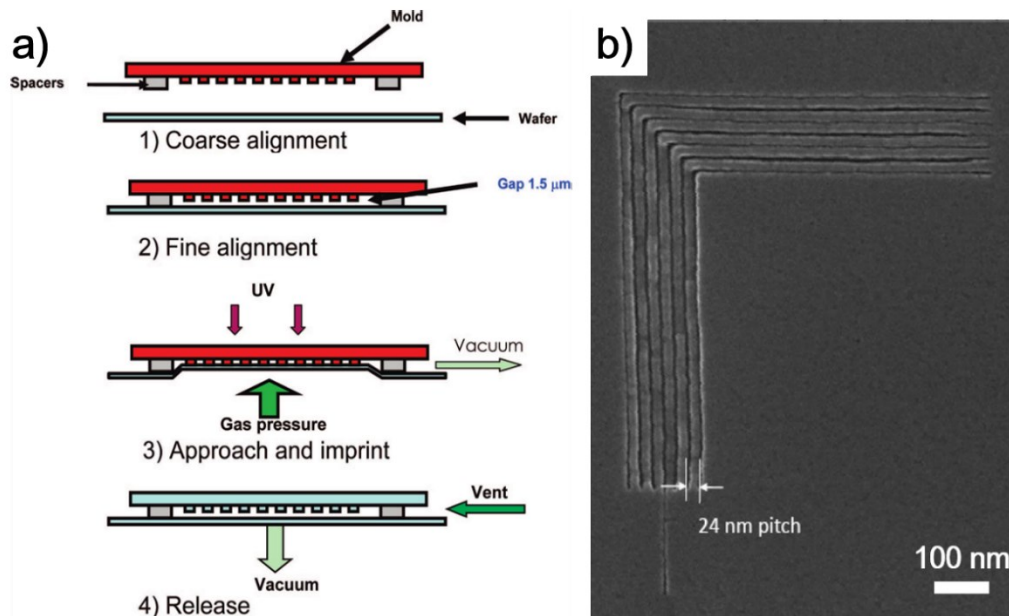


**Figure 1.6.** a) Schematic illustration and b) an SEM image of large-scale nanoimprinting work flow by wafer bowing. Reprinted with permission from ref. 68. Copyright © 2008 American Chemical Society

### 1.2.2 “Bottom-up” Lithography

Bottom-up lithography refers to a constructive fabrication strategy that can form well-ordered nanopatterns in a spontaneous, self-organized fashion.<sup>69-72</sup> The aim of the bottom-up lithography is to achieve large-scale nanofabrication through the self-assembly of molecules or nanoparticles with lower material cost. There are various ways to categorize self-assembly, for example, templated- and untemplated- self-assembly, depending on whether external forces exist in the system.<sup>10</sup> In the following, I will simply discuss the techniques of self-assembly by their building blocks, i.e. molecular/polymer self-assembly and nanoparticle self-assembly.

### ***Molecular Self-Assembly***

Molecular self-assembly<sup>73-76</sup> refers to spontaneous assembly driven by the intermolecular interactions. As molecules are the building blocks for the molecular self-assembly, high spatial resolution can be expected on surface. Due to the complexity of the molecular systems, the driving force of molecular self-assembly usually involves the cooperative effects of multiple non-covalent interactions such as Coulombic attraction/repulsion,<sup>77, 78</sup> van der Waals forces,<sup>79</sup> hydrophobic interactions,<sup>80, 81</sup> hydrogen bonding,<sup>82, 83</sup> etc. The complexity of the driving forces could be the limitation of this method as well, as it is difficult to separate and qualitatively evaluate the driving forces, and therefore it is difficult to precisely control the resulting nanostructures.<sup>84</sup>

So far, the most understood system for surface nanofabrication is based on the self-assembled monolayers (SAMs).<sup>85-87</sup> Figure 1.7 shows an example of a SAM of alkanethiolates on Au(111). To form SAMs on surface, molecules attach themselves to the surface *via* strong chemical bond formation, and then assemble together to form close-packed monolayers through weak but attractive intermolecular interactions as mentioned above. Therefore, designing functionalized molecules is a crucial step for the process. There have been various designs published, including molecules with functional terminal groups such as silanes, amines, thiols, etc.,<sup>88-90</sup> polymers<sup>91, 92</sup> or modified DNA molecules such as deoxyribozymes.<sup>93, 94</sup>

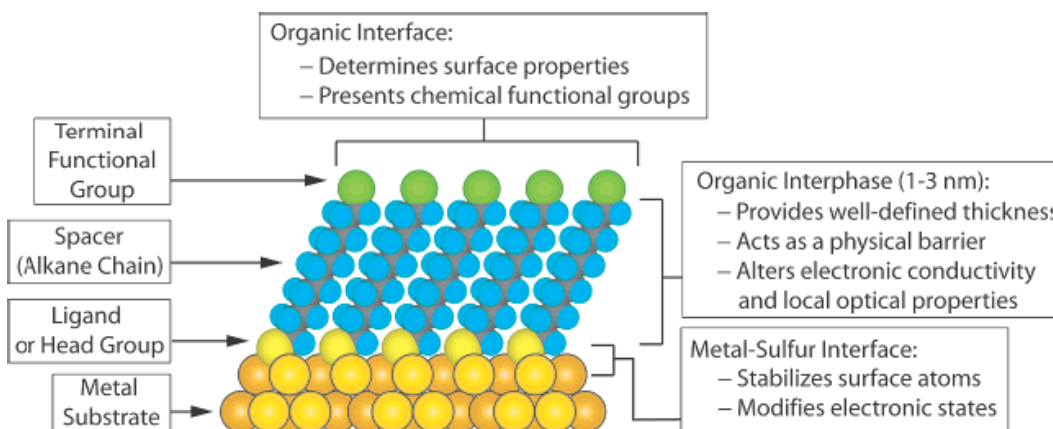


**Figure 1.7.** Scheme of an ideal self-assembled monolayer of thiolates on Au(111) surface.

Reprinted with permission from ref. 86 Copyright © 2005 American Chemical Society.

### ***Supramolecular/polymer Self-Assembly***

Similar to molecular self-assembly, supramolecular or polymer self-assembly is another versatile method and is usually conducted under mild conditions in solution and on surfaces.<sup>95-97</sup> The building blocks can range from polypeptides, DNA molecules to monomeric species including dendrimers and hybrid compounds.<sup>98-101</sup> In terms of self-assembly on surfaces, the assistance from top-down techniques (e.g. electron-beam lithography) is usually need to form long-range ordered patterned structures on surface at the nanoscale, for example, the directed self-assembly (DSA).<sup>102-105</sup> Combined with top-down and bottom-up strategies, DSA allows molecules or polymers to self-assemble on chemically patterned surfaces (referred to as epitaxial self-assembly) or on graphoepitaxy-processed surfaces (an artificial epitaxy method using physical control to guide crystallographic orientation).<sup>106</sup>

Block copolymers can self-organize to form several patterns,<sup>103, 107-109</sup> including hexagonal dots, lamellae, or parallel lines (See Chapter 2 for more detailed introduction on block copolymer self-assembly). In an example shown in Figure 1.8a, thermal annealing of a block copolymer thin film on a flat surface leads to the formation of short-range ordered fingerprint nanolines, while parallel nanolines in long-range order were observed if assembling on the confined area of the graphoepitaxy processed surface. Figure 1.8d showed another example in which self-assembled block copolymers were directed by the patterned nanopillars deposited through electron beam lithography, various two dimensional nanostructures can be achieved *via* directed block-copolymer self-assembly.<sup>110</sup>

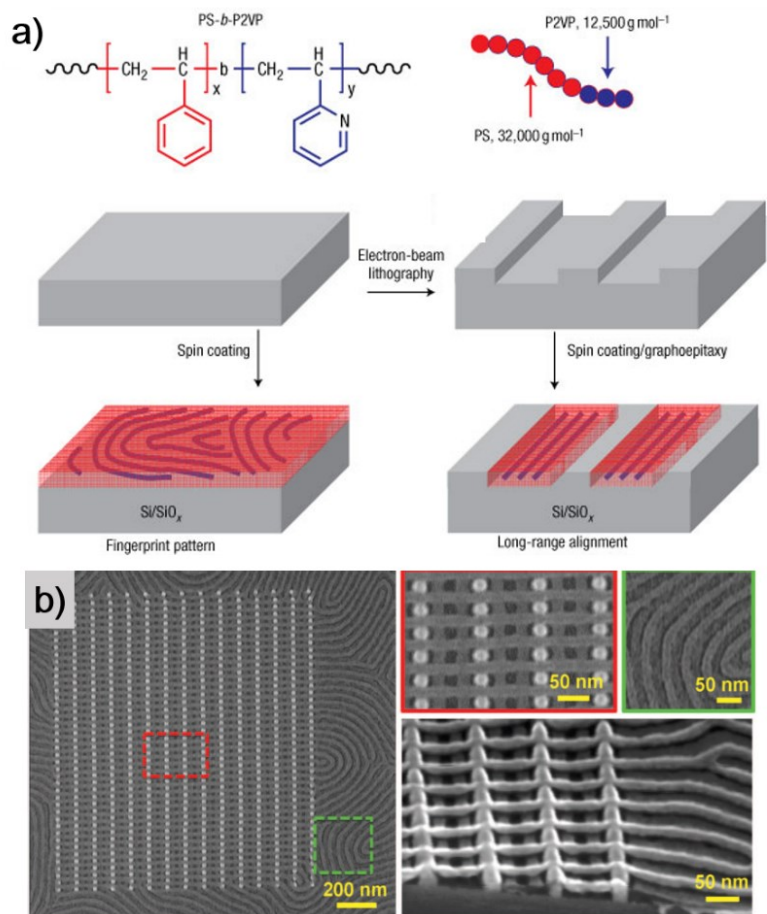


**Figure 1.8.** a) Block copolymer self-assembly on flat and on confined surfaces. b) Directed block copolymer self-assembly on the silicon nanopillar patterned substrate. Reprinted with permission from ref. 109. Copyright © 2007 Nature Publishing Group, and from ref. 110. Copyright © 2012 American Association for the Advancement of Science.

### *Nanoparticle Self-Assembly*

Ordered assemblies of uniform nanoparticles occur in nature and reveal unique mechanical and optical properties.<sup>104</sup> Similarly and inspired by nature, capping agent-passivated nanoparticles with monodisperse size and shape allow for rational

assembly into ordered superstructures in two and three dimensions such as close-packed hexagonal films, superlattices, colloid crystals, etc. In contrast to the molecular self-assembly, the monodisperse nanoparticles act as building blocks to self-organize into long-range ordered 2D films or superlattices, which is driven by interactions between nanocrystals and capillary force *via* solvent evaporation. For example, one of the most remarkable achievements in nanocrystal superlattices in last two decades is construction of multi-component superlattices, especially the binary nanocrystal superlattices (BNSLs).<sup>111, 112</sup> Assembling two different types of nanocrystals into a BNSL not only combines their properties of the each individual component, but also provides new collective properties generating from nanocrystal interactions. This provides a low-cost protocol to construct metamaterials with precisely controlled composition and properties. The Murray group developed FePt-Fe<sub>3</sub>O<sub>4</sub> binary superlattices, as showed in Figure 1.9.<sup>113</sup> In their approach, hexane was used to disperse binary nanocrystals instead of high-boiling-point solvents to allow rapid self-assembly. Colloid hexane dispersion was spread on diethylene glycol subphase (DEG) in a Teflon well, and then covered with glass slide to allow hexane evaporation. BNSL can then be obtained on the DEG subphase surface. The inert and low evaporation rate of DEG is important for the formation of centimeter-scale BNSLs. Different orientation and stoichiometry of BNSL were also obtained by simply changing the size and/or the concentration ratios between two building blocks.

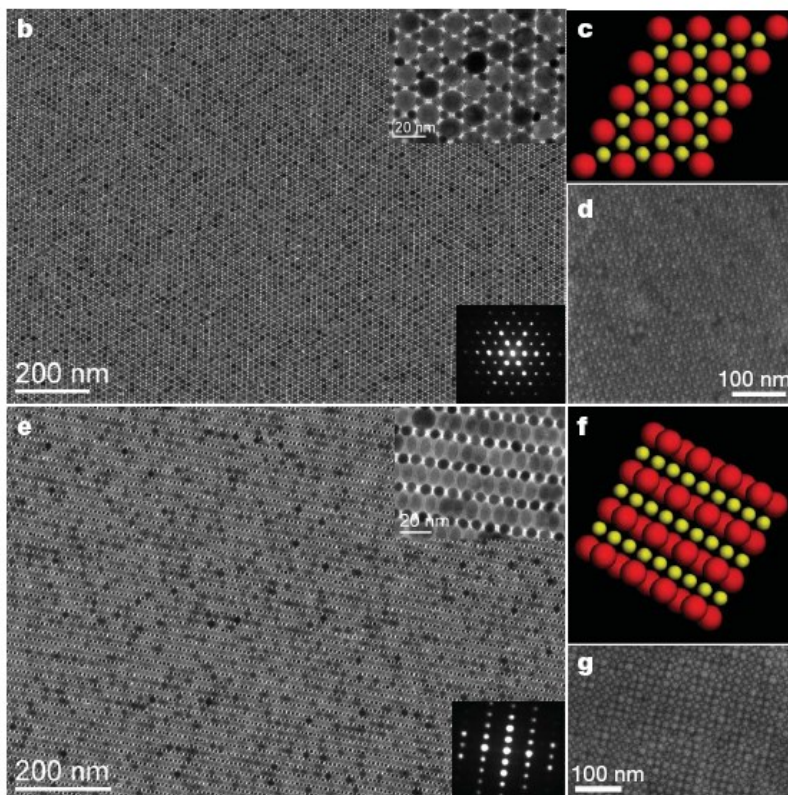


**Figure 1.9.** Binary superlattices of FePt-Fe<sub>3</sub>O<sub>4</sub> *via* the self-assembly of monodispersed FePt and Fe<sub>3</sub>O<sub>4</sub> nanoparticles. Reprinted with permission from ref. 113 Copyright ©2010 Nature Publishing Group

### 1.3 Introduction to Plasmonics

#### 1.3.1 Surface Plasmons

Surface plasmon resonance (SPR) refers to the collective oscillation of electron density at the interface of metals and dielectrics, and can be trapped as localized surface plasmons at the surface of metal nanoparticles or propagate along the metal/dielectric interface as surface polaritons.<sup>114-119</sup> Since SPR refers to the dipole-dipole coupling of photons from incident light and electrons from metal

nanoparticles, SPR peaks can be observed from UV-vis-IR spectra. Tuning the SPR peaks of noble metal nanoparticles for application purpose is of interest, as the peak positions ranges from visible to NIR, and can be controlled by sizes, shapes, geometries, and composition of the metal nanostructures, as showed in Figure 1.10 a-c.<sup>120</sup>

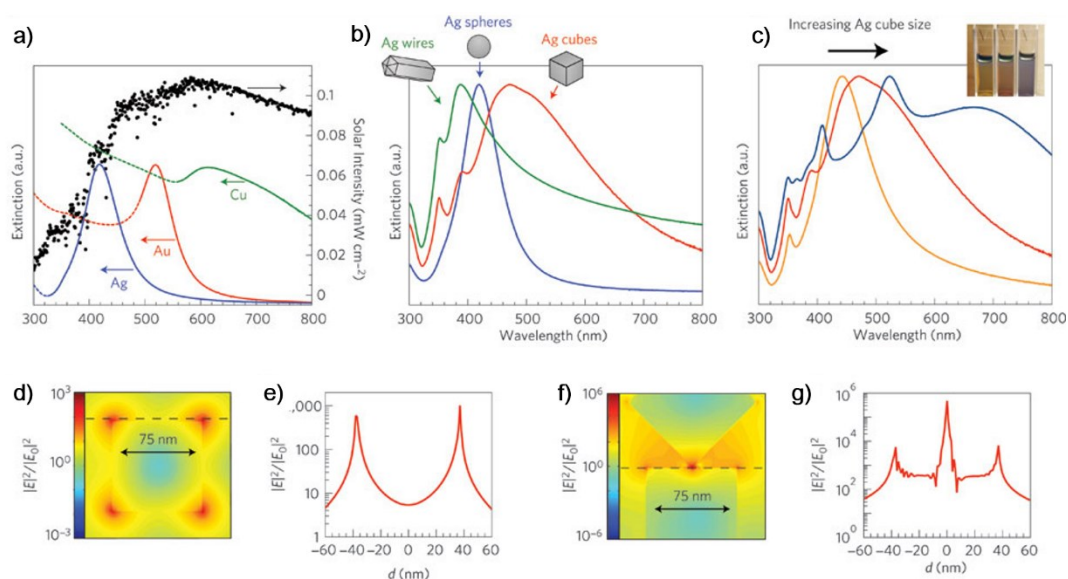


**Figure 1.10.** Overview of properties of surface plasmon resonance. SPR peaks vary with different types of metals a), shapes b) and sizes c), and distribute heterogeneously with the geometry of the metal nanostructures in d) and e). Reprinted with permission from ref. 120.

Copyright 2011 Nature Publishing Group

When the size of the metal is compatible or smaller than the wavelength of the resonant light, surface plasmons are trapped at the metal/dielectric interface and result in high intensity electric-fields (or hot spots).<sup>121-125</sup> Since the surface plasmons are trapped by the metal nanoparticles, this phenomenon is named localized surface

plasmon resonance (LSPR). The high intensity of LSPR is usually expected at gold nanoparticle sizes of 5~200 nm, and can be observed at sharp edges, corners and interstices as shown in the FDTD simulation in Figure 1.10d-g. In addition, LSPR is also sensitive to the dielectric constant of surrounding materials, and the peak intensity and position can be changed with different capping materials, as indicated in Mie theory and experimental data.<sup>120</sup>

### **1.3.2 Plasmonics for Enhanced Solar Energy Conversion**

Plasmonic metals, especially the noble metallic nanostructures, have been incorporated in many systems for enhanced energy conversion, due to their wavelength-dependent optical properties and the enhanced electric near-fields (or hot-spots). One of the reasons why the noble metals (e.g. gold, silver, copper, etc.) are attractive in the plasmonic application is that their LSPR peaks mainly overlap with the wavelength range of visible light, and therefore bring about the enhancement for solar to chemical energy conversion upon resonance.<sup>120, 126</sup> Herein, I will briefly introduce plasmonic applications in three fields: photovoltaics<sup>101-104</sup>, photocatalysis<sup>102-117</sup> (including water splitting, and CO<sub>2</sub> reduction) and photothermal therapy<sup>127-134</sup>.

#### ***SPR in Photovoltaics***

Solar energy is becoming increasingly attractive as a renewable source of energy that could augment conventional combustion of fossil fuels. Fabrication of low-cost,

high-efficiency solar cells is also the goal of the third generation photovoltaics.<sup>117, 126, 135-137</sup> In order to enhance the performance of solar cells, the efficient light absorption must be balanced with charge extraction by the photoactive layer. Increasing the film thickness of the active layer in photovoltaic devices could harvest more light absorption; however, the charge recombination would be severe due to the low diffusion length of excitons, and lead to increased series resistance.

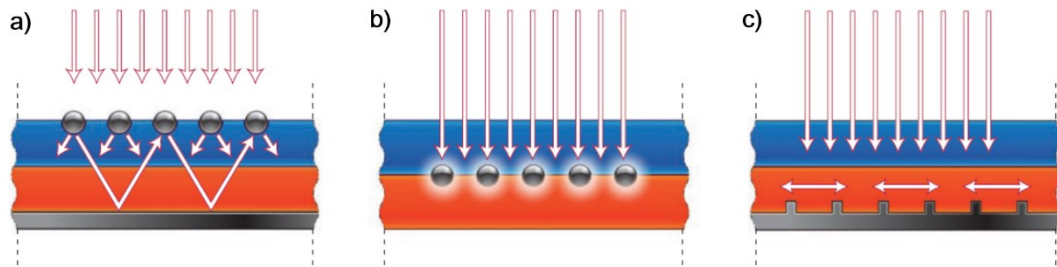


**Figure 1.11.** Schematic illustration of photovoltaic architectures incorporated with plasmonic nanostructures. Reprinted with permission from ref. 126 Copyright 2010 Nature Publishing Group

Enhanced photovoltaic performance can be achieved by incorporating the plasmonic patterns containing gold or silver nanoparticles into the interfacial or photovoltaic layers. In their review of plasmonic photovoltaic configurations and mechanisms, Atwater et.al. suggested that the enhancement was mainly due to increased light absorption arising from light scattering, enhanced energy transfer efficiency by LSPR of metal nanoparticles, and/or the existence of surface plasmon polaritons at the interface between the metal films and photoactive layers, as shown in Figure

1.11.<sup>126</sup> However, it is difficult to distinguish the mechanisms solely in one system as these mechanisms usually coexist in most systems, especially light scattering and SPR absorption. In addition, the introduction of plasmonic nanoparticles can also change the series resistance of the devices and the work functions of the layers in contact with the plasmonic nanoparticles, complicating any attempts to explain the increased efficiency in plasmonic photovoltaics. In one example shown in Figure 1.12, Au@Ag core-shell structures were incorporated into the interfacial layer of two organic solar cell systems, PTB7:PC<sub>70</sub>BM and PCDTBT:PC<sub>70</sub>BM, resulting in enhanced performance compared with the controls without plasmonic structures.<sup>138</sup> The authors attributed the enhancement to the strong scattering efficiency of Au@Ag core-shell structures that led to light trapping in the active layer, resulting in a 2.2-fold increase in external quantum efficiency with optimized particle density, as shown in Figure 1.12c.

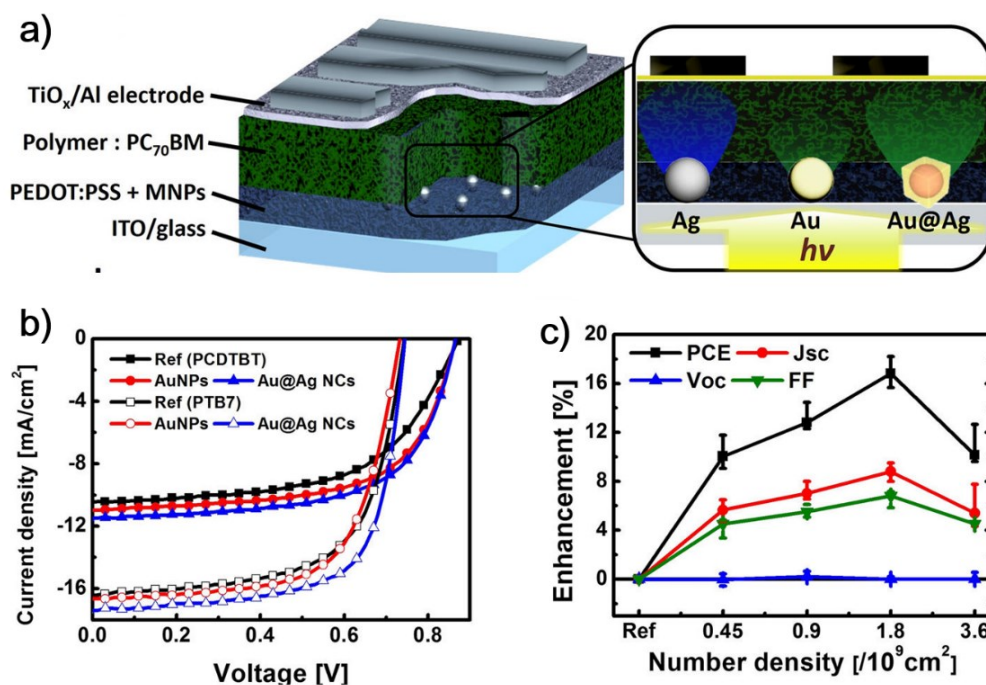


**Figure 1.12.** a) Scheme of plasmonic nanostructures in photovoltaics. Au@Ag core-shell nanoparticles or Au nanoparticles were incorporated in the PEDOT:PSS layer of the polymer:PC<sub>70</sub>BM system. b) J-V curve for two photoactive polymers: PTB7 and PCDTBT. c) Enhancement with the density of Au@Ag core-shell particles. Reprinted with permission from ref. 138. Copyright 2014 American Chemical Society.

### *SPR in Photocatalysis*

SPR of metal nanoparticles can also be applied to improve the efficiency of photocatalytic processes.<sup>102-117</sup> Different from SPR enhancement in photovoltaics, the role of SPR in photocatalysis is to store the energy in the form of chemical bonds. Both plasmon-assisted water splitting, and CO<sub>2</sub> reduction have been demonstrated.

In the application of SPR-assisted water splitting, plasmonic metal nanoparticles are usually deposited on the surface of photoactive materials such as TiO<sub>2</sub> to improve conversion efficiency under the illumination of visible light.<sup>139</sup> For example, the Cronin group reported that the gold-capped TiO<sub>2</sub> can result in up to 66-fold enhancement compared to the controlled TiO<sub>2</sub> electrode with gold, showing plasmonic enhanced water splitting for the first time.<sup>140</sup> The authors suggested that the increased efficiency was due to the LSPR-induced localized electromagnetic near-field at the interface of gold and TiO<sub>2</sub>. Surface plasmon polaritons can also lead to enhanced photocatalytic conversion when the Au/TiO<sub>2</sub> nanoparticles are replaced by Au/TiO<sub>2</sub> films. In addition, Ag nanoparticles incorporated with n-type TiO<sub>2</sub> obtained 10-fold enhancement in photocatalytic efficiency.<sup>140</sup> Figure 1.13 shows another example of plasmonic photocatalysis, in which Au/SiO<sub>2</sub> core-shell nanostructures were incorporated on top of  $\alpha$ -Fe<sub>2</sub>O<sub>3</sub>, resulting in increased exciton generation. The authors attributed the enhancement to the LSPR of Au/SiO<sub>2</sub> core-shell nanoparticles.

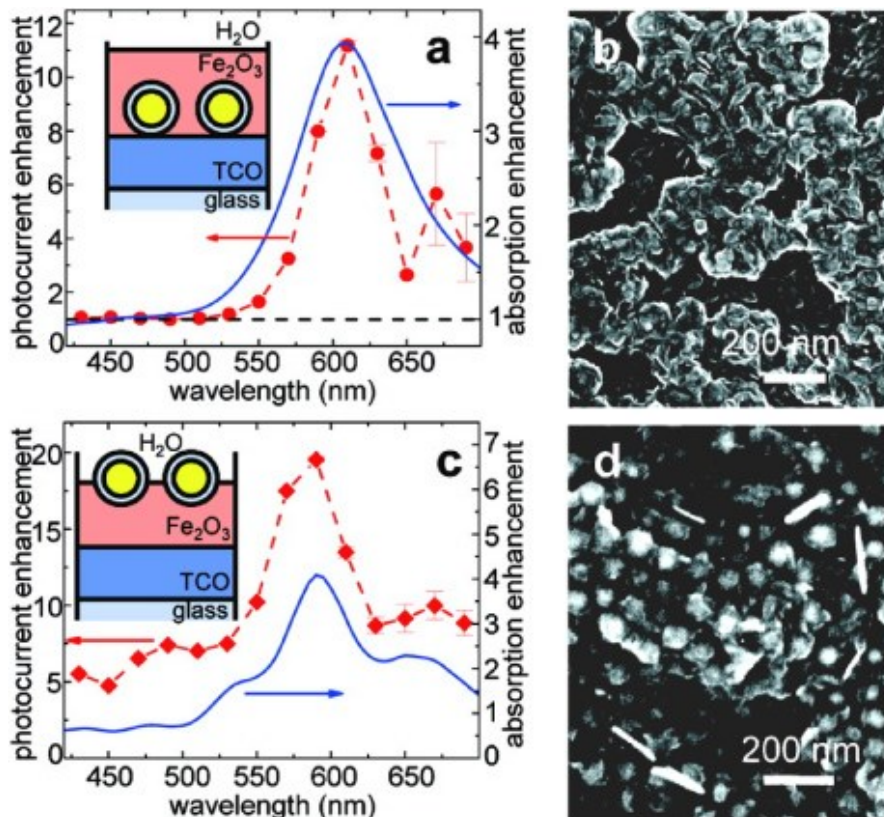


**Figure 1.13.** Plasmonic Ag@SiO<sub>2</sub> core-shell nanostructures for enhanced electron-hole pair generation. Reprinted with permission from ref.140. Copyright © 2010 American Chemical Society.

Since SPR-assisted water splitting has only been demonstrated for less than a decade, mechanisms are not fully understood. Direct charge transfer and localized electromagnetic field enhancement between metals and semiconductors are two separate mechanisms that have been suggested regarding the role played by SPR in photocatalysis. While direct charge transfer at the metal/semiconductor interface was initially accepted as the primary mechanisms of enhancement.<sup>141</sup> The enhancement of the localized electromagnetic field was also later found to

contribute to the higher conversion efficiency, even in the presence of an insulating layer.<sup>120</sup> Further studies are required in order to fully understand these mechanisms.

The reduction of CO<sub>2</sub> to methane is another hot field for solar-to-fuel energy conversion, and has the added benefit over water splitting that it can be used to reduce atmospheric CO<sub>2</sub> levels.<sup>142-144</sup> In terms of plasmonic-enhanced CO<sub>2</sub> reduction, many researchers have proved that the incorporation of plasmonic materials into photocatalysts can lead to higher efficiency of methane conversion. For example, under the illumination of visible light, Au/TiO<sub>2</sub> can be able to reach up to 24-fold enhancement for methane production without any byproducts.<sup>142</sup> The author proposed the LSPR-induced electric fields can excite electron-hole pairs in TiO<sub>2</sub> that drive the catalytic reduction of CO<sub>2</sub>. Other products such as (ethane and methanol) can be obtained by changing the wavelength of incident light, depending on the relative position of their reduction potential to the conduction band edge of the TiO<sub>2</sub>. In addition, other metals such as Pt, Cu and their bimetallic alloys have been applied for CO<sub>2</sub> reduction.<sup>145-148</sup>

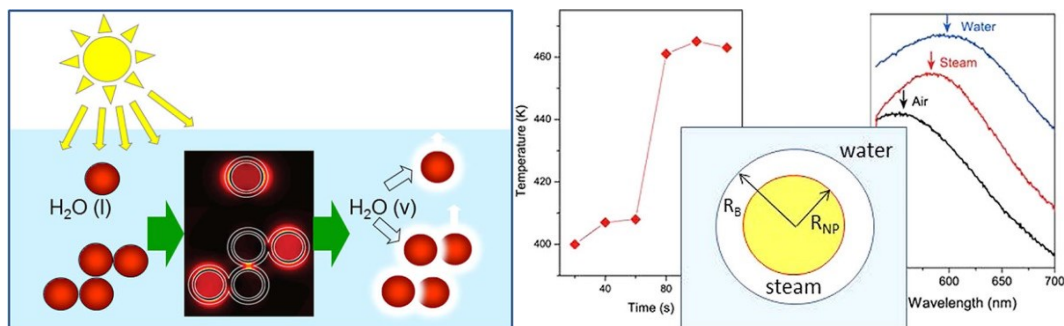


**Figure 1.14.** Plasmonic local heating leads to the generation of water steam at Au nanoparticle surface. Reprinted with permission from ref. 154. Copyright © 2013 American Chemical Society.

### ***SPR in Photothermal Therapy***

Plasmonic metal nanoparticles have also been applied in photothermal therapy.<sup>127-129, 131-134, 149-153</sup> When resonant, the plasmonic nanoparticle can heat local surroundings up to 100 °C before dissipation (Figure 1.14),<sup>154</sup> and SPR-assisted photothermal therapy utilizes this principle to generate localized heating *in vivo* by the metal nanoparticles. Compared with the previous applications, herein a more intense light source (such as pulsed lasers<sup>151-153</sup> is usually required to reach the temperature required to kill cancer cells, as well as limit the damage to the surrounding cells or tissues.<sup>132, 133</sup> Huang et.al. used self-assembled gold nanovesicles to inject to the mice body with tumor issues, and the plasmonic heating under illumination could ablate the tumor cells while keep the healthy cell intact, as shown in Figure 1.15<sup>155</sup> Because of the local temperature variation by LSPR, SPR-

assisted photothermal therapy has also been used in selective inactivation of proteins or enzymes, DNA perturbation and other targeted thermal treatment *in vivo*.

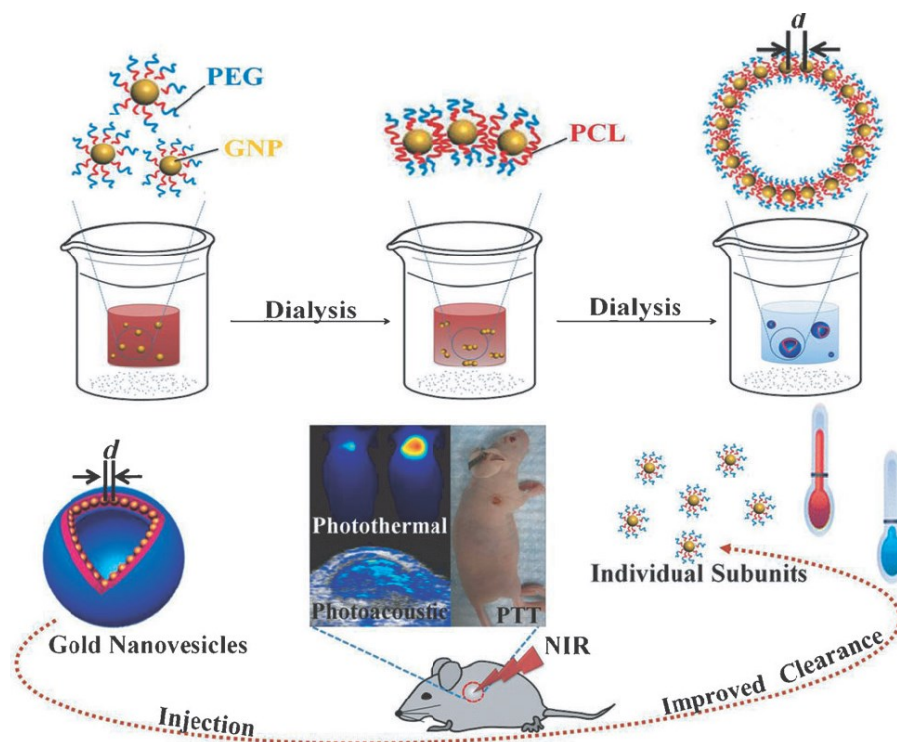


**Figure 1.15.** Plasmonic photothermal therapy for enhanced assembled gold nanovesicles for clearance of tumor issues. Reprinted with permission from ref. 155. Copyright © 2013 Wiley-VCH.

#### 1.4 Scope of the Thesis

In the following chapters of the thesis, I will discuss the topic of the surface plasmon assisted nanolithography from three aspects: (1) Plasmonic stamp fabrication; (2) Chemistry associated with the plasmonic stamp nanolithography; (3) Mechanisms of the plasmonic stamp nanolithography.

Starting in Chapter 2, I will first introduce the fabrication of the plasmonic stamp, an optically transparent flexible PDMS stamp carrying gold nanopatterns that is produced *via* block copolymer self-assembly. Ordered gold hemispheroid arrays can be obtained after gold salt metallization and subsequent plasma treatment of solvent annealed block copolymers. By varying the molecular weight of the block copolymer templates, controllable size and spacings of Au nanopatterns in the plasmonic stamp can be achieved and can be captured by atomic force microscopy.

Chapter 3 will describe how the plasmonic stamps are used to directly functionalize silicon surfaces on a sub-100 nm scale *via* the hydrosilylation of 1-alkenes or 1-alkynes, leading to the nanopattern transfer from self-assembled block copolymer templates to the 1-alkyl or 1-alkenyl molecular patterns on flat silicon surfaces. With further surface modification *via* thiol-ene chemistry, these molecular nanopatterns can be visualized *via* selective attachment of gold nanoparticles or gold electroless deposition in the thiol-terminated areas.

In Chapter 4, a number of mechanisms will be discussed that can possibly exist in our system. Based on the experimental data and mechanistic discussion, it is proposed that the high intensity electric fields that result from the localized surface plasmons of the gold nanoparticles in the plasmonic stamps upon illumination with low intensity green light, leads to generation of electron-hole pairs in the silicon that drive spatially localized hydrosilylation.

Chapter 5 will give a summary of the thesis and future applications and directions of the plasmonic nanostructures.

# 2

## Plasmonic Stamp Lithography I: Fabrication

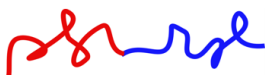
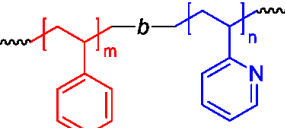
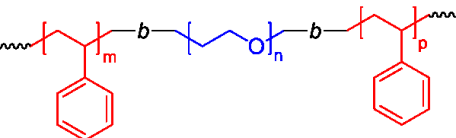
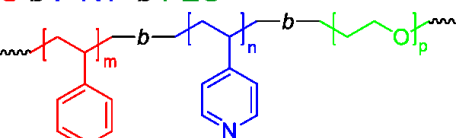
### 2.1 Introduction

This chapter will be focused on the fabrication of plasmonic stamps. In this thesis, flexible and optical transparent PDMS stamps with embedded ordered gold nanopatterns that are derived from block copolymer self-assembly are described.<sup>156</sup>

In this chapter, the nanopatterns of gold nanoparticles were obtained from the block copolymer template on flat silicon surfaces, and then embedded within from the PDMS stamp. Through this soft nanolithography process, the resulting nanopatterns from the self-assembled block copolymers were transferred to the stamp. In the introductory part of this chapter, I will provide an overview of the basics of block copolymer assembly, as well as their lithographic applications that use block copolymer self-assembly. As plasmonic stamps are obtained from the self-assembly of block copolymers, a review of block copolymer self-assembly on flat surfaces will be discussed, with highlights describing the published work in our group.<sup>109, 156-</sup>

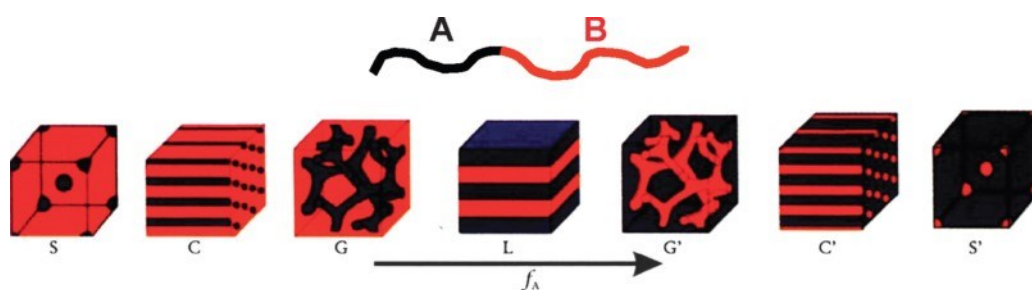
## 2.1.1 The Basics of Block Copolymers

Table 2.1 Schemes and examples of typical block copolymers

Types of block copolymers		Examples
Diblock copolymers	<b>AB type</b> 	<b>PS-<i>b</i>-P2VP</b> 
	<b>ABA type</b> 	<b>PS-<i>b</i>-PEO-<i>b</i>-PS</b> 
Triblock copolymers	<b>ABC type</b> 	<b>PS-<i>b</i>-P4VP-<i>b</i>-PEO</b> 

In general, block copolymers consist of two or more chemical chains (referred to as blocks, examples shown in Table 2.1) that are connected by covalent bonds.<sup>108, 168-170</sup> Since the blocks in the block copolymer are usually designed to be immiscible, the microphase separation of block copolymers can lead to the spontaneous formation of various micro-/nanostructures in bulk solution and on the surface, with morphologies that include spheres, cylinders, lamellae, etc., as shown in Figure 2.1.<sup>171</sup> Taking the diblock copolymer polystyrene-block-polyvinylpyridine (PS-*b*-P2VP) as an example, there are three factors that determine the final morphology of the block copolymer at equilibrium, including the (1) volume fraction of PS and P2VP; (2) the degree of polymerization,  $N$ ; and (3) their Flory-Huggins parameter,

that describes the incompatibility of the PS and P2VP blocks.<sup>171, 172</sup> The volume fractions can determine the types of nanostructures that result, as shown in Figure 2.1, and the product of the latter two parameters is commonly used to determine the degree of the microphase separation that is closely related to the center-to-center spacings in the formed nanopatterns.<sup>108, 173-176</sup> As various structures can be obtained from BCP self-assembly with nanoscale feature sizes, and their morphologies can be controlled by tuning the molecular weight, composition and assembling conditions (temperature, solvent, in bulk or on surface), block copolymer self-assembly has become a promising field for applications, including block copolymer lithography *via* the self-assembly of block copolymers.<sup>12, 166, 170, 177-184</sup>



**Figure 2.1.** Morphologies of block copolymer self-assembly with the increase of volume fraction of block A. Reprinted with permission from ref. 78. Copyright © 2012 Royal Society of Chemistry

### 2.1.2 Block Copolymer Lithography

Nanopatterned surfaces are of central importance to a variety of areas and applications,<sup>185</sup> such as computer chip architectures,<sup>29</sup> tissue interfacing,<sup>186</sup> biosensors,<sup>187</sup> light management and plasmonics<sup>188</sup> among others. As discussed in Chapter 1, the various approaches to nanopatterning are broken into two major classes: top-down methods such as photolithography,<sup>16, 189</sup> e-beam lithography<sup>49, 190</sup> and scanning force microscopy variants,<sup>10, 191</sup> and bottom-up synthetic techniques, including self-assembly.<sup>181, 192, 193</sup> Since lithography is the single most expensive step in computer chip manufacturing, the use of self-assembled block copolymers (BCPs) templates on surfaces is being seriously considered by the semiconductor industry to pattern, sub-20 nm features on a semiconductor surface; the Industry Technology Roadmap for Semiconductors (ITRS) terms this development ‘directed self-assembly’, or DSA.<sup>194</sup> Thanks to the enormous amount of work devoted to BCP-based lithography over the past two decades,<sup>195-197</sup> there is a plethora of patterns and morphologies that can be obtained, ranging from self-assembled BCP-derived nanostructures such as hexagonally packed dots,<sup>198</sup> lamellae<sup>199, 200</sup> and cylinders,<sup>201</sup> to the highly complex and long-range ordered bends,<sup>178</sup> triangles<sup>165</sup> and junctions.<sup>110</sup> Examples of the previous work from Buriak group will be discussed in the following to reveal the applications of BCP self-assembly.

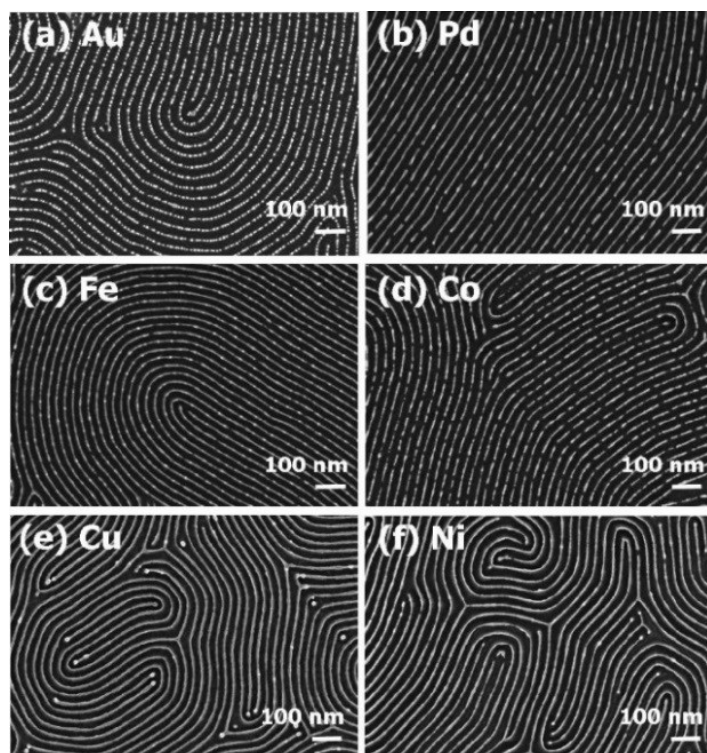


**Figure 2.2.** SEM images of various types of metal nanowires that are obtained from self-assembly of PS-*b*-P2VP (32 k-12.5 k) on flat silicon surface. Reprinted with permission from ref. 165. Copyright © 2008 American Chemical Society.

BCP-based films are compatible with existing silicon-based lithography, due to the central role played by organic photoresists that are handled in much the same manner.<sup>202, 203</sup> As is the case with photoresists, the nanostructured BCP films must typically still be translated or converted into a functional material, or used directly as a removable etch stop.<sup>204</sup> For instance, metal nanopatterns can be converted by loading polystyrene-*block*-polyvinylpyridine films with metal ions, and then treated with plasma to remove the BCP, and simultaneously reduce the metal ions to metal nanostructures.<sup>109, 165, 166</sup> For example, in the earlier work of our group, different

compositions of ordered metal nanowires have been obtained by loading the corresponding metal ions in the annealed BCP films, including gold, platinum, palladium, iron, cobalt, cobalt, nickel, etc., as indicated in Figure 2.2.<sup>165</sup>

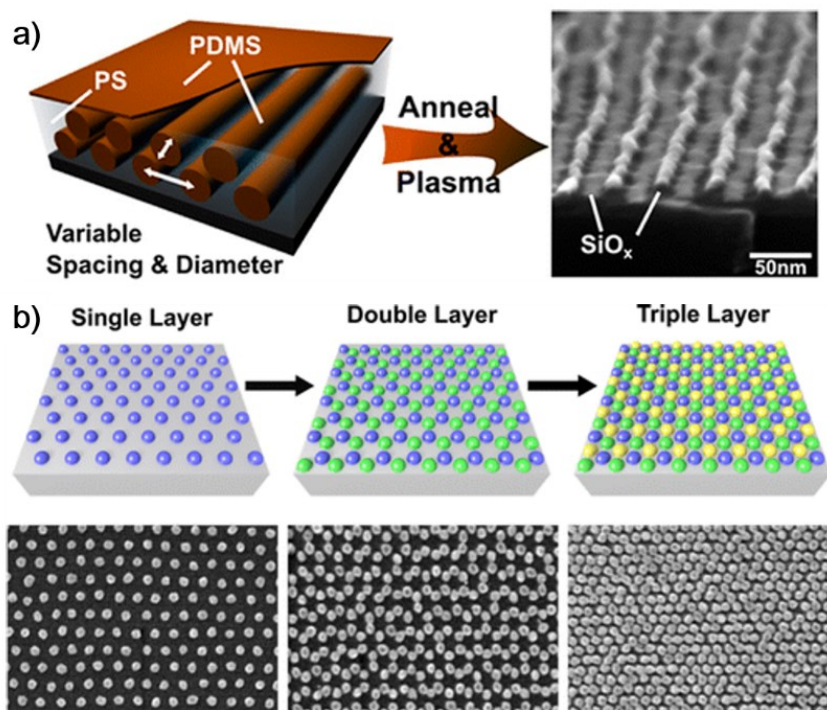


**Figure 2.3.** Order SiO<sub>x</sub> nanopatterns of parallel lines a) and hexagonal dots b) from self-assembly of PS-*b*-PDMS, with the variation of double and triple density of the patterns. Reprinted with permission from ref. 159. Copyright © 2012 and ref. 157 Copyright © 2016 American Chemical Society.

Complex nanopatterned silica structures can be obtained directly *via* plasma treatment of annealed polystyrene-*block*-polydimethylsiloxane (PS-*b*-PDMS) BCP films.<sup>157, 158, 205</sup> No further metallization step is required to view the assembled nanopatterns in hexagonal dots or parallel lines as the PDMS can be reduced directly

into SiO<sub>x</sub> after O<sub>2</sub> plasma. Interestingly, the spatial resolution can be brought down to sub-20 nm when density doubled and tripled nanopatterns are fabricated from the self-assembly of PS-*b*-PDMS, by solvent annealing a thicker PCP thin film (Figure 2.3a) and/or applying the sequential self-assembly process (Figure 2.3b).<sup>165</sup>

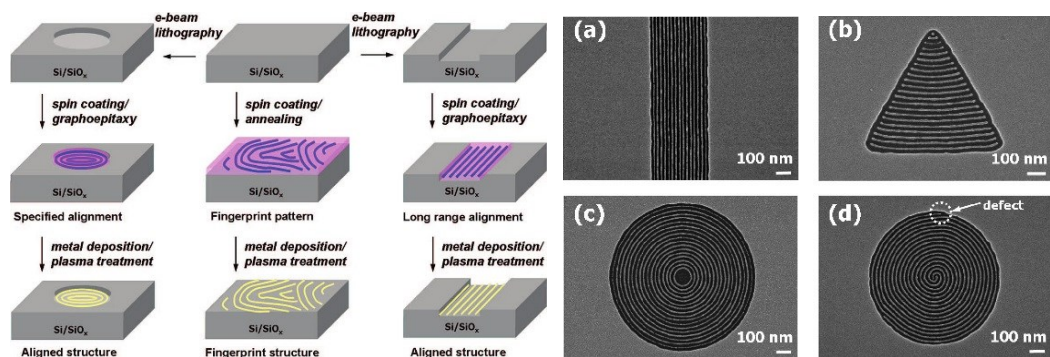


**Figure 2.4** Schematic illustration of directed BCP self-assembly, and the SEM images of the obtained Pt nanolines *via* graphoepitaxy. Reprinted with permission from ref. 165. Copyright © 2008 American Chemical Society.

In general, block copolymers can self-assemble to form ordered nanolines upon solvent or thermal annealing in a large scale, but they are usually randomly aligned over the surface of the flat substrate, as shown in Figure 2.2. With the approach of directed self-assembly that is mentioned in Chapter 1, block copolymers can self-assemble into desired patterns with long-range order.<sup>103, 178, 206</sup> As indicated in Figure 2.4, combined with electron-beam lithography to form different shapes of regions on the silicon surface, the BCP self-assembly can be directed *via* graphoepitaxy on the surface to form the long-range ordered nanolines in

rectangular, triangular, and spherical channels.<sup>165</sup> With the combination of the top-down lithography with the bottom-up BCP self-assembly, the directed self-assembly can avoid the respective limitations (e.g. the slow and expensive fabrication process for the e-beam lithography, and the lack of long-range order *via* BCP self-assembly), and applied potentially for large-scale manufacture.

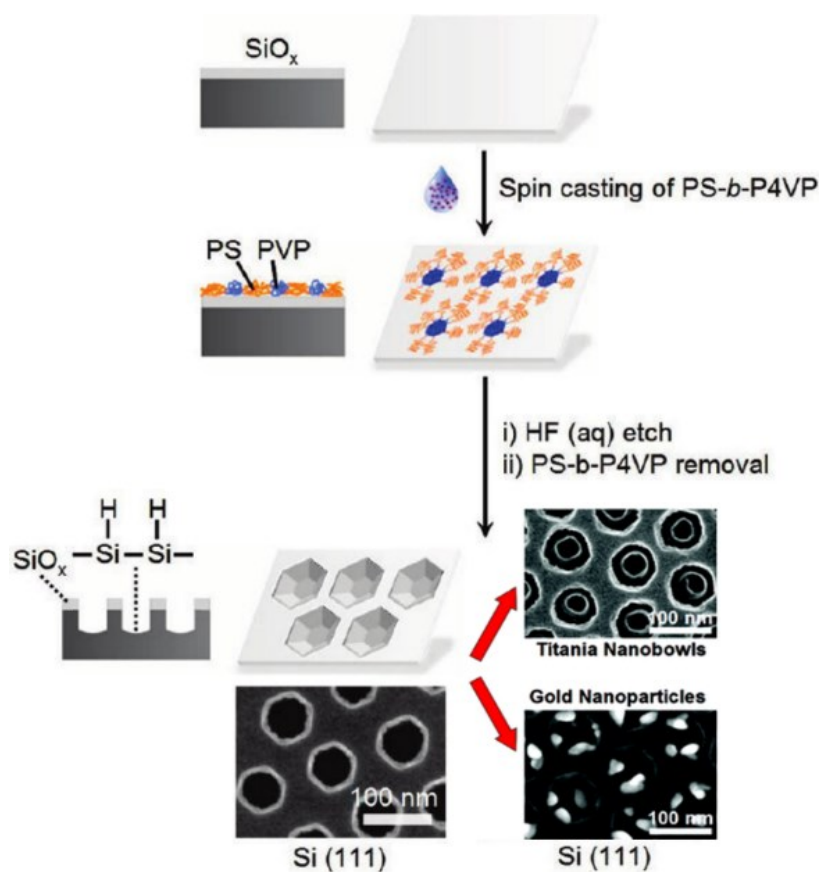


**Figure 2.5.** Scheme of the patterned nanohole formation using the self-assembled BCP film of PS-*b*-P4VP (109 k-27 k) as an etch stop. Reprinted with permission from ref. 158. Copyright © 2011 American Chemical Society.

BCP films can also act as a nanostructured etch stop to yield three-dimensional nanostructures in the underlying silicon,<sup>207</sup> GaAs<sup>208</sup> and other substrates.<sup>209</sup> For example, Figure 2.5 showed the self-assembled PS-*b*-P4VP film on a silicon substrate can act as a patterned mask for the selective etching by HF solution, and patterned nanoholes can be obtained with hydride terminated surfaces in the interior of the nanoholes and native oxide capped in the unetched area.<sup>167</sup> Titania nanobowls and gold nanoparticles can be selectively deposited in the nanoholes with further modifications of the etched surface. The nanopatterning of molecules on a surface using BCPs to direct reactivity is much more challenging and has been the subject of far less attention. BCPs have been applied to enable molecular transfer printing by Nealey and co-workers,<sup>210</sup> and have been used to direct the reactivity of diazonium salts on carbon surfaces,<sup>211</sup> but the area remains relatively unexplored.



from BCP self-assembly on silicon surface, and then PDMS precursors are spin-coated and peeled off after curing.<sup>162-164</sup> Localized catalytic reactions, including hydrosilylation and hydrogenation, can be conducted on hydride-terminated silicon, to generate hexagonal dot and fingerprint nanopatterns of organic monolayers on silicon surface. Inspired by this work, plasmonic stamps were fabricated by replacing the Pd and Pt metals with gold. In the remainder of the chapter, I will discuss the details of the fabrication of plasmonic stamps that contain gold nanopatterns for the LSPR (i.e. localized surface plasmon resonance)-assisted photochemical reactions on silicon surface.

## 2.2 Results and Discussion

### 2.2.1 Synthesis of Gold Nanopatterns

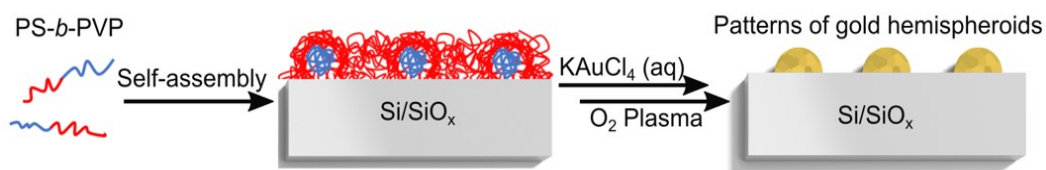


**Figure 2.7.** Scheme of a typical procedure for the fabrication of Au nanopatterns on silicon surfaces *via* block copolymer self-assembly.

Plasmonics stamps were prepared starting with the self-assembly of a thin film of PS-*b*-P2VP or PS-*b*-P4VP BCP on the surface of native oxide-capped single-crystalline silicon. Following solvent annealing and metallization with KAuCl<sub>4</sub>, the

AuCl<sub>4</sub><sup>-</sup>-loaded BCP was treated with an oxygen plasma to form a hexagonal array of gold hemispheroids on the silicon surface, followed by H<sub>2</sub>/Ar plasma to further remove any organic residues. Figure 2.7 outlines the fabrication procedure for nanopatterns of gold hemispheroids.

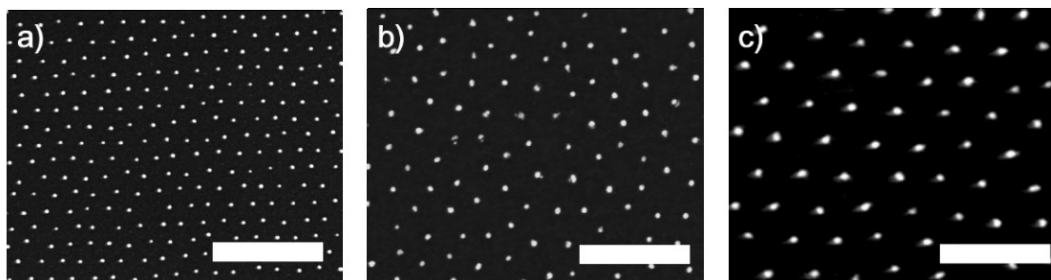


**Figure 2.8.** SEM images of gold nanopatterns on silicon surfaces. Scale bar: 400 nm. BCPs:  
a): PS-*b*-P2VP (125 k-*b*-58.5 k) b): PS-*b*-P2VP (91 k-*b*-105 k) c): PS-*b*-P2VP (190 k-*b*-190 k)

By changing the molecular weight of the BCP, the center-to-center spacings can be modulated as will be shown, *vide infra*. Figure 2.8 showed SEM micrographs of Au nanopatterns on flat silicon surfaces with different molecular weight BCPs. Center-to-center spacings can be tuned from 70 nm (125k-58.5k) to 160 nm (190k-190k) by simply varying the molecular weight of the applied BCPs.

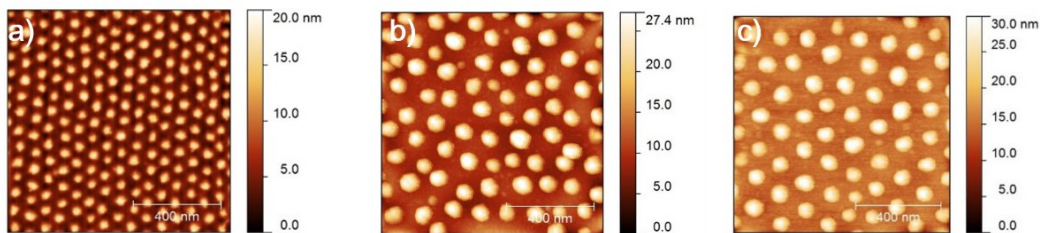


**Figure 2.9.** AFM height micrographs of gold nanopatterns on silicon surfaces with controlled spacings. BCPs: a): PS-*b*-P2VP (125 k-*b*-58.5 k) b): PS-*b*-P2VP (91 k-*b*-105 k) c): PS-*b*-P2VP (190 k-*b*-190 k).

AFM height micrographs in Figure 2.9 showed consistent center-to-center spacings in comparison to the SEM images in Figure 2.8. Note that the seemingly larger sizes of gold hemispheroids in AFM images compared with SEM images in Figure 2.8 are owing to the convolution effects of the AFM tips in the x-y scanning direction,<sup>212</sup> as the size of the AFM tips (~10 nm) has the same order of magnitude as that of the gold hemispheroids. The consistency of nanopatterns can be proved by the center-to-center spacings of the hexagonal dots.

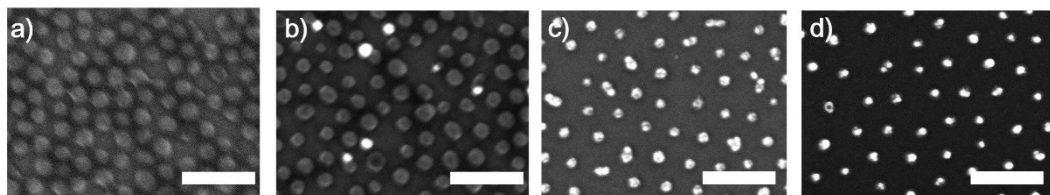


**Figure 2.10.** Self-assembled BCP film with oxygen plasma treatment time: 5 s (a), 10 s (b), 30 s (c), and 1 min (d). Scale bar: 200 nm. BCP: PS-*b*-P4VP (20 k-19k)

Plasma treatment of BCP films is crucial to facilitate the plasmonic stamp fabrication. Exposure to an oxygen plasma (10~30 s) is sufficient to observe the morphologies self-assembled BCPs after the metallization step. However, in order to obtain plasmonic gold hemispheroids, an extended oxygen plasma (10 min) is required to fully reduce the Au(III) ions to Au metal. Figure 2.10 indicates the transformation of gold nanopatterns from AuCl<sub>4</sub><sup>-</sup>-loaded BCP micelles with increased treatment time (10 min) of an oxygen plasma at 0.8 Torr. As mentioned earlier, another plasma step of H<sub>2</sub>/Ar is also applied to remove the organic residuals,<sup>213,214</sup> as well as the possible oxides on the formed metal hemispheroids.<sup>162,</sup>

163

### 2.2.2 Fabrication of Plasmonic Stamps

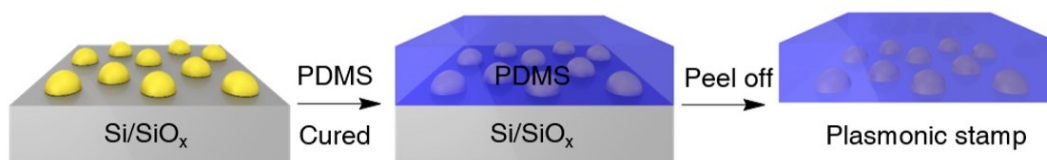


**Figure 2.11.** Scheme of a typical procedure for the fabrication of a plasmonic stamp.

After the fabrication of gold nanopatterns on flat silicon surfaces, the wafers were exposed to the vapor of trichloro(1H,1H,2H,2H-perfluorooctyl)silane for 60 min to result in a fluoro-functionalized, hydrophobic surfaces to facilitate the next step. The wafer was then coated with PDMS precursors and allowed to cure. Two different PDMS layers, h-PDMS (hard PDMS) and PDMS 184 (soft PDMS), were applied to

ensure the complete pattern transfer from silicon surface to the stamp. (See experimental method for details). When the plasmonic stamp was peeled off the silicon, the gold hemispheres remained embedded within the plasmonic stamp, with the flat faces of the gold hemispheres exposed on one side of the plasmonic stamp, as showed in Figure 2.11.

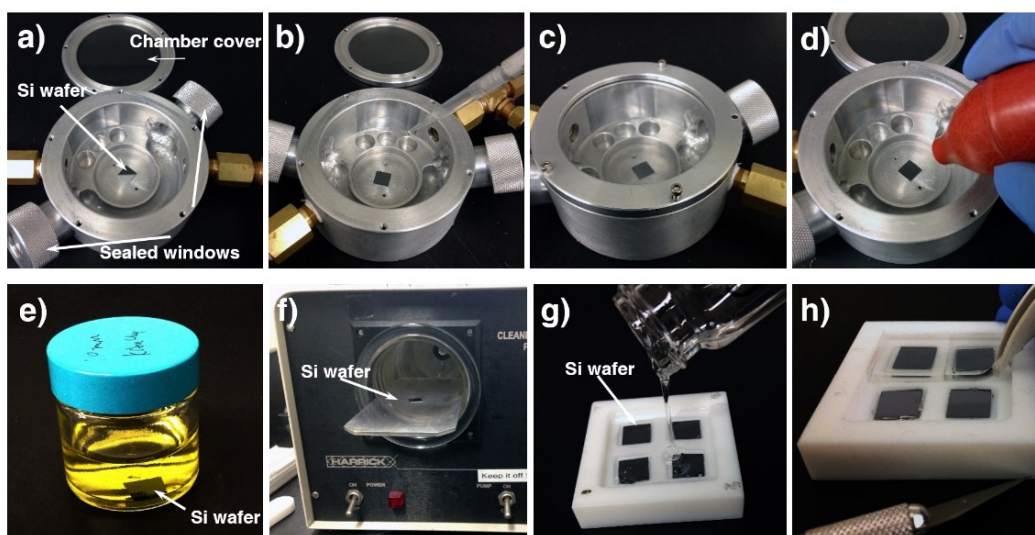


**Figure 2.12.** Photographs of the important steps necessary for preparing the plasmonic stamps.

In order to obtain ordered patterns, a solvent annealing step is necessary. Figure 2.12 shows the photos of each detailed step for the fabrication of the plasmonic stamp: (a) A BCP-coated Si wafer was placed in the homebuilt, aluminum solvent annealing chamber. (b) 1.0 mL of neat THF was added into the chamber. (c) The chamber was sealed to enable solvent annealing. (d) The chamber was purged with air after annealing. (e) The annealed wafer was immersed in a vial containing 10 mL of 10 mM  $\text{KAuCl}_4$  (aq) for 10 min. (f) The sample was rinsed thoroughly with water and

placed into the plasma cleaner for the two-step plasma treatment. (g) The gold nanoparticle-coated samples were exposed to trichloro(1H,1H,2H,2H-perfluorooctyl)silane vapor (not shown), followed by placement into the Teflon mold, and sequentially layered with h-PDMS and 184 PDMS, in this order, on the surfaces of the samples. (h) After curing overnight in the vacuum oven, the plasmonic stamp was carefully peeled off from the wafer surface.

### 2.2.3 Characterization of the Plasmonic Stamp

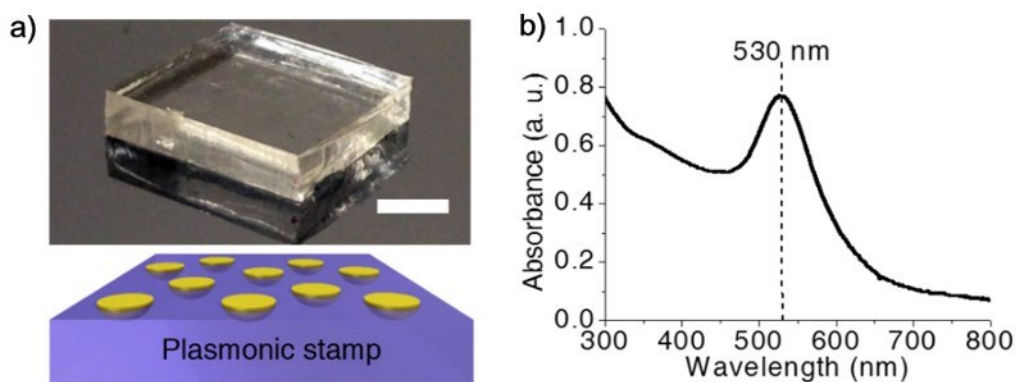


**Figure 2.13.** Optical photograph and UV-vis spectrum of a plasmonic stamp.

A flexible, optically transparent plasmonic stamp can be obtained after carefully peeling off from the silicon surface. In the example showed in Figure 2.13, the plasmonic stamp on a reflective silicon wafer was cut into a  $1.0 \times 1.0 \text{ cm}^2$ ,  $\sim 4 \text{ mm}$  thick stamp, which shows an absorbance in the UV-visible spectrum that peaks at 530 nm, which is attributed to the LSPR of the gold nanohemispheroids.

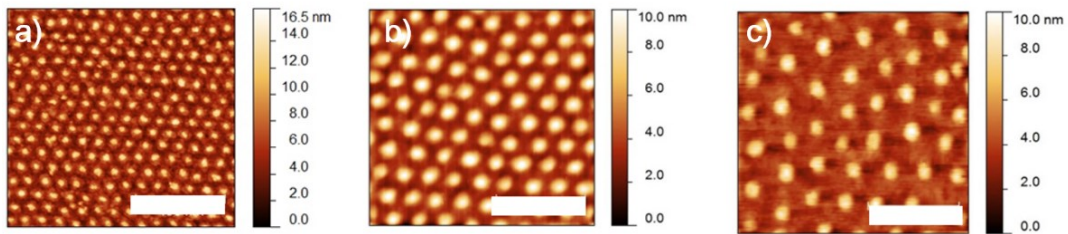


**Figure 2.14.** AFM height micrographs of plasmonic stamps with controlled spacings. Scale bar 400 nm: a): PS-*b*-P2VP (125 k-*b*-58.5 k) b): PS-*b*-P2VP (91 k-*b*-105 k) c): PS-*b*-P2VP (190 k-*b*-190 k).

The gold nanopatterns in can be imaged by AFM in tapping mode. Figure 2.14 shows the AFM height micrographs of plasmonic stamps with different spacings that is consistent with their respective Au pattern templates, as observed in Figures 2.8 and 2.9.

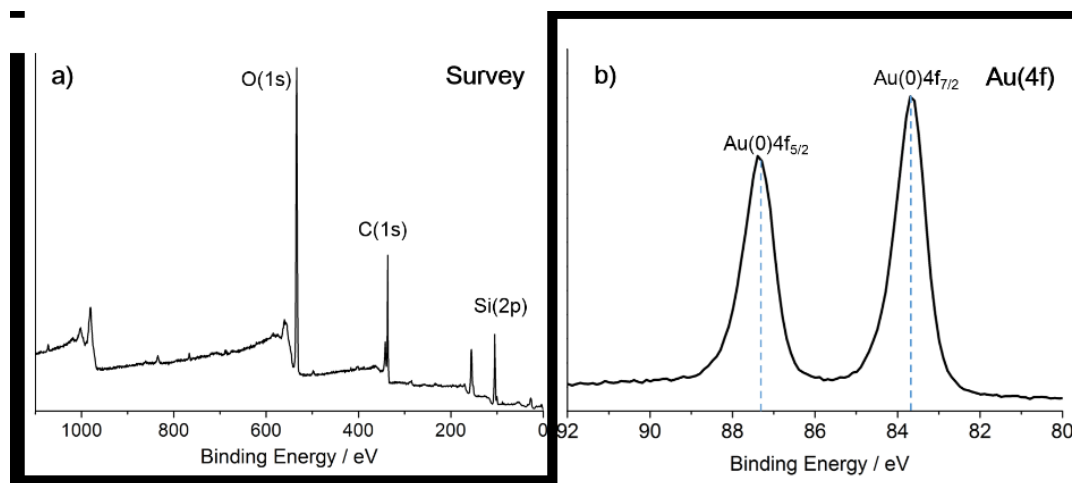


**Figure 2.15.** Survey scan a) and high resolution b) XPS spectra of a plasmonic stamp.

XPS spectra of the plasmonic stamp were further shown to confirm the composition, and are shown in Figure 2.15. Signals of O(1s), Si(2p) and C(1s) in the survey scan

of the XPS spectrum can be attributed to the PDMS substrate in the plasmonic stamp, although O(1s) and C(1s) may also come from air or residual solvents.<sup>162, 163</sup> A high resolution XPS spectrum of Au(4f) showed features at 83.8 eV and 87.6 eV that are consistent with published XPS data for Au(0),<sup>215</sup> which further substantiates the existence of gold nanopatterns that were fully reduced by plasma treatment from the AuCl<sub>4</sub><sup>-</sup> ions.

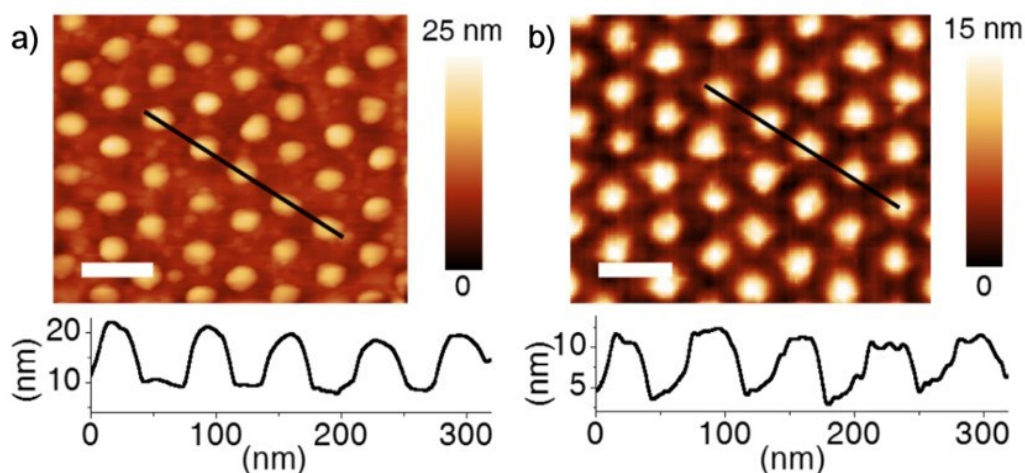


**Figure 2.16.** Comparison of AFM height micrographs and corresponding height profile of Au nanopatterns on silicon surface a) and a plasmonic stamp b). BCP: PS-*b*-P2VP (125 k-*b*-58.5 k)

The metallization of the self-assembled BCP and subsequent oxygen plasma treatment result in nanopatterns of hemispherical gold particles on flat surfaces. Figure 2.16 showed AFM height micrographs of gold hemispheroids on silicon surface and in a plasmonic stamp. The z-profile of Au nanoparticles in the plasmonic stamp (data extracted from the AFM height images in tapping mode) is much flatter

than on the silicon surface, indicating the existence of Au hemispheroids with flat surfaces and sharp edges on the surface of the plasmonic stamp.

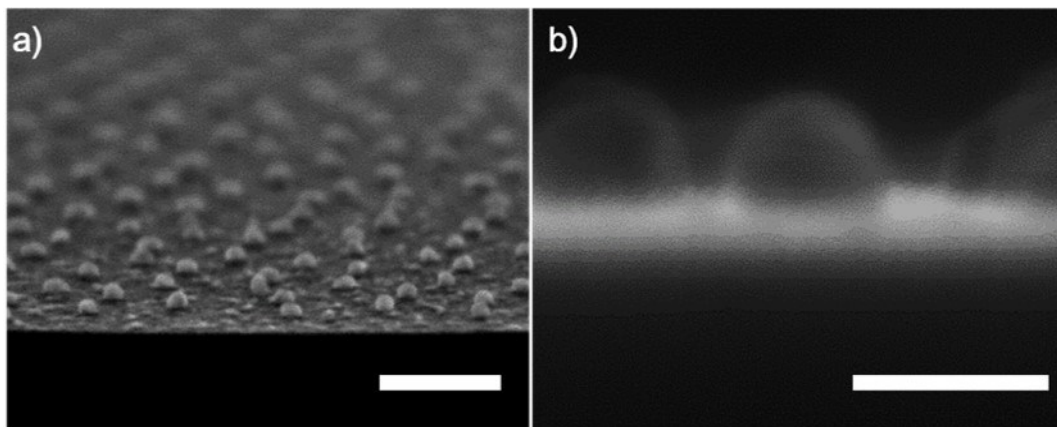


**Figure 2.17.** Tilted SEM image of patterned gold hemispheroids on Si/SiO<sub>x</sub> substrate. Cross-section SEM image in the inset showed the flatness of the underneath surface of a single gold hemispheroid. Scale bars: 100 nm, and 20 nm for inset. BCP: PS-*b*-P2VP (125 k-*b*-58.5 k)

The tilted and cross-section SEM images of the Au hemispheroids in Figure 2.17 further demonstrate the shape of hemispheroids, and will also be discussed later in Chapter 4 combined with their FDTD simulations. The hemispherical nature of the gold nanoparticle is important for the following plasmonic stamping, as the edges of the gold nanospheroids can generate higher electromagnetic field by LSPR to induce localized hydrosilylation on the hydride terminated silicon surface, which will be discussed in detail in the next two Chapters.

## 2.3 Conclusions

I demonstrate the fabrication of the plasmonic stamp, an optically transparent flexible PDMS stamp with embedded gold nanopatterns that produced *via* block copolymer self-assembly. Ordered gold hemispheroid arrays can be obtained after gold salt metallization and subsequent plasma treatment of solvent annealed block copolymers. By varying the molecular weight of the block copolymer templates, controllable size and spacings of Au nanopatterns in the plasmonic stamp can be achieved. The shape of the gold nanoparticles is also determined to be hemispherical by AFM height profile, as well as the the tilted and cross-section SEM images. This low-cost and versatile method can be applied for the various pattern transfers and can be combined with conventional top-down lithographic techniques.

## 2.4 Experimental Section

### Materials

All reagents and materials were used as received unless otherwise specified. Si wafers (111 plane-oriented, prime grade, p-type, B-doped,  $\rho = 1-10 \Omega\text{-cm}$ , thickness = 600-650  $\mu\text{m}$ ) were purchased from WRS Materials Inc. Millipore water (resistivity: 18.2 M $\Omega$ ) was used for the preparation of all aqueous solutions and for rinsing samples. Block copolymers (BCPs), all of the composition polystyrene-*block*-poly-2-vinylpyridine (PS-*b*-P2VP) with three different molecular weights (125 k-*b*-58.5 k, 91.5 k-*b*-105 k, and 190 k-*b*-190 k), were purchased from Polymer

Source Inc. The starting materials for preparing *h*-PDMS [Trimethylsiloxy terminated vinylmethylsiloxane-dimethylsiloxane (VDT-731), 25-35% (Methylhydrosiloxane) 65-70% (dimethylsiloxane) (HMS-301), and Pt divinyltetramethyldisiloxane (SIP6831.2)] were purchased from Gelest Corp., and 184 PDMS from Dow Corning. 2,4,6,8-tetramethyl-2,4,6,8-tetravinylcyclotetra-siloxane, 30% NH<sub>4</sub>OH (aq.), and 30% H<sub>2</sub>O<sub>2</sub> (aq.) were obtained from Sigma-Aldrich.

### **Silicon Wafer Preparation**

Si(111) wafers were cut into 1 × 1 cm<sup>2</sup> pieces, sonicated in methanol for 15 min, and dried with a stream of nitrogen gas. The silicon wafers were then cleaned *via* a standard RCA procedure: The wafers were first immersed in a solution of 30% NH<sub>4</sub>OH (aq.), water, and 30% H<sub>2</sub>O<sub>2</sub> (aq.), with volume ratio of 1:6:1 at 80 °C for 15 min, rinsed with water, and then immersed in a solution of 37.5% HCl (aq.), water, and 30% H<sub>2</sub>O<sub>2</sub> (aq.), with volume ratio of 1:5:1 at 80 °C for another 15 min. Lastly, the wafers were rinsed with water and dried with a stream of nitrogen gas.

### **Preparation of Au Nanopatterns on Si/SiO<sub>x</sub> Surface**

The BCP solution of PS-*b*-P2VP (125 k-*b*-58.5 k, 1.0 wt% in toluene) was spin cast at 4000 rpm for 40 s on a clean, native oxide-capped Si(111) wafer, and annealed in a homebuilt annealing chamber, as described earlier,<sup>159</sup> which contained 1.0 mL of THF for 60 min; The BCP layer on the Si(111) surface was then converted to the

corresponding gold nanopattern using a process previously described,<sup>166</sup> with slight modifications: Briefly, the sample was immersed in 10 mL of a 10 mM KAuCl<sub>4</sub> (aq.) solution for 10 min, rinsed with water, and then dried with a stream of nitrogen gas. The sample was then loaded into a bench top plasma cleaner (Harrick PDC 32G, 18 W), and exposed to an oxygen plasma at 0.8 Torr for 10 min to obtain the corresponding Au nanopatterns on the Si/SiO<sub>x</sub> surface. To ensure complete removal of polymer residues, the sample was then exposed to another 2 min of H<sub>2</sub>/Ar plasma at 1.5 Torr. Other BCPs were not solvent annealed with THF as they showed no improvement in hexagonal order as compared to ‘as spin-coated’. All other procedures were identical to those described here for PS-*b*-P2VP (125 k-*b*-58.5 k).

### **Preparation of Plasmonic Stamp**

The preparation of plasmonic stamps was based upon a process previously published by our group the preparation of catalytic Pd/Pt stamps,<sup>162-164</sup> with slight modifications. Briefly, the Au-nanopatterned Si/SiO<sub>x</sub> sample was placed in a desiccator with reduced pressure (1 Torr), together with an uncapped vial containing 15 μL of trichloro(1H,1H,2H,2H-perfluorooctyl)silane for 60 min. The sample was then rinsed with ethanol, and dried with a stream of nitrogen gas. To prepare the plasmonic stamp, *h*-PDMS (VDT-731, HMS 301, 2,4,6,8-tetramethyl-2,4,6,8-tetravinylcyclotetra-siloxane, and SIP6831.2) and 184 PDMS (degassed by centrifuging the PDMS prepolymer in a sealed tube at 3000 rpm for 30 min) were

coated, in sequence, on the wafer surface in a Teflon mold, as per the photographs in the Figure 2.12. Two curing steps (30 min for *h*-PDMS; and overnight for 184 PDMS) were performed at 65 °C in a vacuum oven after each PDMS coating step. After the curing steps, the plasmonic stamp was peeled off carefully from Si/SiO<sub>x</sub> substrate, soaked in hexane using a Soxhlet extractor for at least 6 h, rinsed with ethanol/water, and stored under vacuum prior to use.

# 3

## Plasmonic Stamp Lithography II: Chemistry and Scope

### 3.1 Introduction

Following the plasmonic stamp fabrication in Chapter 2, this chapter will introduce their application *via* LSPR-assisted surface hydrosilylation to direct the patterning of organic molecules on silicon surfaces, referred to as plasmonic stamp lithography.<sup>156</sup> The hydrosilylation reaction takes place at the hydride-terminated silicon surface in the presence of neat 1-alkenes or 1-alkynes that are sandwiched between a plasmonic stamp and a hydride-terminated silicon wafer. After the localized hydrosilylation under illumination, 1-alkyl or 1-alkenyl molecules are attached to the silicon surface in the form of ordered patterns of molecules that reflect the gold nanopatterns in the plasmonic stamp, as well as the original patterns from the self-assembled BCP template. In the introduction of this chapter, current research and mechanisms will be briefly introduced, with the focus on the light induced-hydrosilylation on the hydride-terminated silicon surfaces.

### 3.2 Hydrosilylation on Hydride-terminated Silicon Surfaces

The chemical reaction that is the focus of this work, hydrosilylation, involves the insertion of an unsaturated bond into a silicon-hydride group on the surface, which results in attachment of the organic molecules to the silicon, *via* the formation of Si-C bonds.<sup>216-223</sup> Figure 3.1 outlines the surface hydrosilylation reaction of different types of unsaturated organic molecules on hydride-terminated Si(111) surfaces, including alkenes, alkynes, and an aldehyde. Understanding the mechanism of the seemingly simple hydrosilylation reaction is important, as there have been several proposed reaction mechanisms, depending on the reaction conditions such as temperature, light sources, types of silicon surfaces, etc.<sup>220, 224, 225</sup>

#### 3.2.1 Surface Hydrosilylation without Incident Light

Hydrosilylation on surfaces was first communicated 23 years ago by Chidsey and Linford to form a series of alkyl monolayers on Si(100)-H and Si(111)-H surfaces *via* the formation of silicon-carbon covalent bonds.<sup>216</sup> They proposed that surface hydrosilylation was a radical based reaction driven by the dangling bonds induced by radical initiators on the silicon surface.<sup>216</sup> The surface hydrosilylation can also be achieved at a reaction temperature above 150 °C *via* homolytic cleavage of the Si-H bonds on flat silicon surfaces.<sup>226, 227</sup> Since then, this interesting finding on silicon chemistry has been the subject of great attention because of its utility for covalent interfacing of a broad range of organic molecules to different types of

silicon surfaces, including the surfaces of flat silicon,<sup>228-230</sup> nanocrystalline/porous silicon,<sup>231-233</sup> and silicon nanoparticles.<sup>225, 234-237</sup>

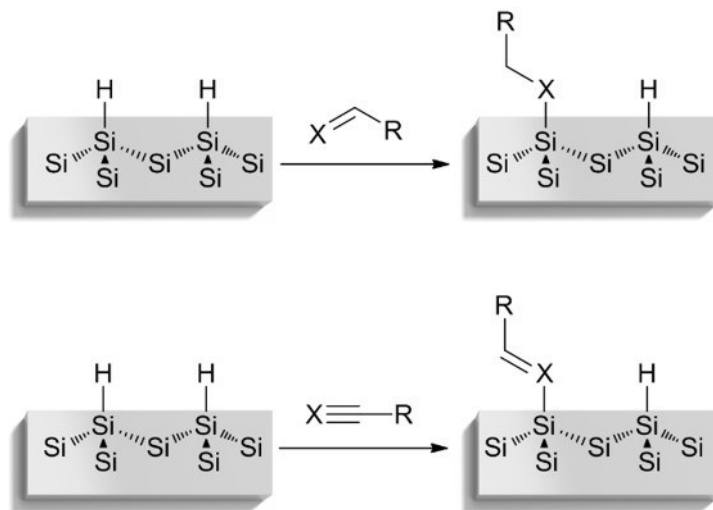


**Figure 3.1.** Scheme of hydrosilylation of different types of molecules on Si(111)-H surface.

### 3.2.2 UV Light Induced Surface Hydrosilylation

Other than the mentioned hydrosilylation initialized by catalysts and heating, photohydrosilylation has demonstrated to be another way to covalently attach organic molecules on silicon surfaces. Under the illumination of UV or visible light, photohydrosilylation can take place without the addition of radical catalyst or temperature increase, and therefore is recognized as an efficient and clean strategy for silicon surface hydrosilylation. In 1997, UV-induced hydrosilylation of 1-pentene on a flat Si(111)-H surface was reported for the first time.<sup>238</sup> The mechanism was considered to be radical-based chemistry, having a similar reaction pathway as the previously mentioned hydrosilylation reactions that are initiated thermally.

Specifically, the UV light could cleave the Si-H bonds to form radicals or dangling bonds on the hydride-terminated silicon surfaces, followed by the formation of Si-C bonds and attachment of 1-alkyl molecules on the surface.<sup>238-241</sup> A mechanistic scheme of radical-based hydrosilylation on silicon surface is outlined in Figure 3.2.

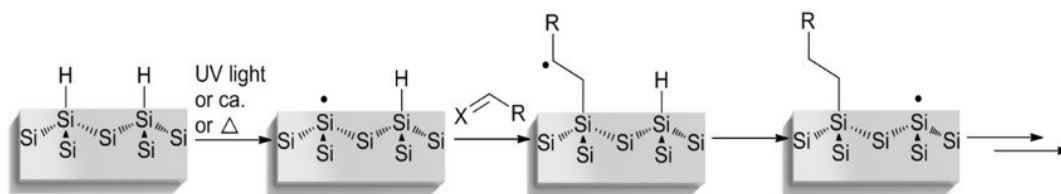


**Figure 3.2** Scheme of radical-based hydrosilylation on Si(111)-H surface.

Another mechanism of electron photoemission was proposed by Hamers group later to interpret the UV promoted hydrosilylation.<sup>219</sup> As shown in Figure 3.3, the authors used three identical alkene linkers with different terminal groups (i.e. 1-dodecene, TFAAD (N-(dec-9-enyl)-trifluoroacetamide), and tBoc (10-N-Boc-aminodec-1-ene)) for UV-induced (254 nm) hydrosilylation and found that the TFAAD molecule has a much higher grafting efficiency than the other two identical molecules, which cannot be explained by radical based mechanism since the reaction efficiency should be similar for these selected molecules. By systematically investigating the kinetics and relative energy levels of 1-alkenes and silicon from UV induced hydrosilylation, they proposed that UV light can eject a valence electron that is absorbed by electron-accepting groups of TFAAD, and that the leftover hole on the silicon surface can be attacked by the 1-alkenes, resulting in the

grafting of 1-alkyl molecules, as shown in Figure 3.3b. This proposed mechanism was further investigated in our group by adding a series of aromatic acceptors with various LUMO levels.<sup>242</sup> Results showed the acceptors with lower LUMO levels can lead to higher hydrosilylation rates, and the chlorination on silicon surface with aromatic electron acceptors containing weak C-Cl bonds suggests the radical-based mechanism can also take place on the surface at the same time.

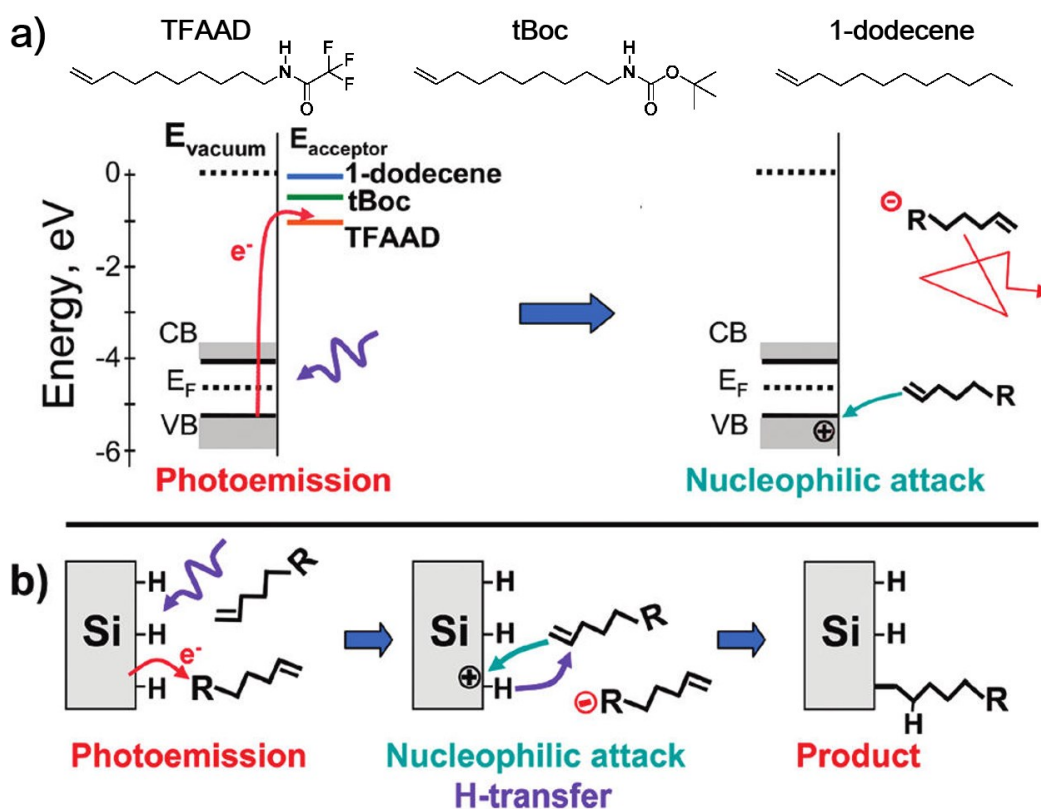


**Figure 3.3.** Scheme of electron photoemission mechanism for UV-induced hydrosilylation on flat, hydride-terminated silicon surfaces. Reprinted with permission from ref. 237 Copyright ©

2010 American Chemical Society

### 3.2.3 Visible Light Induced Surface Hydrosilylation

The reaction pathways proposed for white light-induced hydrosilylation reactions on silicon surface typically involve electron-hole pairs, since visible light is incapable of homolytic Si-H bond cleavage or electron photoemission.<sup>218, 219, 225</sup> Previous work in our group demonstrated that under the illumination of visible light, hydrosilylation of 1-alkenes and 1-alkynes can be conducted within several minutes on porous silicon.<sup>218, 243-246</sup> High concentration of excitons were generated in the silicon nanocrystallites, and unsaturated organic molecules then attack the holes of the excitons in a nucleophilic fashion to form 1-alkyl or 1-alkenyl functionalized silicon surface, as illustrated in Figure 3.4. This exciton-based mechanism was further demonstrated by adding exciton-quenching agents that block hydrosilylation on porous silicon surface.<sup>218</sup> In addition, the presence of electron acceptors led to higher hydrosilylation rates due to the increased hole lifetime that therefore favors the Si-C bond formation on the porous silicon surface (Figure 3.4).<sup>244, 247</sup>

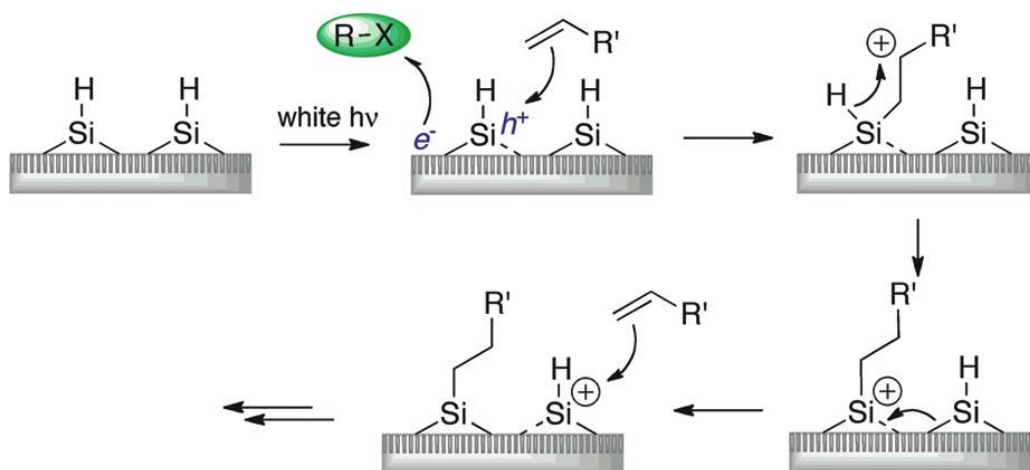


**Figure 3.4.** Scheme of exciton based mechanism for the white light promoted hydrosilylation on porous silicon surface in the presence of R-X as an electron acceptor. Reprinted with permission from ref. 244. Copyright © 2012. American Chemical Society

White light-promoted hydrosilylation of 1-alkenes and 1-alkynes can also take place on flat hydride-terminated silicon surfaces such as Si(111)-H and Si(100)-H, in spite of longer reaction time (10 to 15 h) needed to reach a coverage that is comparable to that with other approaches such as UV-induced or thermal hydrosilylation on flat silicon surface.<sup>248-250</sup> Zuilhof and co-workers believe that the reaction was driven by the white light-induced electron-hole pairs that lead to the grafting of 1-alkyl and 1-alkenyl molecules in a similar pathway as the exciton based mechanism.<sup>248, 249</sup>

Sugimura and coworkers presented results showing that gold nanoparticles capped with alkene-terminated thiols showed higher levels of incorporation on flat hydride-terminated silicon surface when illuminated with light that overlapped with the absorption maximum of the gold nanoparticles. The authors referred to the gold

nanoparticles as ‘photon collectors’, transferring the energy of the incident illumination to the surface, as suggested in Figure 3.5.<sup>251</sup>

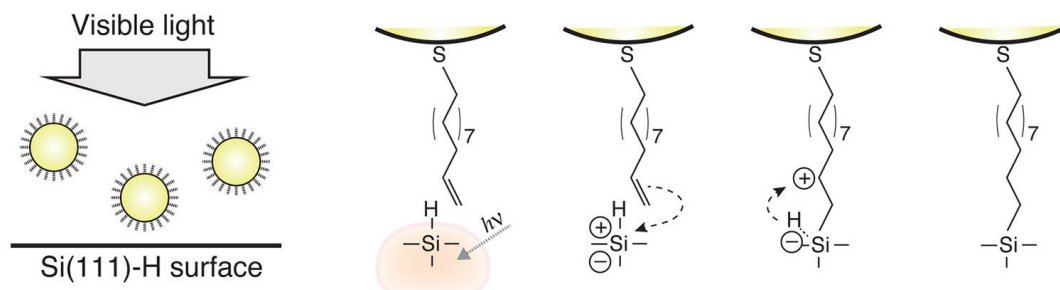


**Figure 3.5.** Mechanistic scheme of the gold nanoparticle mediated hydrosilylation on flat Si(111)-H surface. Reprinted with permission from ref 251. Copyright © 2013. American Chemical Society

In the gold nanoparticle-mediated hydrosilylation, the mechanism was not clear, and the proposed ‘photon collector’ role of the gold nanoparticles could come from either scattering of gold nanoparticles, and/or the surface plasmon absorption.<sup>120, 126</sup> Inspired by this work, I decided to investigate gold particle-mediated hydrosilylation by incorporating gold nanopatterns in a plasmonic stamp, with the goal of determining the mechanism, which will be described in detail in the rest of the chapter.

### 3.3 Results and Discussion

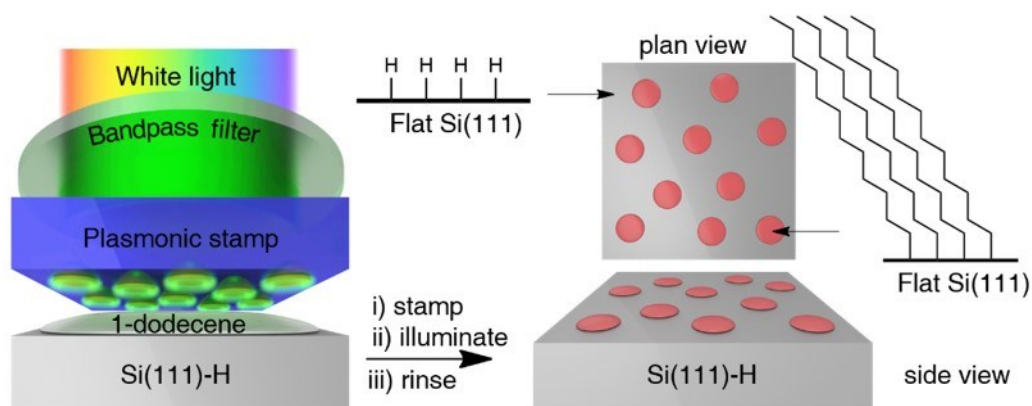


**Figure 3.6.** Scheme of a typical procedure for plasmonic stamping on Si(111)-H surfaces.

The LSPR-assisted hydrosilylation was carried out by applying the gold nanopatterned plasmonic stamp on a hydride-terminated silicon (111) surface, referred to as Si(111)-H, prepared *via* a 4 minute etch in 40% NH<sub>4</sub>F (aq.). Neat 1-dodecene (30 L) was then dropped onto the Si(111)-H surface in a nitrogen-filled glove box, and the plasmonic stamp placed on top in direct contact; this PDMS/1-dodecene/Si(111)-H sandwich was then firmly clamped together, as shown in Figure 3.7. The surface of the silicon was then illuminated through the plasmonic stamp with green light of mild intensity (50 mW/cm<sup>2</sup>; filter: CW526 (centre band wavelength: 526 nm); FWHM (full width-half max: 180 nm) for the desired period of time (0 to 60 min); the silicon sample was then released, rinsed with dichloromethane, dried under an argon stream, and then analyzed by atomic force microscopy (AFM).

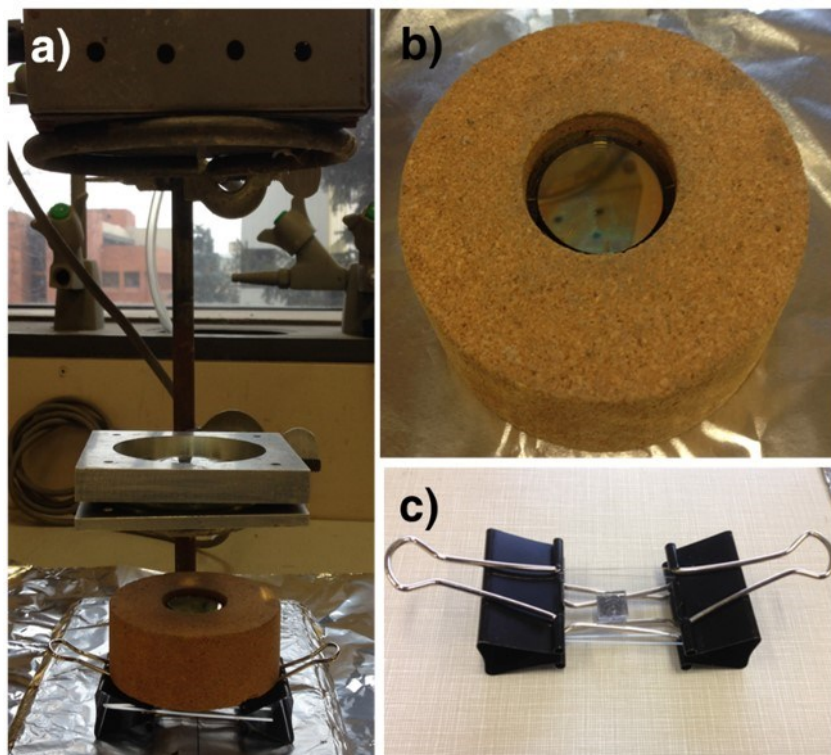


**Figure 3.7.** Photograph of the experimental setup for plasmonic stamping.

Photographs of detailed experimental setup can be observed in Figure 3.7, including the ELH light source (top), a focusing lens (middle), the band pass filter (held in the cork ring), and the sample (bottom). (b) Photograph of a band pass filter held within the cork ring holder. (c) Photograph of the silicon sample, sandwiched between glass slips and fixed with two paper clamps on each side. Note that the stamping process was conducted in a nitrogen-filled glovebox, and tentire setup was moved out from glove box for improved photographic clarity.

### 3.3.1 Plasmonic Stamping of Alkenes on Silicon

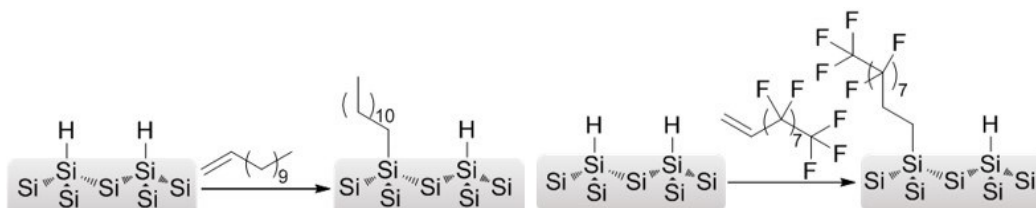


**Figure 3.8.** Schematic outline of hydrosilylation chemistry on flat Si(111)-H surfaces with two typical 1-alkenes used for plasmonic stamping.

Hydrosilylation of 1-alkenes on hydride-terminated silicon surfaces, can result in 1-alkyl molecules tethered on silicon surface. Figure 3.8 outlines the hydrosilylation of two selected alkenes that were investigated in this research. With the plasmonic stamp-assisted hydrosilylation, Patterns of 1-alkyl groups can be obtained on hydride-terminated silicon surface, and can be characterized using atomic force microscopy to directly measure the pattern and height of hydrosilylated molecules at the nanoscale, as shown in Figure 3.9.

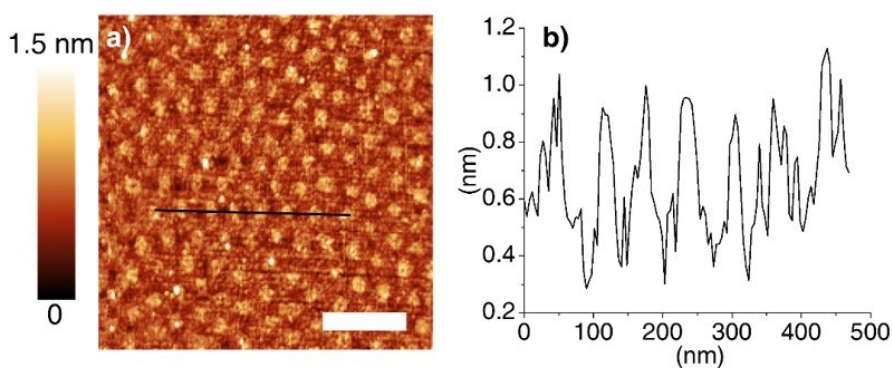


**Figure 3.9.** AFM height micrograph and corresponding height profile of 1-dodecene stamped Si(111)-H surface. Scale bar: 200 nm BCP: PS-*b*-P2VP (125 k-*b*-58.5 k)

An AFM micrograph of a freshly etched Si(111)-H surface shows the expected Si(111) terrace planes (Figure 3.10a). The hexagonal pattern of dodecyl spots on the Si(111) starts to emerge after 30 min of illumination (Figure 3.10b), and becomes more apparent after 60 min (Figure 3.10c).

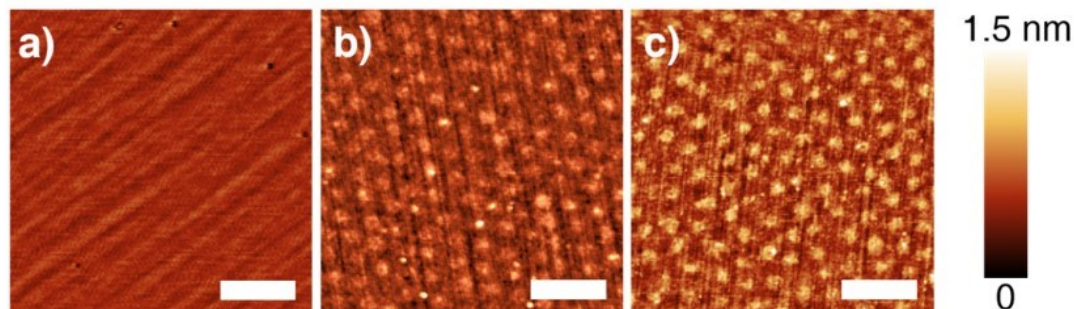


**Figure 3.10.** AFM height micrographs of 1-dodecene stamped Si(111)-H surfaces with a variation of illumination time of a) 0 min, b) 30 min, c) 60 min. BCP: PS-*b*-P2VP (125 k-*b*-58.5 k)

The centre-to-centre spacing of the hexagonal spots can be controlled by varying the molecular weight of the BCPs; Figures 3.11a-c show dodecyl patterns with the expected heights for dodecyl chains ( $\sim 1.0$  nm), with centre-to-centre spacings of  $\sim 70$  nm, 120 nm, and 160 nm, prepared with PS-*b*-P2VP BCPs of molecular weights of 125 k-*b*-58.5 k, 91 k-*b*-105 k and 190 k-*b*-190 k, respectively. The statistics of center-to-center spacings of the three types of nanopatterns (i.e. Au nanopatterns on silicon surfaces, Au nanopatterns on plasmonic stamps, and hydrosilylated patches on stamped Si(111)-H surfaces) are summarized in Table 3.1, indicating the

consistent pattern transfers from the initial BCP self-assembly to the final ordered molecule patches.

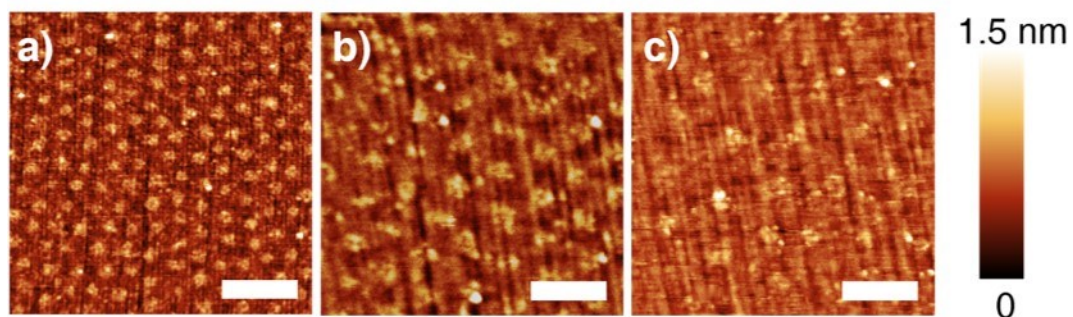


**Figure 3.11.** AFM height micrographs of 1-dodecene stamped Si(111)-H surfaces with controlled spacings. BCPs: a) PS-*b*-P2VP (125 k-*b*-58.5 k); b) PS-*b*-P2VP (91 k-*b*-105 k); c) PS-*b*-P2VP (190 k-*b*-190 k)

**Table 3.1.** Statistics of center-to-center spacings of nanopatterns during stamping process.

Block copolymers	Au nanopattern on silicon (nm)	Au nanopatterns on stamps (nm)	Patches on stamped surfaces (nm)
125k- <i>b</i> -58.5k	75 ± 6	73 ± 8	73 ± 6
91.5k- <i>b</i> -105k	123 ± 7	121 ± 5	119 ± 7
190k- <i>b</i> -190k	154 ± 6	156 ± 9	157 ± 10

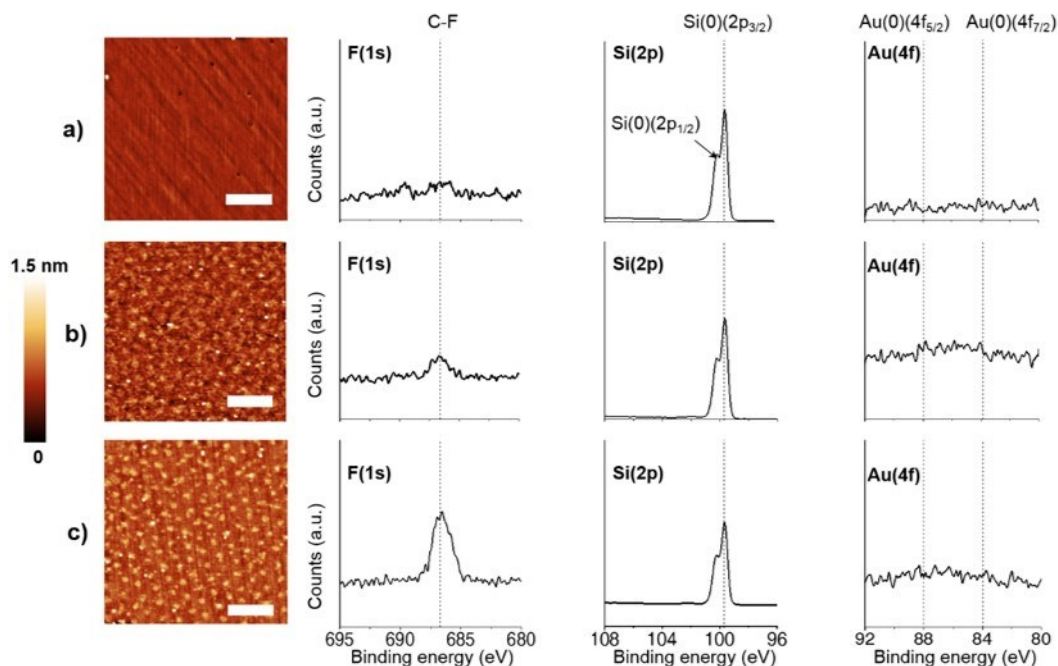


**Figure 3.12.** AFM height micrographs and XPS spectra of 1H,1H,2H-perfluoro-1-decene on silicon surfaces with a variation of illumination time of a) 0 min, b) 30 min, c) 60 min.. BCP: PS-*b*-P2VP (125 k-*b*-58.5 k)

To provide further evidence of the plasmonic stamping on hydride-terminated silicon surfaces, a fluorinated alkene, 1H, 1H, 2H-perfluoro-1-decene, was tested for LSPR-mediated hydrosilylation, using the same conditions as those described earlier for 1-dodecene, which was characterized *via* X-ray photoelectron spectroscopy (XPS) and contact angle (goniometry) measurements. The AFM images and corresponding XPS data for nanopatterned Si(111)-H at 0 min, 30 min and 60 min of illumination are shown in Figure 3.12; as can be seen from the XPS data, the F(1s) signal (687.3 eV) increases in intensity with increased time, and the high resolution spectra of the Au(4f) and Si(2p) regions show the absence of features

that would correspond to residual gold (84 eV and 88 eV),<sup>63</sup> PDMS (~102 eV),<sup>64</sup> and oxidized surface-bound silicon (~103 eV).<sup>64</sup>

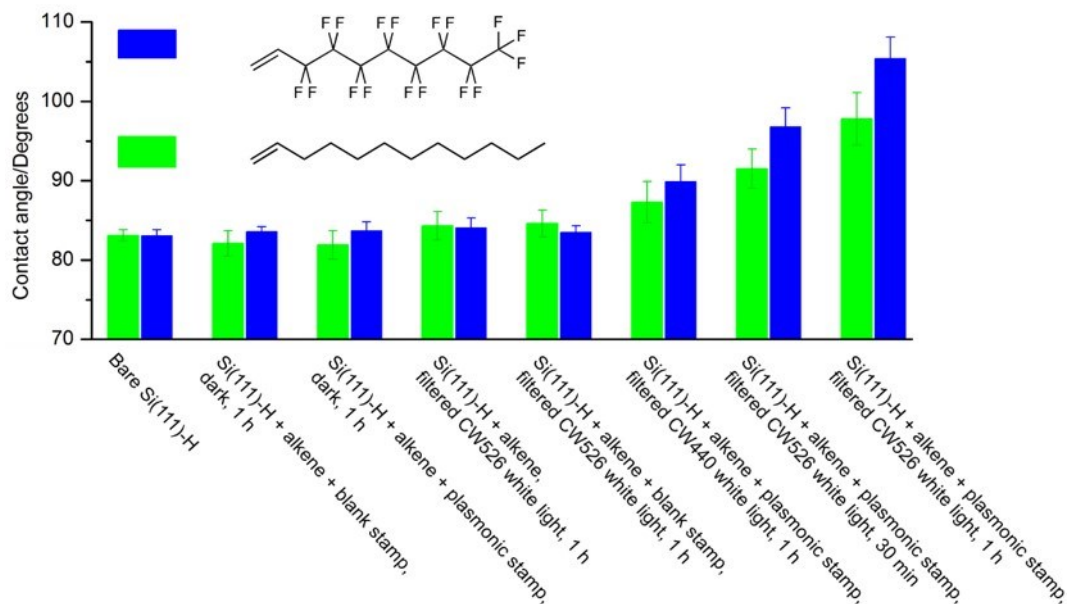


**Figure 3.13.** Water contact angles of the 1-alkene stamped Si(111)-H surfaces under various conditions.

A series of control experiments support the proposal that the gold nanoparticles are essential to enable light-induced hydrosilylation. Illumination of a blank plasmonic stamp (missing gold nanoparticles), or applying the gold-nanopatterned plasmonic stamp in the dark, revealed no dodecyl patterns on the surface. The corresponding contact angle measurements for these surfaces are shown in Figure 3.13. The contact angle of the Si(111)-H surface was found to measurably increase only when the surface was subjected to the combination of both a plasmonic stamp and illumination.. The maximum observed contact angles for patterned Si(111)-H

surfaces were  $\sim 98^\circ$  and  $105^\circ$  for hydrosilylation with 1-dodecene, and 1H, 1H, 2H-perfluoro-1-decene, respectively.

### 3.2.2 Plasmonic Stamping of Alkynes on Silicon

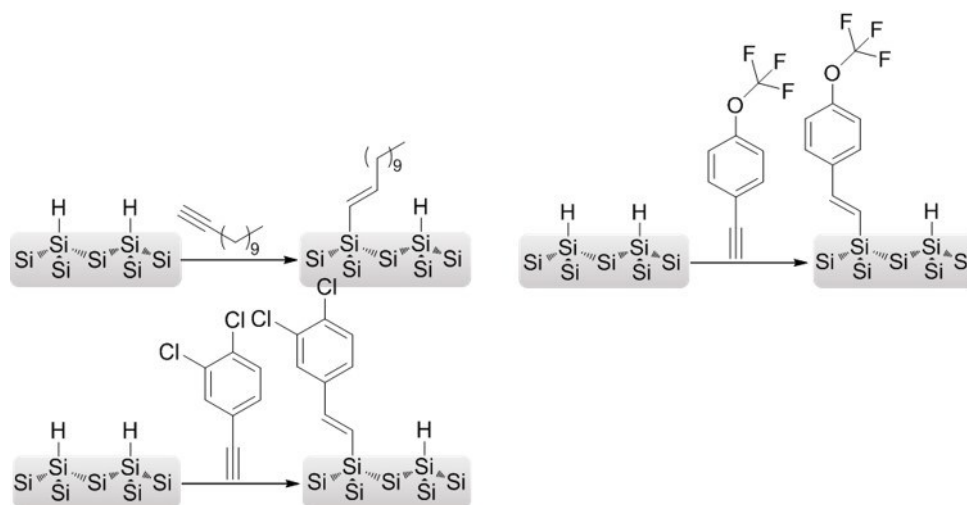


**Figure 3.14.** Schematic outline of the hydrosilylation chemistry on flat Si(111)-H surfaces with selected 1-alkynes used for plasmonic stamping.

Figure 3.14 summarized the SPR-assisted hydrosilylation of 1-alkyne on Si(111)-H surface. Three 1-alkyne molecules (1-dodecyne, 4-(trifluoromethoxy)phenyl acetylene, and 3,4-dichlorophenylacetylene) were applied to the plasmonic stamp-mediated system, and the patterned functionalized surfaces after stamping can be captured by atomic force microscopy (AFM) after 60 min stamping, as shown in Figure 3.15.

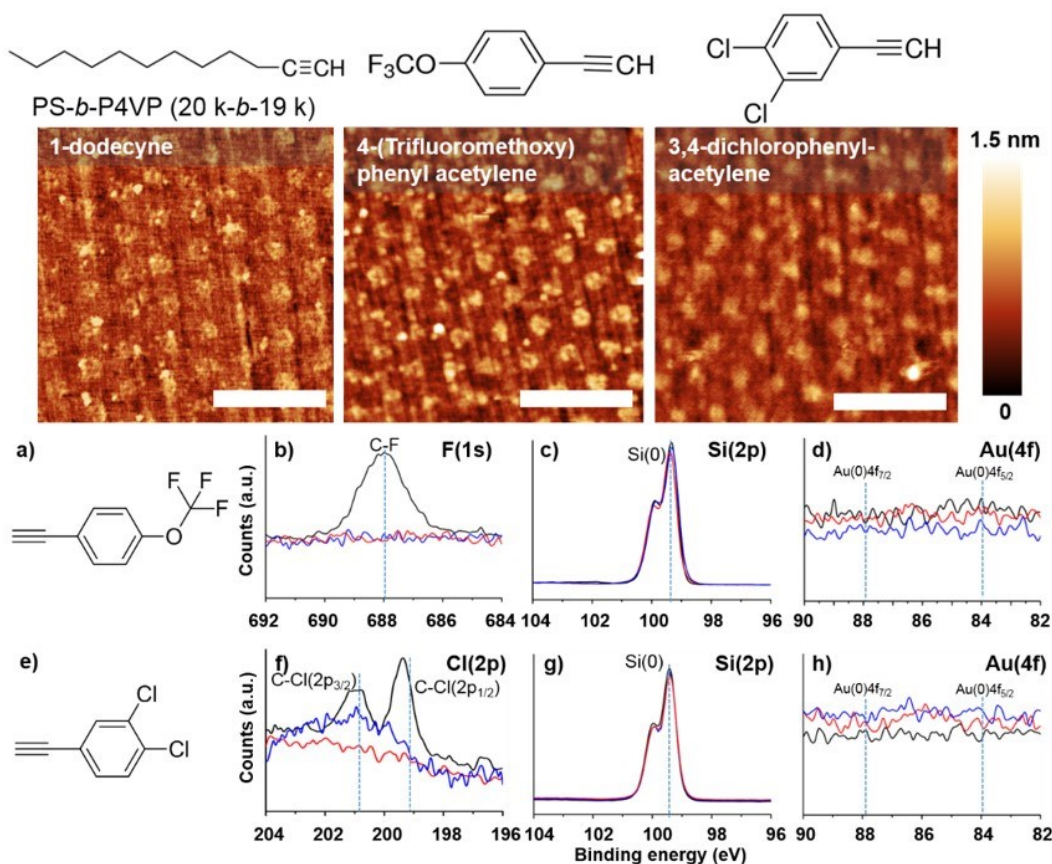


**Figure 3.15.** AFM height micrographs and XPS spectra of 1-alkyne-stamped Si(111)-H surfaces after plasmonic stamping under various conditions. Scale bar: 200 nm.

As for 4-(trifluoromethoxy)phenyl acetylene, and 3,4-dichlorophenylacetylene, XPS measurements were further conducted to confirm hydrosilylation. F(1s) (687.3 eV), and Cl(2p) (199.2 eV and 200.8 eV for 2p 3/2, and 2p 5/2) signals were observed, and only in the presence of both the plasmonic stamp and filtered white light (50 mW/cm<sup>2</sup>; filter center wavelength: 526 nm; FWHM (full wavelength half max): 180 nm), indicating successful pattern transfers *via* localized hydrosilylation. In addition, no residual gold and oxidation of the silicon surface were observed according to the absence of the Au(4f)<sup>252</sup>, and Si-O<sup>253</sup> in the high-resolution XPS

data. In addition, no patterns can be captured in the absence of Au hemispheroids or incident light, and the contact angle comparisons in Table 3.2 further prove the failed pattern transfer under these conditions.

**Table 3.2.** Water contact angles of the 1-alkyne stamped Si(111)-H surfaces under various conditions

Samples	Light Intensity	Contact Angle* (Degree) 1-dodecyne	Contact Angle* (Degree) 4-(Trifluoromethoxy)- phenyl acetylene
Si(111)-H (Control)	Dark		83.1 ± 0.7
Si(111)-H + neat alkyne + plasmonic stamp	Dark	83.7 ± 0.9	82.6 ± 0.7
Si(111)-H + neat alkyne + blank PDMS stamp	526 nm filter for 1 h Intensity: 50 mW/cm <sup>2</sup>	84.5 ± 1.8	83.9 ± 1.5
Si(111)-H + neat alkyne + plasmonic stamp	526 nm filter for 1 h Intensity: 50 mW/cm <sup>2</sup>	94.6 ± 1.9	88.2 ± 1.9

### 3.3.3 Pattern Visualization for the Stamped Molecules on Silicon

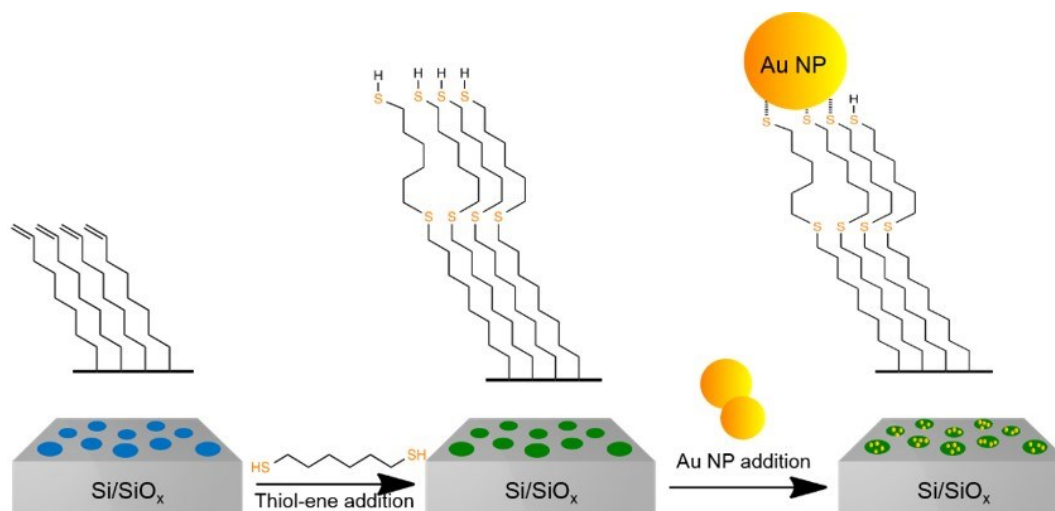


**Figure 3.16.** Outline of pattern visualization *via* citrate-capped gold nanoparticles

In order to verify that these patterns are a result of localized hydrosilylation, further chemical functionalization was carried out, with the goal of binding gold nanoparticle tags to the spots in the hexagonal patterns for SEM imaging. As showed in Figure 3.16, a bis-diene was used as the ink for stamp-mediated hydrosilylation, since hydrosilylation of this molecule would yield  $\omega$ -alkenyl-terminated spots, with centre-to-centre spacings of 70 nm that derived from the self-assembled BCP template. Thiol-ene click chemistry on the  $\omega$ -alkene groups with a dithiol would be expected to lead to spots with terminal thiol groups;<sup>254</sup> exposure of the functionalized silicon to citrate-capped  $\sim 10$  nm-diameter gold nanoparticles resulted in binding of the nanoparticles to the thiol-capped spots, resulting in a templated hexagonal nanopattern, as shown in Figure 3.17.

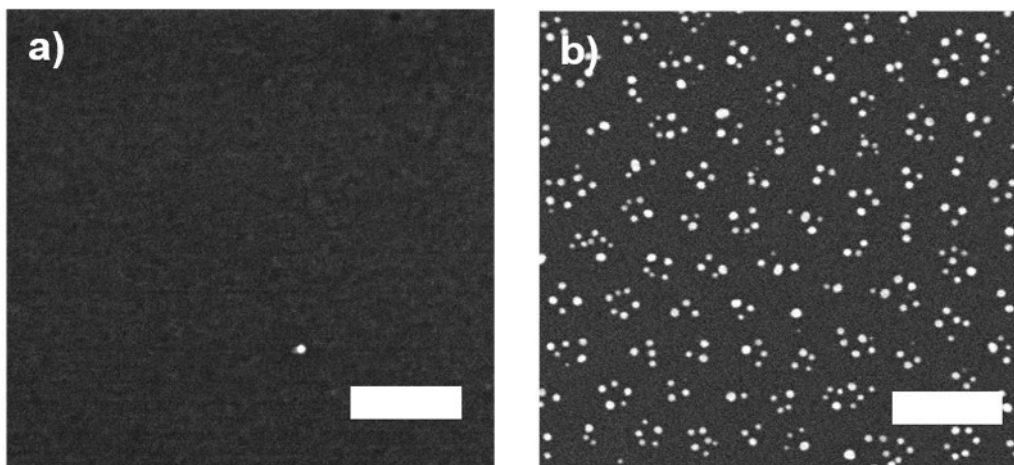


**Figure 3.17.** SEM images of an of the patterned silicon surface a) before and b) after exposure to  $\sim 10$  nm Au nanoparticles. SEM scale bar: 100 nm.

Due to the discrete nature of using nanoparticles for visualization, it is difficult to interpret the finer structure of the regions patterned *via* hydrosilylation. In contrast to the method whereby thiol-terminated patches were exposed to pre-formed gold nanoparticles, in an alternative method shown in Figure 3.18, the sample was immersed in a solution to promote the electroless deposition of gold. As can be seen in Figure 3.19, both the SEM and AFM micrographs reveal that the gold selectively deposits in a ring-like pattern, thus emphasizing that the original pattern formed by plasmonic stamping is not a uniform circular patch, but a ring. These gold rings formed at the places where hydrosilylation took place on the silicon surface, reflecting the shape of the electric field distribution in the Au hemispheroids. In addition, it is also possible that the thiol-ene chemistry happened at both ends of the dithiol molecules, and therefore reduced the density of thiol-terminated molecules

at the centers of the hydrosilylated patches, resulting in the formation of gold rings after the gold deposition. The corresponding XPS spectra for the thiol-terminated and gold-functionalized surfaces are shown in Figures 3.20a and b, respectively.

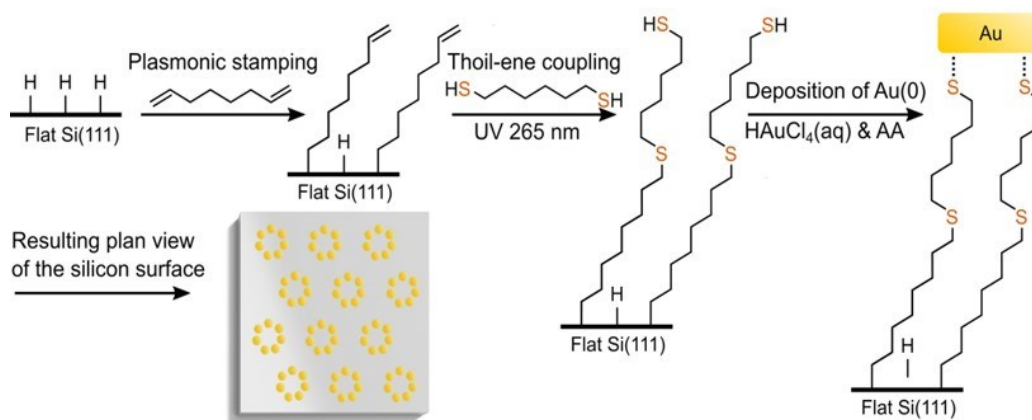


**Figure 3.18.** Schematic outline of pattern visualization *via* gold electroless deposition

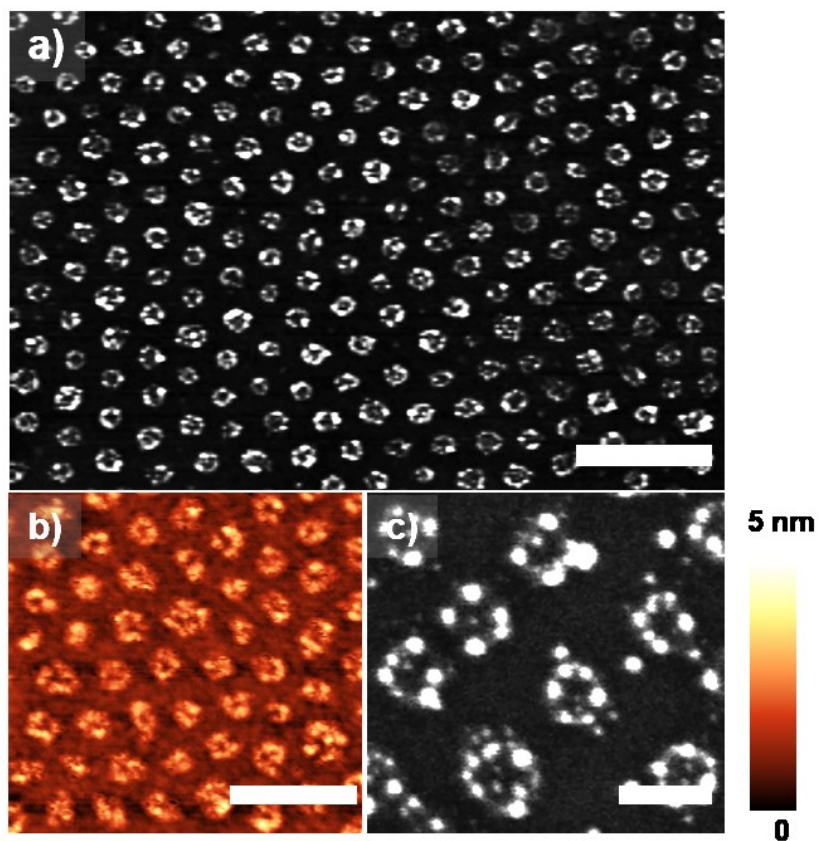


**Figure 3.19.** SEM and AFM images of the patterned silicon surface after electroless gold deposition. Scale bars: 200 nm for a,b), and 20 nm for c).

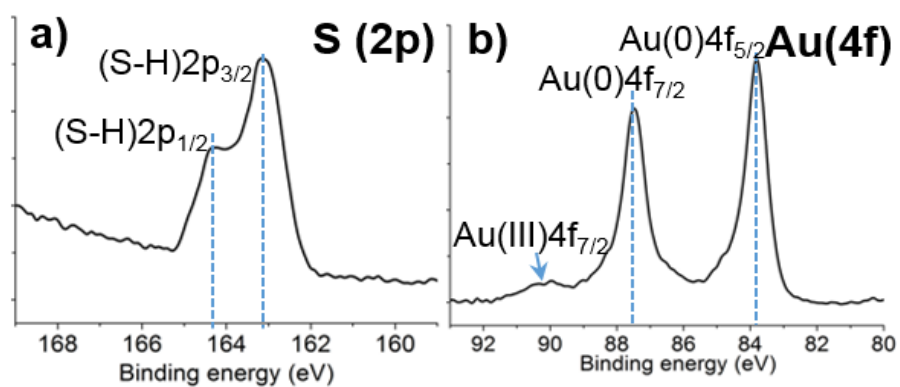


**Figure 3.20.** XPS spectra of S(2p) after thiol-ene chemistry and Au (4f) after final Au deposition

### 3.2.4 Recycling of Plasmonic Stamps

Reusability would be important for a ‘real world’ application to minimize the necessity to fabricate new stamps. As shown in Figure 3.21, the plasmonic stamp could be reused three times after cleaning with dichloromethane and hexane after each use. No pattern transfer to the silicon surface was observed if the plasmonic stamp was used without the cleaning steps, probably due to adventitious physisorbed impurities that increase the spacing between the gold hemispheroids and the silicon surface.

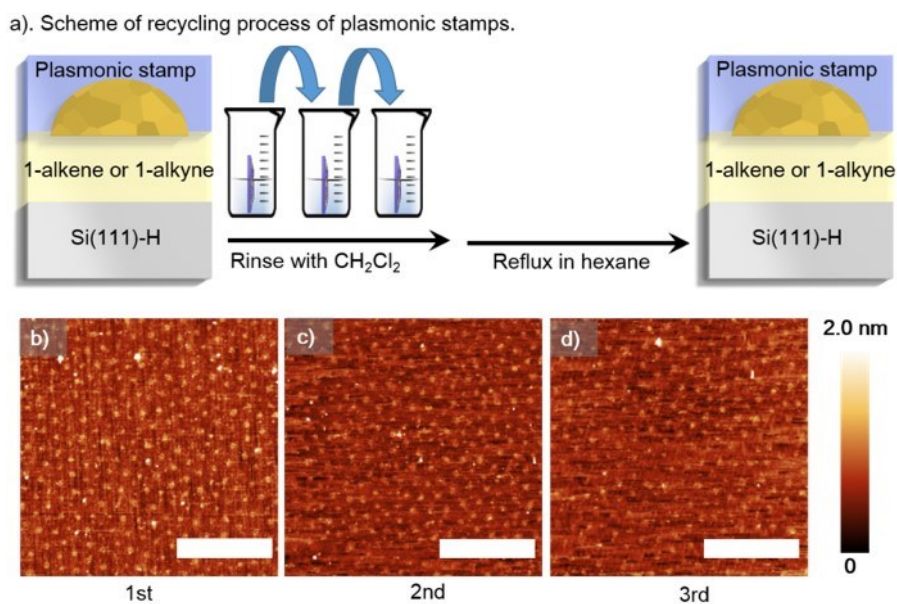


**Figure 3.21.** a): Scheme of recycling process of plasmonic stamps. Prior to the next stamping, the stamp was soaked in dichloromethane for three times and then washed in hexane for at least 6 hours. b-d): AFM height micrographs of 1-dodecene stamped nanopatterns on Si(111)-H surfaces with recycled plasmonic stamps. Scale bar: 400 nm. BCP: PS-*b*-P2VP (125 k-*b*-58.5 k)

### 3.4 Conclusions

Localized surface plasmons in hemispheroidal gold nanostructures, embedded within an optically transparent plasmonic stamp, can be used to drive hydrosilylation of alkenes and alkynes on silicon surfaces, upon illumination with white light with wavelengths that corresponded to the absorption profile of the gold nanoparticles. The gold nanopatterns were created *via* block copolymer self-assembly, but could presumably be produced through other lithographic nanopatterning approaches. The resulting patterns on the silicon surface mirror those of the parent gold nanopattern within the plasmonic stamp, and demonstrate the localized nature of the reaction. Other surface reactions that are driven by locally generated charges may also be promoted by the plasmonic stamp, and the influence of edges, points, and other features that result in increased electric field effects could provide a rich source of reactivity.

The most likely mechanism for the observed hydrosilylation is based upon the high intensity local electric field of the gold nanoparticle LSPRs leading to the generation of electron-hole pairs in the silicon, resulting in nucleophilic attack by the alkene, and formation of the Si-C bond. Details and discussion of possible mechanisms will be presented in Chapter 4.

### 3.5 Experimental Section

#### Materials

All reagents and materials were used as received unless otherwise specified. Si wafers [111, prime grade, p-type, B-doped,  $\rho = 1\text{-}10\ \Omega\text{-cm}$ , thickness = 600-650  $\mu\text{m}$ ] were purchased from WRS Materials Inc. Millipore water (resistivity: 18.2 M $\Omega$ ) was used for the preparation of all aqueous solutions and for rinsing samples. Block copolymers (BCPs), all of the composition polystyrene-*block*-poly-2-vinylpyridine (PS-*b*-P2VP) with three different molecular weights (125 k-*b*-58.5 k, 91.5 k-*b*-105 k, and 190 k-*b*-190 k), were purchased from Polymer Source Inc. The starting materials for preparing *h*-PDMS (trimethylsiloxy terminated vinylmethylsiloxane-dimethylsiloxane (VDT-731), 25-35% (methylhydrosiloxane) 65-70% (dimethylsiloxane) (HMS-301), and Pt divinyltetramethyldisiloxane (SIP6831.2) were purchased from Gelest Corp., and 184 PDMS from Dow Corning. 2,4,6,8-tetramethyl-2,4,6,8-tetravinylcyclotetra-siloxane, 30% NH<sub>4</sub>OH (aq.), 30% H<sub>2</sub>O<sub>2</sub> (aq.), KAuCl<sub>4</sub>·xH<sub>2</sub>O (99.999%), 1,4-butanedithiol (>97%), trichloro(1H,1H,2H,2H-perfluorooctyl)silane (98%), 1,7-octadiene(>99.0%), 1-dodecene (>99.0%) and 1H,1H,2H-perfluoro-1-decene (99.0%) were obtained from Sigma-Aldrich. 1-Dodecene, 1,7-octadiene, and 1H,1H,2H-perfluoro-1-decene were passed through a column of dried alumina to remove peroxides, and

deoxygenated with a stream of nitrogen gas. Optical filters (CW526 or CW440, CW referring to center wavelength) were purchased from Edmund Optics Inc.

### **Plasmonic Stamping on Hydride-terminated Si(111) Surface**

Hydride-terminated Si(111) samples were obtained by immersing the RCA-processed Si(111) wafers in degased 40% NH<sub>4</sub>F(aq.) for 5 min, then immersed in deoxygenized water for 10 s, and dried with a stream of argon. In a nitrogen-filled glovebox, a hydride-terminated Si(111) wafer was placed on a clean glass slip, and then neat alkene (30  $\mu$ L) was carefully dropped from a microliter syringe on the hydride-terminated Si(111) surface. The plasmonic stamp was applied on the surface and another glass slip cover was placed on top of the stamp. To apply reproducible pressure, two paper clamps were applied on both sides to fix the sandwich structure, as shown in the photograph in the Figure 3.7c. White light from a 300 W ELH bulb was focused through a PCX lens, filtered by band-pass filters (CW526 or CW440), and shone on the sandwiched sample for 60 min with the intensity of 50 mW/cm<sup>2</sup> for the CW526 filter and 40 mW/cm<sup>2</sup> for CW440 filter. After the stamping steps, the wafer was rinsed thoroughly with dichloromethane and dried with a stream of argon gas prior to further analysis.

## Thiol-ene Chemistry and Gold Nanoparticle Binding

Citrate-capped gold nanoparticles were fabricated *via* a seed-mediated growth method following a procedure described elsewhere.<sup>255</sup> The procedure of visualization of a alkyl-patterned Si(111)-H substrate with gold nanoparticles closely follows the method previously described,<sup>164</sup> and was slightly modified here. Briefly, a hydride-terminated Si(111) wafer was firstly stamped with 1,7-octadiene to form a pattern with terminal alkene groups. The sample was then immersed in concentrated KOH (4 mol/L) for 30 s, and soaked overnight in oxygen-saturated water, to remove all remaining Si-H<sub>x</sub> groups. The alkene-terminated patterned regions then underwent a thiol-ene reaction by immersing the sample in 0.1 mL of neat 1,4-butanedithiol, with illumination of ultraviolet visible light (254 nm, UV pen lamp, Model 11SC-1) for 30 min, followed by rinsing with dichloromethane. Lastly, the thiol-patterned sample was immersed in a colloidal solution containing 10 nm citrate-capped Au nanoparticle for 3 h, and then rinsed with toluene and dried with a stream of nitrogen gas. For the Au electroless deposition, the thiol-patterned sample was immersed in a beaker containing 10 mL of 0.1 mM HAuCl<sub>4</sub> (aq) for 30 min, followed by the addition of 100 μL of 0.1 mM ascorbic acid. The processed surface was finally rinsed with DI water and dried with a stream of nitrogen gas.

# 4

## Plasmonic Stamp Lithography III: Mechanisms

### 4.1 Introduction

Plasmonic stamp fabrication and applications for lithography on silicon surfaces have been demonstrated and described in Chapters 2 and 3. An SPR-assisted mechanism was proposed to drive the localized hydrosilylation under the illumination of filtered visible light. In order to further understand the mechanism, this chapter describes a series of experimental and computational experiments including investigations regarding doping effects, Au-Si distance studies, among other experiments, as well as FDTD (finite-difference time-domain) simulations. Based on the discussion of the results and possible mechanisms, it was found that the SPR-assisted hydrosilylation can be explained *via* electric near-field induced electron-hole pair generations. First, the various mechanisms regarding energy transfer between metals and semiconductors will be briefly reviewed.

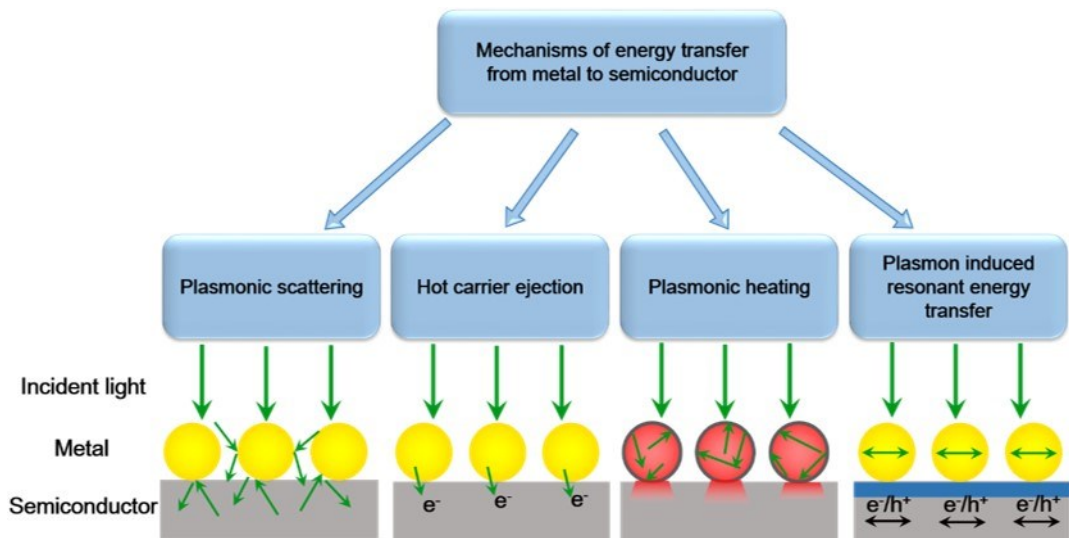


**Figure 4.1.** Various mechanisms for energy transfer between metals and semiconductors.

## 4.2 Conventional Energy Transfer Mechanisms

As discussed previously in Chapter 1, plasmonic metal nanostructures provide a promising pathway to improve the efficiency of solar energy conversion, and have been applied to a variety of systems for the solar-to-chemical conversion.<sup>120, 125, 256-258</sup> Therefore, investigations on energy transfer between a metal and a semiconductor are becoming increasingly useful in order to understand the mechanisms in the targeted system. Resonant under illumination, the “hot” surface plasmon can transfer its energy to the surrounding matrix (e.g. semiconductors) *via* radiative and non-radiative decay.<sup>120, 125</sup> Depending on geometric considerations (size, shape, position/distribution, etc.), and relative energy levels between metals and dielectrics, there are several reported energy transfer pathways between a metal and a semiconductor, such as plasmonic light scattering,<sup>259-262</sup> hot carriers,<sup>125, 263-265</sup>

plasmonic heating,<sup>266-268</sup> and the recently demonstrated plasmon-induced resonant energy transfer,<sup>256, 269-272</sup> as shown in Figure 4.1. Note that each mechanism may co-exist with energy conversion, and the dominant pathway can change during the reaction/energy conversion.<sup>120, 269</sup> In the following part of the introduction, these mechanisms will be discussed in detail.

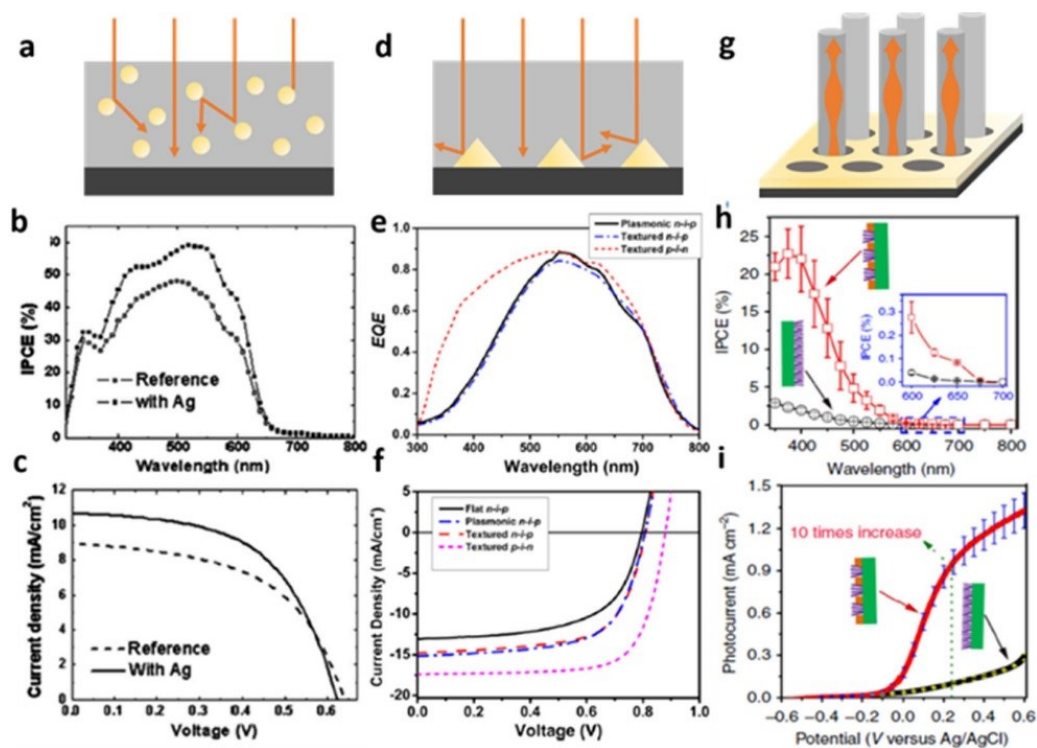


**Figure 4.2.** Schematic geometries of light scattering for applications in photovoltaics and photocatalysis. Reprinted with permission from ref. 269. Copyright © 2016 American Chemical Society.

### 4.2.1 Light Scattering

In well-defined systems consisting of metal-semiconductor nanostructures, plasmonic light scattering has been an effective strategy for light trapping enhancement in a semiconductor that leads to improved efficiencies in photovoltaics<sup>259, 261, 273-275</sup> and photocatalysis.<sup>270, 274, 276</sup> Due to the presence of plasmonic nanostructures, multiple reflections of the incident light can be expected to trap incident light in a semiconductor and increase the optical thickness while keeping the physical thickness of the film.<sup>126, 259, 273, 274</sup> Therefore, geometric designs for light scattering have become one of the most important strategies. As described in Figure 4.2, several geometries of plasmonic nanostructures have been applied to improve light trapping. Figures 4.2a-c describe geometries of metal nanoparticles embedded in a semiconductor, in which Ag nanoparticles are incorporated into the photoactive layer in organic solar cells, in order to maximize the light trapping as well as reduce the charge recombination losses.<sup>277</sup> Another geometry for plasmonic scattering is presented in Figures 4.2d, in which the plasmonic nanostructures are designed to be above or underneath the photoactive layer and act as a forward scattering layer or as a back reflector in the case of Figures 4.2d-f.<sup>274</sup> In addition to nanoparticles, plasmonic scattering can also be applied to metal films, in which surface plasmon polaritons (SPP) are generated and trapped within metal and semiconductor thin films.<sup>270</sup> Note that in order to design an effective plasmonic

nanostructure for light scattering using LPSR, the size of plasmonic metal nanoparticles should be larger (>50 nm) to ensure the multiple reflections inside the semiconductor.<sup>278</sup> Shapes of the plasmonic nanostructures with multiple resonant directions (quadrupole or higher order modes), as well as large-scale nanopatterns can also facilitate broad-band light scattering.<sup>120, 126, 279</sup>

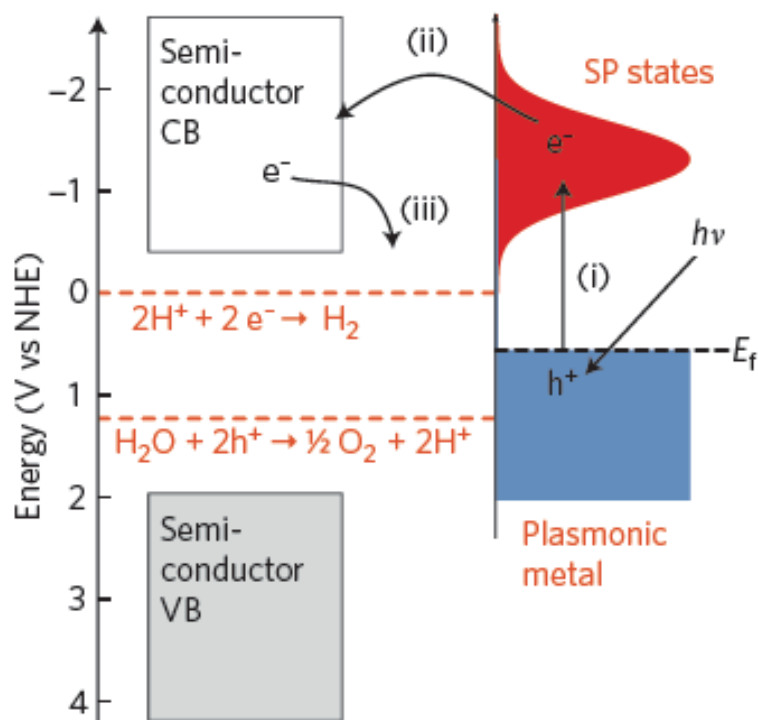


**Figure 4.3.** Energy diagram for water splitting *via* the hot carrier injection mechanism. CB: conduction band. VB: valence band. SP: surface plasmon. Reprinted with permission from ref.

120. Copyright © 2011. Nature Publishing Group.

#### 4.2.2 Hot Carrier Injection

When the plasmonic metal is designed to be in direct contact with the semiconductor (as opposed to an insulator layer in between, which will be discussed below), a Schottky barrier at the metal/semiconductor interface is formed.<sup>280, 281</sup> When resonant under illumination, the plasmon can generate hot charge carriers (electrons or holes) that are sufficiently energetic to overcome the Schottky barrier and be injected into semiconductors at the interface.<sup>125, 263, 269, 281, 282</sup> The separated carriers can then be utilized for photocatalytic applications such as water splitting.<sup>258, 283-287</sup> In order for the hot carrier mechanism to be effective, direct contact of a metal and a semiconductor is necessary, as the mean free path for the hot carrier is usually only a few nanometers and the bulk carriers will recombine before migrating to the interface, in spite of a small portion of electrons can tunnel through the Schottky barrier with low efficiency.<sup>125, 282</sup> The energy alignment is also crucial for the hot carrier transfer. In an example of water splitting using direction of the plasmonic nanostructures as shown in Figure 4.3, the energy levels for noble metal falls about 1.0~ 3.5 eV above Fermi level, which is above the energy window for water splitting (-1.0~0 eV) with the energy level alignment.<sup>120</sup> Therefore, the hot electron carriers should only be valid for the transfer from the metal to the semiconductor for hydrogen generation.

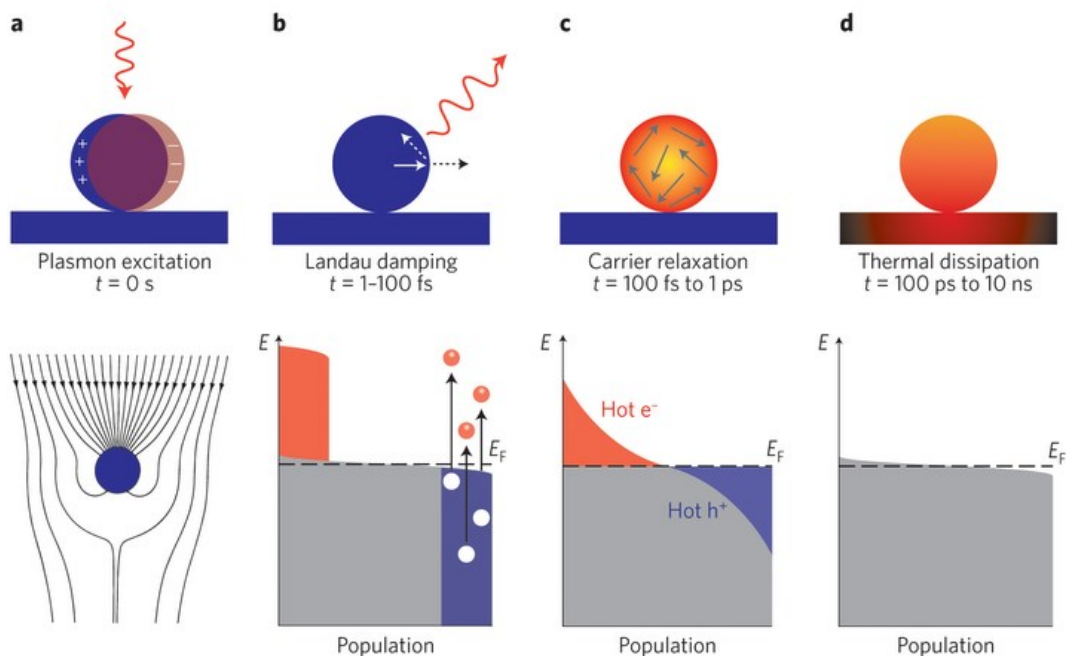


**Figure 4.4.** Photo excitation and relaxation process of SPR induced hot carriers. Reprinted with permission from ref. 257. Copyright © 2014 Nature Publishing Group.

### 4.2.3 Plasmonic Heating

In Chapter 1 various applications of surface plasmon resonance were reviewed, and discussed the application in photothermal therapy due to the local heating effects that were induced by SPR of plasmonic metal nanoparticles.<sup>131-134</sup> Figure 4.4 describes the kinetic processes for the excitation and relaxation of hot carriers induced by SPR of a plasmonic metal nanoparticle.<sup>125</sup> Plasmonic local heating can be observed when the hot carriers are trapped inside the metal nanoparticle during the decay process, leading to a local temperature increase at the surface of the metal nanoparticle and its surrounding environment, as shown in Figures 4.4c-d.

Depending on the intensity of incident light and surrounding dielectric materials, the temperature increase can be efficient for water steam generation<sup>266, 268</sup> and the killing of cancer cells *in vivo*.<sup>131-134</sup>

#### **4.2.4 Plasmon-induced Resonant Energy Transfer**

Plasmonic metal nanostructures offer a promising route to improve the solar energy conversion efficiency of semiconductors. Different from the previously discussed mechanisms, the plasmon-induced resonant energy transfer refers to the energy transfer from metal to semiconductor by dipole-dipole coupling of excited surface plasmons, and subsequently induce the formation of electron-hole pairs in the semiconductor.<sup>256, 269, 284</sup> The PIRET has two important requirements for the geometry of the system: First, overlapping of the energy density of the metals and semiconductors; and second, a thin insulating layer between the metal and the semiconductor. This phenomenon was firstly proposed by Wu's group in order to interpret the enhanced photocatalyst performance in their gold-SiO<sub>2</sub>-Cu<sub>2</sub>O structures.<sup>271</sup> They found that in the presence of a thin insulating layer of SiO<sub>2</sub>, the photocatalysis efficiency is consistent with their extinction spectra. With these interesting results and the charge carrier calculations, they proposed that the dipole-dipole interaction from surface plasmon resonance lead to the plasmon-induced energy transfer from Au to Cu<sub>2</sub>O and the resulting electron-hole pair generation in the semiconductor, as described in Figure 4.5b.

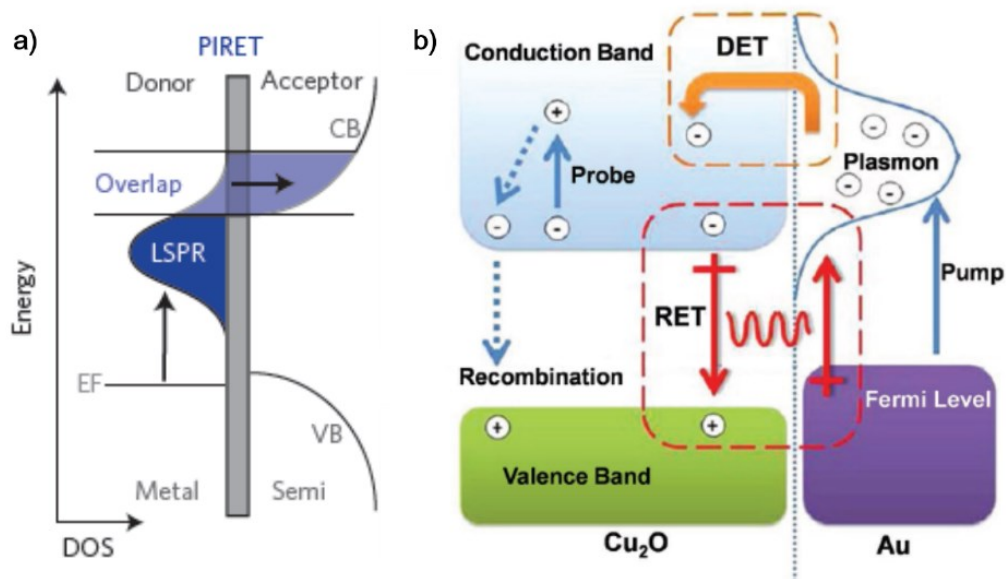


**Figure 4.5.** a) Plasmon-induced resonant energy transfer (PIRET). The plasmon is excited and its energy transfers from the metal to the conduction band of the semiconductor. b) Photocatalytic activity is enhanced by PIRET from Au to Cu<sub>2</sub>O. Reprinted with permission from ref. 256. Copyright © 2015 Nature Publishing Group, and from ref. 271. Copyright©2012 American Chemical Society.

So far there are few reports of plasmon-driven hydrosilylation on silicon surfaces,<sup>156, 251</sup> and thus this intriguing reaction pathway requires further study as it could provide a new route towards catalytic surface functionalization using plasmonically active materials, as the materials are not consumed or changed during the course of the reaction. In this following discussion, the mechanism of action of gold plasmons on the chemical reactivity of a proximal silicon surface was re-evaluated and refined in light of recent work in the area of plasmonics, which is probably due to the

plasmon-induced intense electric near-field from the patterned Au hemispheroids in the plasmonic stamp to the hydrosilylated silicon surface.

### **4.3 Results and Discussion**

From the results of plasmonic stamp-assisted hydrosilylation on silicon surfaces, it appears that the local hydrosilylation reaction is driven by the plasmon resonance of the Au nanoparticles. As such, energy is being transferred from the Au nanoparticles/plasmons to the 1-dodecene/Si(111)-H interface. Upon excitation, the plasmon can decay radiatively through resonant plasmonic scattering, or non-radiatively *via* the generation of an electron-hole pair, typically referred to as hot carriers. These hot carriers can be directly injected into the surrounding medium, or they can recombine, which results in local heating of the nanoparticle. Lastly, electron-hole pairs can be directly generated in silicon as a result of the resonant energy transfer of surface plasmon, which is localized to the neighborhood of the gold nanoparticle. Given that all four of these mechanisms (resonant photon scattering, nanoparticle plasmonic heating, hot carrier injection and plasmon-induced electron-hole pair generation) could be driving the local hydrosilylation reaction, their relative contributions are discussed below based on the obtained experimental results to figure out whether the previously introduced mechanisms fits the SPR-assisted plasmonic stamping on silicon surfaces.

### 4.3.1 Discussion of Plasmonic Scattering Mechanism

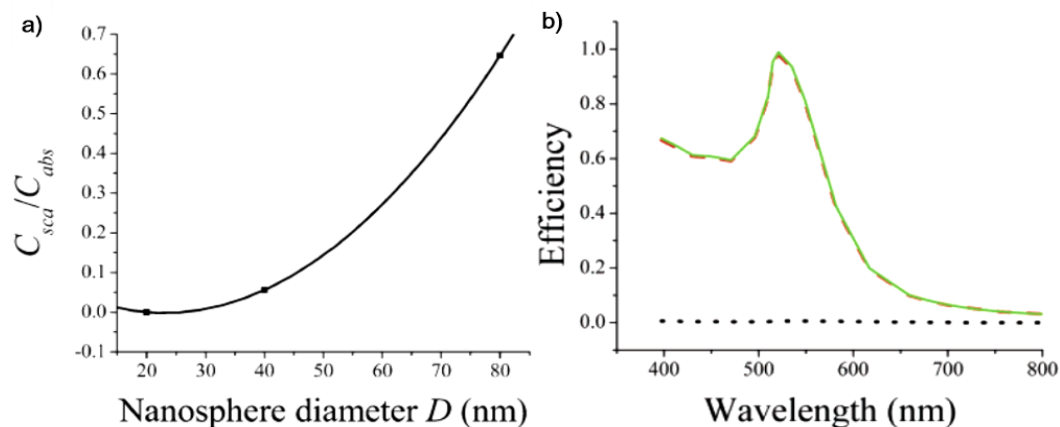


**Figure 4.6.** a) Calculated cross-section coefficient scattering/absorption ratio of Au nanoparticles. b) Calculated spectra of scattering (black), absorption (red) and total extinction (green) of a gold nanoparticle with 20 nm in diameter. Reprinted with permission from ref. 279.

Copyright © 2006 American Chemical Society.

Efficiency enhancement due to the resonant photon scattering or forward light scattering of metal nanoparticles has been suggested to be taking place in light scattering-enhanced solar cells.<sup>20-22</sup> When metal nanoparticles are located on a solar cell surface, the secondary radiation of incident electromagnetic energy into the active layers of solar cells, referred to as the forward light scattering, can increase the effective optical length by light trapping in the active layers, which could lead to an increased rate of electron-hole pair generation at the silicon surfaces.<sup>261</sup> As mentioned above, particle sizes should be larger than 50 nm to facilitate plasmonic scattering, however, the size of the Au nanoparticles in the plasmonic stamp is

10~15 nm, which is in the range in which LSPR absorption would be dominant; the forward scattering intensity would be less than 0.1% of incident light, according to previously reported simulations that are shown in Figure 4.6.<sup>130, 261, 279</sup>

#### 4.3.2 Discussion of Plasmonic Heating Mechanism

The next mechanism to be considered is *in-situ* plasmonic heating, which could result in a local increase of temperature of the gold nanoparticles due to the strong light absorption at the plasmon resonance, which is dissipated as heat.<sup>132, 154, 268, 288</sup> For thermal heating to play a role in hydrosilylation, the silicon surface would need to reach temperatures in excess of 100 °C, within the timescale of experiments performed in this work.<sup>226, 227</sup> The temperature increase,  $\Delta T$ , of a single isolated gold nanoparticle can be estimated using the conventional model,<sup>288</sup>

$$\Delta T = \frac{\sigma I}{2\pi k D}$$

where  $\sigma$  is the particle absorption cross section,  $I$  is the incident light intensity,  $k$  is the thermal conductivity of the surrounding medium and  $D$  is the nanoparticle diameter. Assuming a scattering cross section of 500 nm<sup>2</sup>, a thermal conductivity of 0.15 W/m K (corresponding to PDMS), a nanoparticle diameter of 15 nm and an intensity of 50 mW/cm<sup>2</sup>, the predicted temperature increase would be  $1.8 \times 10^{-5}$  °C.

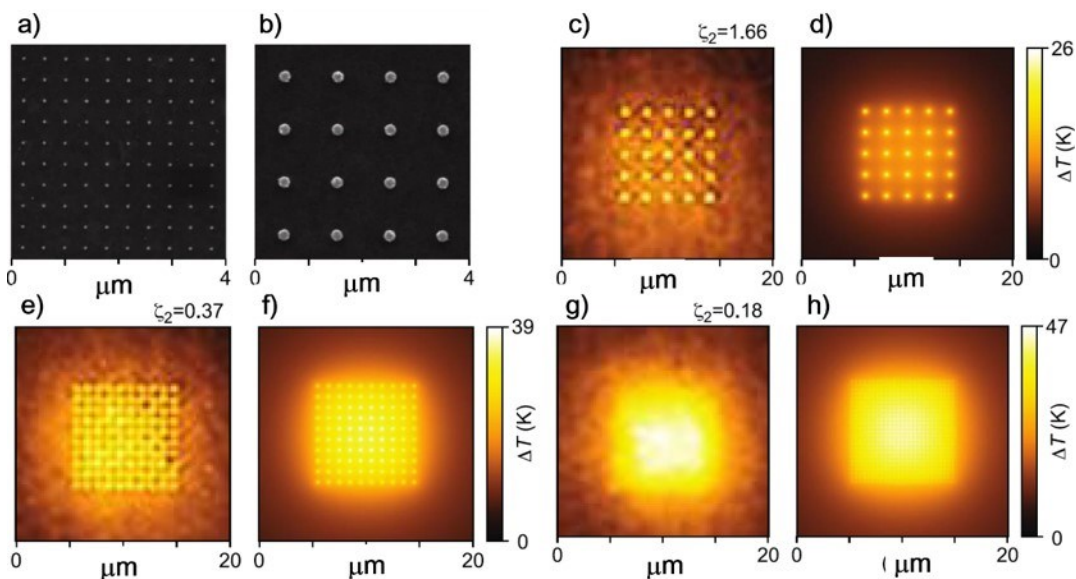


**Figure 4.7.** a-b): SEM images of Au nanopatterns with spacings of a) 200 nm and b) 400 nm.

c,e,g) Experimental and d,f,h) FDTD simulation of plasmonic heating and delocalization.

Reprinted with permission from ref. 267. Copyright © 2013 American Chemical Society.

It is worth noting that steam generation has been observed for dilute solutions of light absorbing nanoparticle using moderate light intensities of  $\sim 10^5$  mW/cm<sup>2</sup>, but this phenomenon has been shown to be a result of enhanced light absorption due to efficient volume scattering between nanoparticles in solution.<sup>154</sup> A similar light trapping effect is unlikely to play a role here since the nanoparticles are isolated on a single plane. Moreover, in order for patterned surface hydrosilylation to occur, it would be necessary for the temperature increase to be localized directly underneath the nanoparticles such that the surrounding silicon does not react. This effect has been extensively studied by Baffou *et al.*, who showed that localized heating around the nanoparticles could only take place if they were sufficiently far apart relative to

the total number of illuminated nanoparticles, due to heat diffusion between nanoparticles, as shown in Figure 4.7.<sup>267</sup> Specifically, it was shown through both simulation and experiment that localized heating could only be achieved if

$$p^2/3LR \gg 1,$$

where  $p$  is the average centre-to-centre spacing,  $R$  is the nanoparticle radius and  $L$  is the diameter of the illuminated area. Given that  $p^2/R \sim 650$  nm, while the illuminated diameter is on the order of millimeters, it can be concluded that any temperature increase due to nanoparticle heating would be uniformly distributed across the substrate surface.

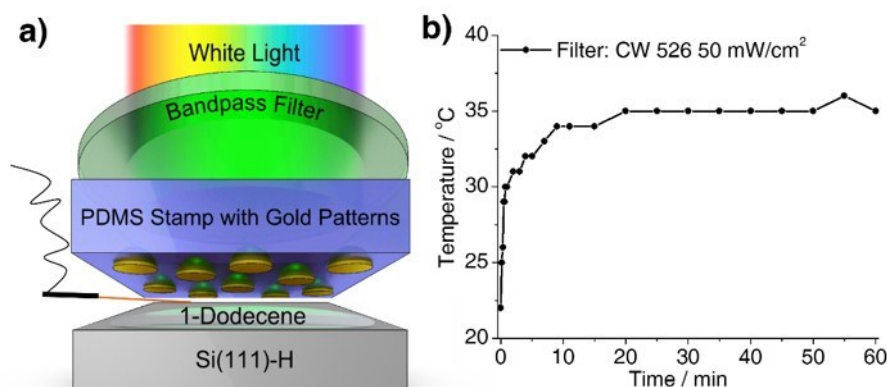


**Figure 4.8.** Macroscale temperature measurements. a) Scheme of the temperature measurement setup. b) Temperature profile observed with the increase of illumination time. (Band pass filter: CW526, 50 mW/cm<sup>2</sup>). The thermocouple was sandwiched between plasmonic stamp and silicon surface as per the described experimental procedure.

In addition, the temperature increase was also measured on the macroscale. Illumination of the plasmonic stamp/1-dodecene/Si(111)-H sandwich with filtered white light (50 mW/cm<sup>2</sup>, CW526) resulted in only a minor temperature change from room temperature to a maximum temperature of ~35 °C in about 20-30 minutes, as shown in Figure 4.8, as measured with a small thermocouple localized between the plasmonic stamp and silicon. This temperature increase is insufficient to initiate thermal hydrosilylation on flat surface, not to mention the formation of patterned alkyl molecules.

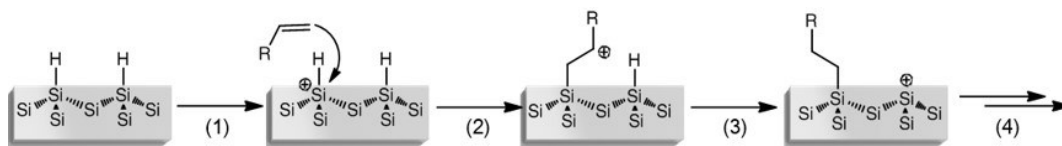


**Figure 4.9.** Scheme of the possible carrier injection mechanism.

### 4.3.3 Discussion of Hot Carrier Injection Mechanism

The third mechanism to consider is hot carrier injection from the gold nanoparticles into the surrounding medium. In the event of non-radiative decay of the plasmon (which is the dominant plasmon decay mode for nanoparticles much smaller than the plasmon wavelength) an energetic electron-hole pair is formed, typically referred to as hot carrier generation.<sup>125, 265</sup> These hot carriers have been extensively studied in catalytic water-splitting as mentioned previously, where it has been shown

that the hot carrier are directly injected into the semiconductor surface, facilitating the water-splitting reaction.<sup>5, 31-35</sup> In the case of hydrosilylation, if a hole is injected into the silicon surface from the gold nanoparticle, the hydrosilylation reaction can proceed *via* nucleophilic attack by an alkene on a positively charged surface silicon site, as has been repeatedly postulated.<sup>219</sup> However, it is necessary to consider the presence of the non-conducting organic layer of 1-dodecene sandwiched between the gold nanoparticles and the silicon surface, which would be expected to impede charge transfer to the silicon. Although the 1-dodecene is layer is non-conducting, recent work has revealed that the plasmonically generated hot holes in gold can have energies of  $\sim 7.5$  eV (w.r.t vacuum),<sup>264</sup> and as such it is possible that some of these hot holes could be injected into the silicon. These injected holes could then lead to hydrosilylation *via* nucleophilic alkene attack and silicon-carbon bond formation,<sup>219</sup> as shown in Figure 4.9. Although direct charge transfer of hot carriers from the gold nanoparticle to the silicon surface appears to be unlikely in this scenario, further investigation is necessary to conclusively determine the role of these hot carriers.

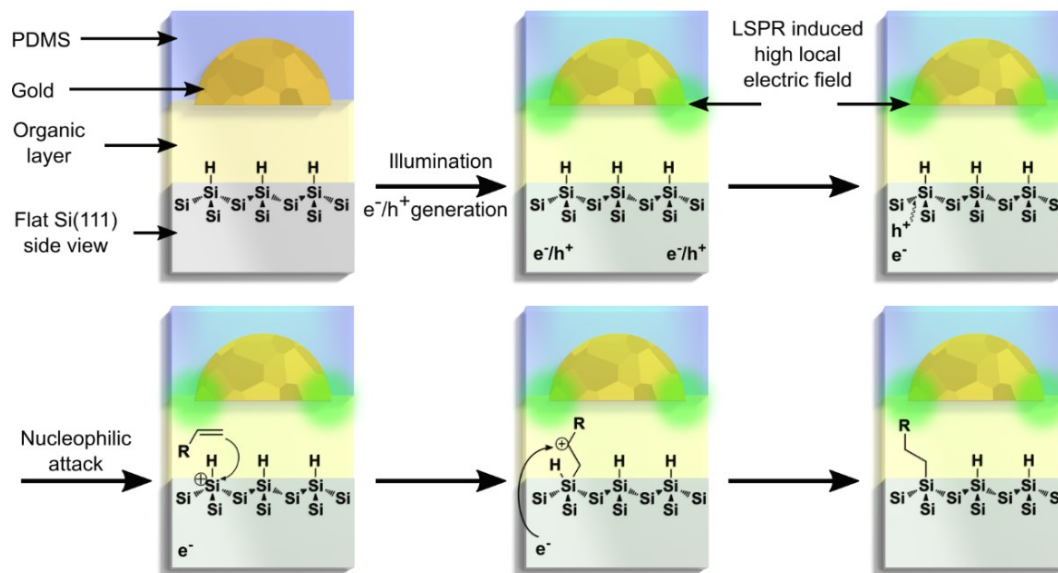


**Figure 4.10.** Schematic mechanism of plasmonic stamp-assisted hydrosilylation driven by the LSPR induced high local electric field.

#### 4.3.4 Proposed Mechanism for the Plasmonic Stamping

In their earlier work on gold nanoparticle-induced hydrosilylation, Sugimura and co-workers invoked plasmonic excitation upon illumination, and subsequent conversion of this light energy and transfer to the silicon surface, in close proximity to the spherical nanoparticle. In our later publication on plasmonic stamping, we suggested the role of the enhanced electric field to produce charge carriers, electron-hole pairs, in the silicon.<sup>156</sup> The effect of the highly concentrated electromagnetic field produced by the LSPR is considered. It has been shown that the rate of electron-hole pair generation in a semiconductor is proportional to the local intensity of the electric field.<sup>289, 290</sup> Given that the electric field enhancement is on the order of  $\sim 10^3$  at the edges of the nanoparticle,<sup>120</sup> the relative concentration of electron-hole pairs

at the silicon surface (within the neighborhood of the gold nanoparticle) would also be expected to  $\sim 10^3$  times higher. As such, the kinetic rate of the hydrosilylation reaction would proceed much faster in these areas of increased electron-hole pair concentration, given that the electron-hole pairs drive the reaction, as outlined in Figure 4.10.

To determine if the plasmon resonance was fundamental to the observed hydrosilylation, samples were illuminated with light having no spectral overlap with the plasmon resonance of the gold nanoparticles. As determined by UV-vis spectroscopy of the stamp that is presented in Chapter 2, the absorbance maximum of the LSPR stamp was observed at 530 nm. To this end, the same light source was used, but with a band pass filter (CW 440 nm) centered around 440 nm full-width at half-max (FWHM) of 90 nm, which allows passage of higher energy light, but cuts off just below the absorbance of the plasmon, as indicated in Figure 4.11. This experiment resulted in no obvious pattern transfer *via* hydrosilylation on the Si(111)-H surface, as demonstrated by AFM characterizations in Figure 4.11.

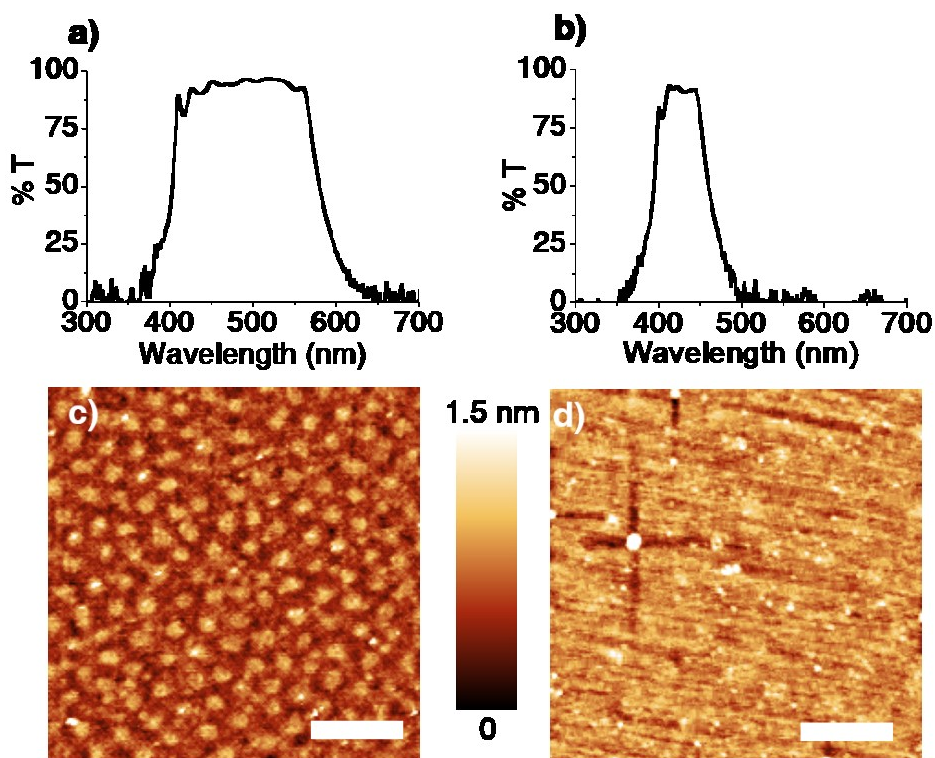


**Figure 4.11.** AFM height maps of stamped Si(111)-H surfaces using band-pass filters with different wavelength ranges: a, c) CW 526, 50 mW/cm<sup>2</sup> and b, d) CW 440, 40 mW/cm<sup>2</sup>). The block copolymer used for the stamp was PS-*b*-P2VP (125 k-*b*-58.5 k). Scale bar is 200 nm.

#### 4.3.5 Simulation

Examining the AFM micrographs of the patterned Si(111)-H surfaces with alkyl or alkenyl groups, the hydrosilylated patches appear to be more akin to rings upon close inspection as opposed to uniform regions, particularly those produced with the smaller gold hemispheroids, as shown in Figures 4.12a and b. Visualization of hydrosilylated silicon surface also reveals ring-like nanopatterns by gold electroless deposition that was described in Chapter 3. The formation of rings resulting from

plasmonic stamp-induced hydrosilylation points to the influence of the edges of the hemispheroids of gold, embedded within the stamp. As has been previously published for hemispheroids of gold,<sup>291-294</sup> FDTD simulations show an enhancement of the electric field surrounding the edge of the nanoparticle. The edges of the gold nanospheroids induce localized hydrosilylation on the hydride terminated silicon surface.

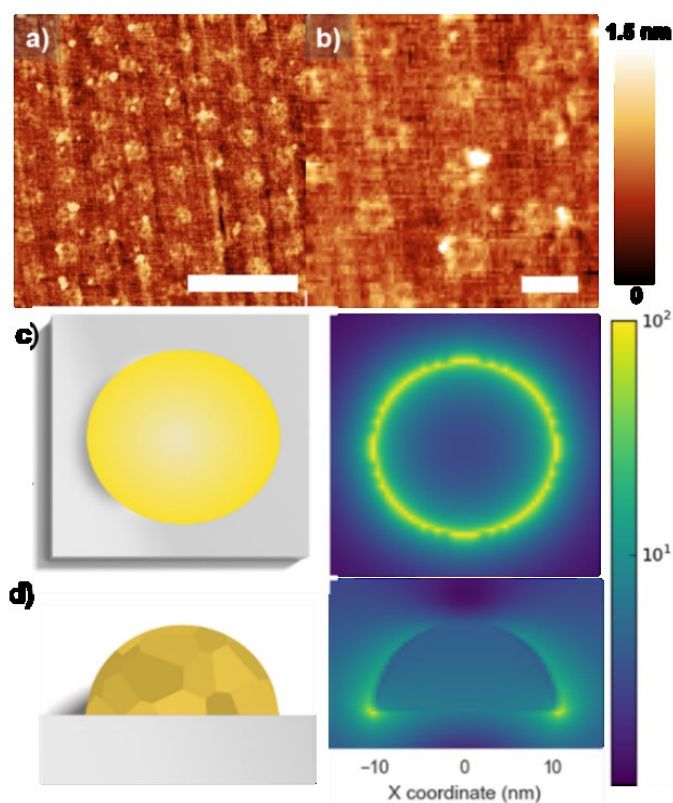


**Figure 4.12.** (a) AFM micrographs of 1-dodecyl patterned Si(111)-H surface after plasmonic stamping; (b) Zoomed-in AFM micrograph shows ring-like dodecyl patterns on Si(111)-H surfaces. BCP: PS-*b*-P4VP (20k -19k) Scale bars: 200 nm for a); 20 nm for b). c, d) FDTD simulations of a single gold hemispheroids (20 nm in diameter) from top and side views.

### 4.3.6 Ferrocene Quenching

To support a hydrosilylation mechanism of plasmon-induced reactive carriers in the silicon, trace amounts of a charge transfer quenching agent, ferrocene, was added to the 1-dodecene; if such a mechanism were to be in play, the ferrocene should effectively quench the reaction *via* electron injection because the holes required to drive the hydrosilylation mechanism would be eliminated *in-situ*.<sup>218, 225, 244</sup> Addition of 2.0 % ferrocene (w/w) to the 1-dodecene resulted in no visible pattern by AFM and an unchanged contact angle showed in Table 4.1, suggesting *ex situ* hole quenching *via* electron transfer from the ferrocene, providing an addition piece of evidence to substantiate the mechanism based upon electron/holes.

**Table 4.1.** Contact angle measurements of hydrosilylated silicon surface with and without the quenching agent addition. \* Average of at least 16 measurements

Samples	Light Intensity	Contact Angle* (Degree) 1-dodecene	Contact Angle* (Degree) 1H,1H,2H- perluoro-1-decene
Si(111)-H (Control)	Dark		83.1 ± 0.7
Si(111)-H + neat alkene + plasmonic stamp	526 nm filter for 1 h Intensity: 50 mW/cm <sup>2</sup>	97.8 ± 3.3	105.4 ± 2.7
Si(111)-H + 2.0 wt% ferrocene in alkene + plasmonic stamp	526 nm filter for 1 h Intensity: 50 mW/cm <sup>2</sup>	84.5 ± 1.8	85.1 ± 2.0

### 4.3.7 Au-Si Distance Studies

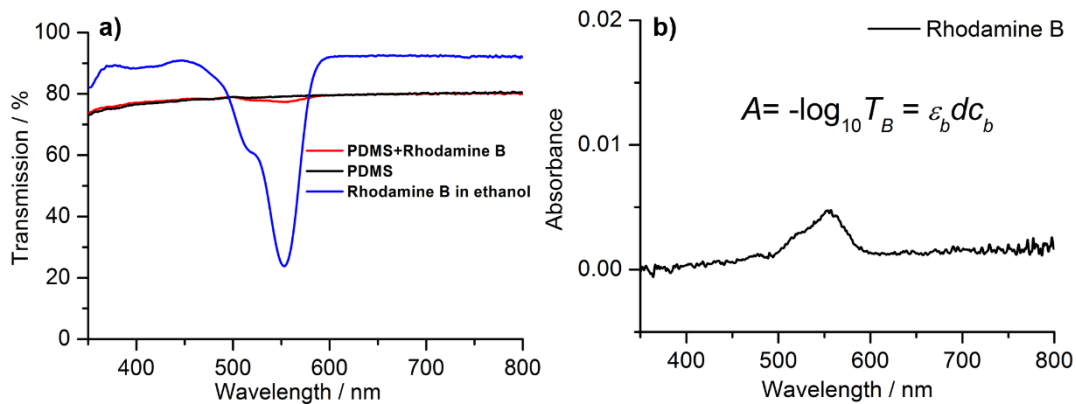


**Figure 4.13.** a) UV-vis spectra of the stamps clamped between two glass slips before and after the addition of Rhodamine B. b) Absorbance of Rhodamine B, calculated from their UV-vis spectra.

In order to roughly determine the scale of the distance between Au and Si during the stamping process, a trace amount of Rhodamine B (an organic dye) was mixed with alkenes to reach a concentration of 0.02 M. 30  $\mu$ L of the mixed solution was then sandwiched between glass slip and a transparent PDMS stamp (Au free), and then characterized by UV-vis spectroscopy. Figure 4.13 showed the UV-vis spectra comparison with and without the Rhodamine B. The difference of these two absorption spectra indicates the presence of thin layer of solution in the sandwich structure. Thus, the distance between Au and Si can be roughly determined by calculating the thickness of the sandwiched solution layer with Beer's law<sup>295</sup>:

$$A = -\log_{10} T_B = \epsilon_b d c_b$$

Where  $\epsilon_b$  is the absorption coefficient of Rhodamine B, which is  $106,000 \text{ cm}^{-1} \text{ M}^{-1}$  at 545 nm from reported data;<sup>296</sup>  $d$  is the thickness of the solution layer;  $A$  and  $T$  are absorption and transmission of the solution layer. According to the equation 1 and the obtained values from UV-vis spectra ( $A = 0.004$  at 543 nm), the calculated thickness is 16.5 nm. Although the accurate Au-Si distance remains difficult to determine due to a host of variable factors (e.g. thickness of organic molecule layer, uneven pressure, H-termination, etc.), the distance that roughly evaluated with this method falls in the magnitude order to facilitate the FIRET pathway.

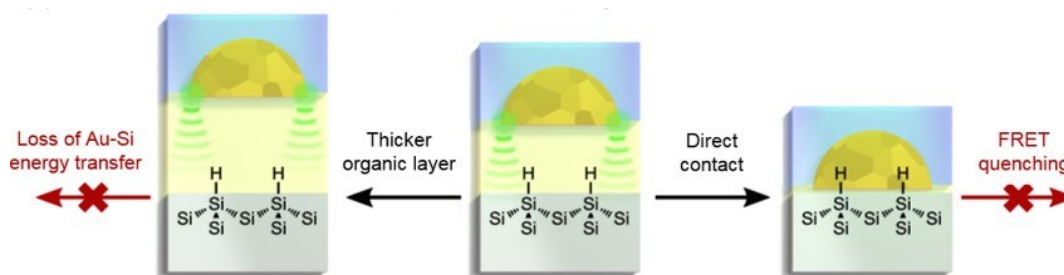


**Figure 4.14.** Distance dependence of the plasmonic stamping. FRET: Förster resonance energy transfer.

The influence of electric near-field induced by LSPR to the silicon surface is dependent upon the thickness of the dielectric, the alkene/alkyne located between the gold hemispheroid and the silicon surface. The distance calculated from UV-vis spectra indicated that the average thickness of the alkene/alkyne layer was less than 20 nm. Note that this calculated distance should be regarded as an average value over a large area ( $7\sim 110 \text{ mm}^2$ ), and owing to the heterogeneity of pressure, there

will be, consequently, variations of the thickness of the alkene/alkyne layer. Since there are areas on the silicon surface where no patterning is observed, the assumption is that hydrosilylation can only occur in those regions where the distance between the stamp and the Si(111)-H surface is small, on the order of 4-10 nm from the reported work.<sup>120, 289, 297, 298</sup> Other research also imply that when the distance between Au and silicon surfaces is too close (in contact or  $< 1$  nm), the Förster resonance energy transfer (FRET) between metals and semiconductors can quench local excitons on the semiconductor surface.<sup>120, 256</sup> Scheme of the Au-Si distance effects on the plasmonic stamp lithography are summarized in Figure 4.14.

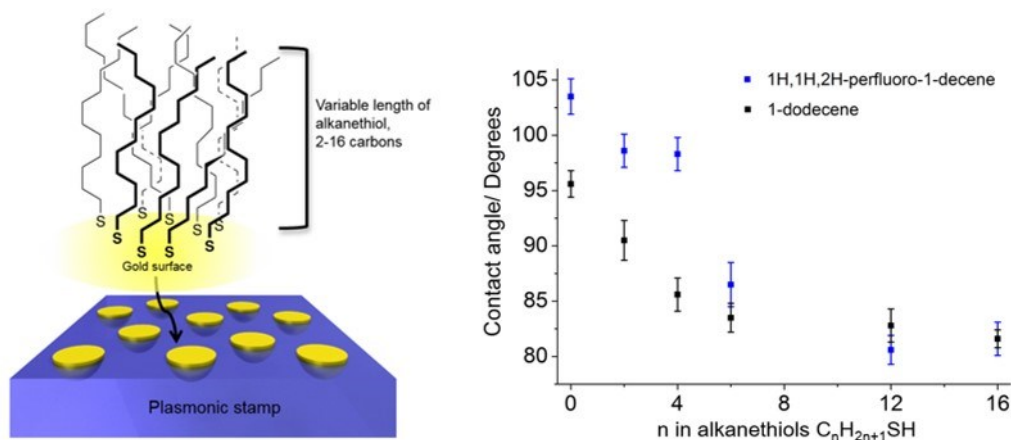


**Figure 4.15.** Scheme and plots of water contact angle measurements of 1-dodecene (black) and 1H,1H,2H-perfluoro-1-decene (blue) stamped Si(111)-H surfaces with alkanethiol ( $C_nH_{2n+1}SH$ ) treated plasmonic stamps. Monolayer of ethanethiol, 1-butanethiol, 1-hexanethiol, 1-dodecanethiol and 1-hexadecanethiol was attached to the Au surface in the plasmonic stamp prior to the stamping,  $n = 0$  indicates control experiments without thiol treatment.

Keeping all other experimental parameters constant, the effect of distance was investigated *via* functionalization of the flat surface of the exposed gold hemispheroids with 1-alkanethiols, as outlined in Figure 4.15a. The molecular length of the alkane thiols varied from 0.3 ~ 2.5 nm, and the results are summarized in Figure 4.15b and Table 4.2. The water contact angles of the stamped Si(111)-H surfaces with 1-dodecene decrease with increasing length of the 1-alkanethiol, which suggests that increasing the distance between the gold hemispheroids and the silicon surfaces was not productive in terms of yield of hydrosilylation. Similar trend of contact angle measurements was also observed on 1H,1H,2H-perfluoro-1-decene stamped Si(111)-H surface under the same conditions.

**Table 4.2.** Contact angle measurements of hydride-terminated silicon substrates stamped with thiol-modified plasmonic stamps. (Corresponding to Figure 4.17) \* Average of at least 16 measurements

Thiols	Number of carbons	Molecule length	Contact angles*/Degree (1-dodecene)	Contact angles*/Degree (1H,1H,2H-perfluoro-1-decene)
No thiols(Control)	0	0	95.6 ± 1.2	103.5 ± 1.6
Ethanethiol	2	~0.3 nm	90.5 ± 1.8	98.6 ± 1.4
1-Butanethiol	4	~0.6 nm	85.6 ± 1.5	98.3 ± 1.6
1-Hexanethiol	6	~1.0 nm	83.5 ± 1.2	86.5 ± 2.1
1-Dodecanethiol	12	~2.0 nm	82.8 ± 1.6	80.6 ± 1.3
1-Hexadecanethiol	16	~2.5 nm	81.6 ± 0.9	81.6 ± 1.5

#### 4.3.8 Doping Effects of Silicon Substrates

The plasmonic stamp-mediated hydrosilylation appears to be driven by proximal surface plasmons inducing an increase in concentration of electron-hole pairs, as it has been shown that the rate of electron-hole pair generation in a semiconductor is proportional to the local intensity of the electric field,<sup>289, 299</sup> with the electric field enhancement is on the order of  $\sim 10^3$  at the edges of the nanoparticle.<sup>120, 126</sup> In order to substantiate this proposed mechanism, a series of silicon surfaces with differing concentrations of dopants was investigated. Figure 4.16 show the water contact angle measurements of hydride silicon surfaces. As summarized in Figure 4.16a, the contact angles of the hydride-terminated silicon surfaces following hydrosilylation with both 1-dodecene and 1H,1H,2H-perfluoro-1-decene showed strong dependence upon doping. Degenerately doped n- and p-type silicon (n<sup>++</sup> and p<sup>++</sup>) showed only a small increase in water contact angle with both alkenes, to about 85-90 degrees, from 83.1 degree for freshly etched Si(111)-H.

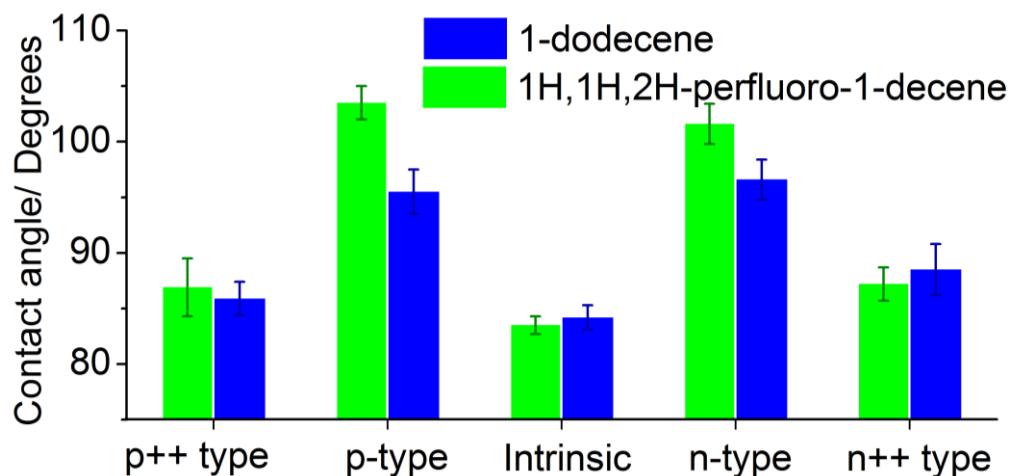


**Figure 4.16.** Water contact angle measurements of 1-alkene stamped silicon surfaces with different doping levels (++: highly doped).

Figure 4.17 showed the corresponding AFM height images of hydride silicon surfaces after stamping with silicon wafers under the same conditions (60 min of plasmonic stamping, illumination of 50 mW/cm<sup>2</sup>). The degenerately doped silicon surface after surface hydrosilylation showed only a faint pattern. Intrinsic (undoped) silicon also showed no significant increase of water contact angle for both alkenes, and no pattern was visible by AFM, with only the terraces of the Si(111)-H to serve as a reference. With lightly doped n- and p-type silicon, on the other hand, the water contact angles increased from 83 degree for freshly etched Si(111)-H to over 100 degrees with 1H,1H,2H-perfluoro-1-decene, and over 95 degree for 1-dodecene. The corresponding AFM micrographs of the stamped Si(111)-H surfaces on lightly doped n- and p-type silicon show obvious patterns.

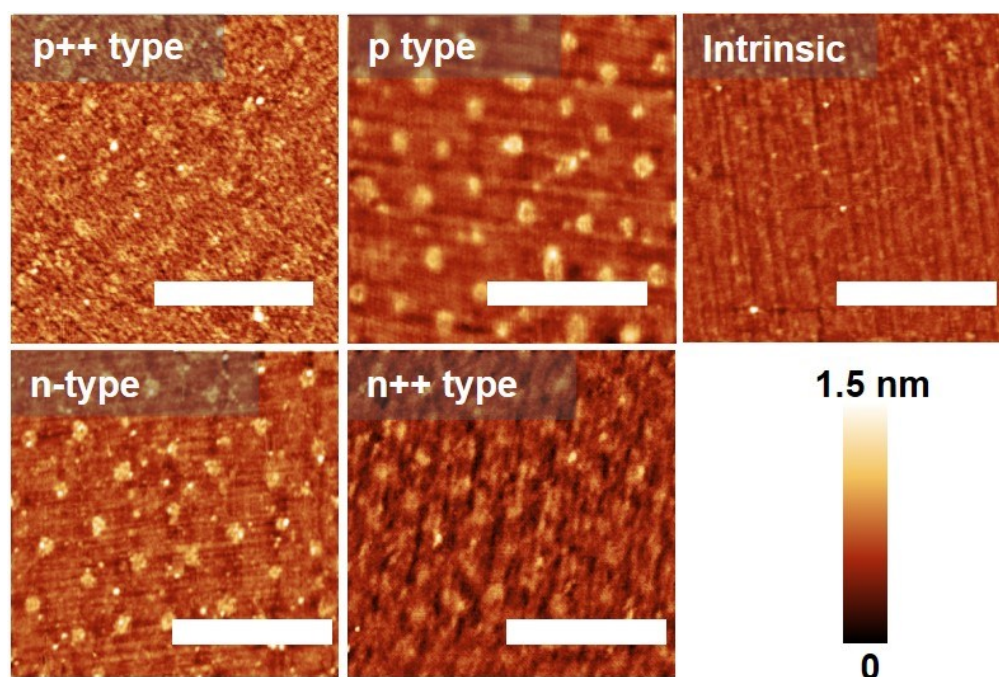


**Figure 4.17.** AFM height micrographs of 1H,1H,2H-perfluoro-1-decene stamped silicon surfaces with various doping concentrations.

Given that the doping density of the Si substrate significantly changes the kinetics of the plasmon-induced hydrosilylation reaction, we explore the possible interactions between free charge carriers near the Si surface (as a result of doping) and the plasmonic field. Specifically, if a free charge carrier (either electron or hole) is within the vicinity of a plasmonic electric field, to a first order approximation, it will acquire kinetic energy proportional to the square of the electric field strength,  $|E|^2$ . If the electric field accelerating these free charge carriers is sufficiently large, electron-hole pair generation can occur through the process of impact ionization, as indicated in Figure 4.18.<sup>300, 301</sup> Specifically, it has been found that there are appreciable rates of impact ionization in silicon at field strengths greater than  $10^5$

V/cm.<sup>302</sup> When considering the spatial distribution of the electric field of the Au nanoparticle plasmon, it is important to account for the image charge effect, where the field of the plasmon will be mirrored about the substrate plane, reduced by a factor of  $\eta=(\epsilon_s-\epsilon_b)/(\epsilon_s+\epsilon_b)$ ,<sup>303</sup> where  $\epsilon_s$  is the dielectric constant of the substrate and  $\epsilon_b$  is the dielectric constant of the surrounding media of the nanoparticle. Given the relatively large dielectric constant of silicon (~16 in the visible spectrum), it is expected to have a strong image charge effect. If we assume that the field of the plasmons for the nanoparticle from Figure 4.17 are confined to a volume  $V_p$  and has an energy of  $E_p$ , the average field strength can be estimated as

$$|\overline{\mathbf{E}}| = \sqrt{\frac{2\eta^2 E_p}{\epsilon_0 V_p}}$$

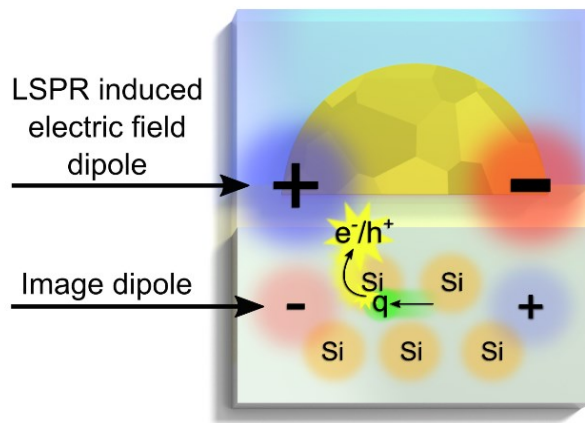


**Figure 4.18.** Schematic mechanism of plasmonic hole generation in silicon *via* free charge carrier impact ionization.

From UV-vis measurements and ellipsometry shown in Figure 4.19, we can estimate  $E_p \approx 2.2$  eV and based on a hemispheroid diameter of  $\sim 30$  nm, we can conservatively estimate that the plasmon field is confined to a volume of  $50 \times 50 \times 50$  nm<sup>3</sup>, giving an average plasmonic field value of  $|\overline{\mathbf{E}}| = 2.2 \times 10^5$  V/cm. Therefore, if there is a free charge carrier within the vicinity of the plasmon image charge, we can expect electron-hole pair generation *via* impact ionization to occur with a reasonable probability, given that appreciable rates of impact ionization in silicon can occur at field strengths greater than  $10^5$  V/cm.<sup>302</sup> Given the proximity of the holes generated by impact ionization, they could subsequently be consumed for the hydrosilylation reaction. To this end, we can calculate the number of free charge carriers within the interaction volume of a plasmon image charge,  $G_i$ , which is simply given by  $G_i = NV_p$ , where  $N$  is the doping density of the Si substrate. If we assume an interaction volume of  $50 \times 50 \times 50$  nm<sup>3</sup> as previously, for intrinsic silicon ( $N = 10^{10}$  cm<sup>-3</sup>), this gives  $G_i = 1.25 \times 10^{-6}$ . Physically, this value is interpreted as there being one free charge carrier for every 80,000 Au nanoparticles at the surface. As such, we would not expect hydrosilylation to occur as a result of plasmon driven impact ionization in intrinsic silicon. Conversely, if we apply this calculation to the lightly doped n-type silicon used in this work ( $N \approx 5.0 \times 10^{15}$  cm<sup>-3</sup>), we get  $G_i = 0.6$ . This is in stark contrast to the intrinsic silicon where this is on the order of 1 free charge carrier per Au nanoparticle. As such, it is reasonable to expect a significant number of holes to be generated *via* impact ionization at these

doping densities, which could be used for the hydrosilylation reaction. Finally, calculating  $G_i$  for the highly doped n++ silicon ( $N \approx 1.2 \times 10^{19} \text{ cm}^{-3}$ ), we find there are 1,500 free charge carriers per Au nanoparticle. Given the extremely high density dopants we would expect a large number of impact ionization events, however we would also expect very high rates of Auger recombination,<sup>304</sup> which work in opposition to each other and could explain the decreased degree of hydrosilylation for both the n++ and p++ substrates in Figures 4.17 and 4.18.

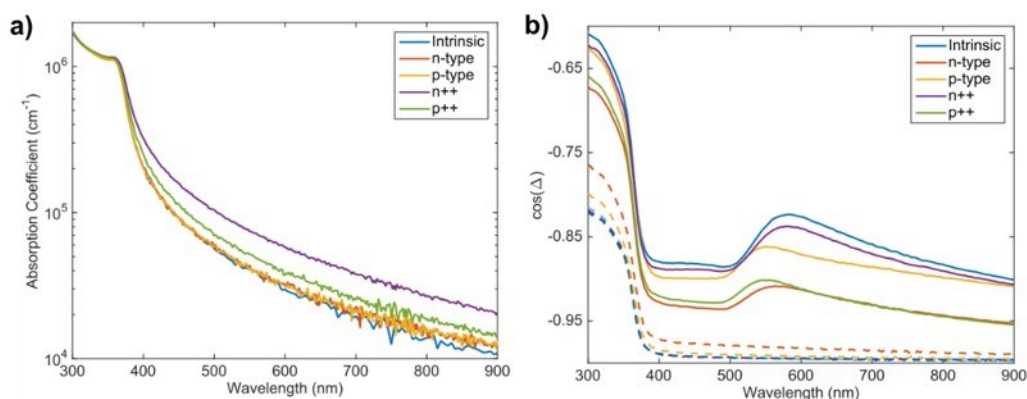


**Figure 4.19.** a) Absorption coefficient of hydrogen terminated (111) oriented silicon with various doping types and densities. b) Cosine of ellipsometric phase shift for pseudo-hexagonal arrays of Au dots on (111) oriented silicon substrates of various doping densities (solid lines), and corresponding bare silicon substrates (dotted lines)

#### 4.4 Conclusions

The enhanced electric field of surface plasmons of gold nanostructures can be used to direct surface chemistry on a semiconductor surface in a localized manner. Gold hemispheroids embedded within a PDMS stamp were used to drive patterned hydrosilylation of an alkene or alkyne on a hydrogen-terminated silicon surface. The plasmonic stamp-assisted hydrosilylation appears to be driven by electron-hole formation near the interface of the silicon, which is followed by an attack of the holes by an alkene or alkyne, leading to silicon-carbon bond formation. The effect of doping, however, suggests that the mechanism is more nuanced. Free charge carrier impact ionization, induced by the electric field of the local plasmons of the gold nanohemispheroids is therefore proposed to explain the role of doping. Other possible energy transfer mechanisms such as hot-carrier injection, plasmonic scattering, and plasmonic heating were also discussed, and were proved to have minor or no contributions to the SPR-assisted surface hydrosilylation.

#### 4.5 Experimental Section

**Materials.** Si wafers (100-oriented, p-type, B-doped,  $\rho = 1-10 \text{ } \Omega\text{-cm}$ , thickness = 500-550  $\mu\text{m}$ ; 111-oriented, prime grade, p-type, B-doped,  $\rho = 1-10 \text{ } \Omega\text{-cm}$ , thickness = 600-650  $\mu\text{m}$ ; 111-oriented, prime grade, intrinsic,  $\rho > 80 \text{ } \Omega\text{-cm}$ , thickness = 500-550  $\mu\text{m}$ ; 111-oriented prime grade, n-type, P-doped,  $\rho = 1-10 \text{ } \Omega\text{-cm}$ , thickness = 600-650  $\mu\text{m}$ ; 111-oriented prime grade, n-type, As-doped,  $\rho = 0.001-0.005 \text{ } \Omega\text{-cm}$ ,

thickness = 500-550  $\mu\text{m}$ ) were purchased from WRS Materials Inc. Millipore water (resistivity: 18.2  $\text{M}\Omega$ ) was used for the preparation of all aqueous solutions. Two types of Block copolymers (BCPs), polystyrene-block-poly-2-vinylpyridine (PS-*b*-P2VP) and polystyrene-block-poly-4-vinylpyridine (PS-*b*-P4VP) with different molecular weights (125k-58.5k and 190k-190k for PS-*b*-P2VP, and 20k-19k for PS-*b*-P4VP), were purchased from Polymer Source Inc. The precursors for the h-PDMS (trimethylsiloxy terminated vinylmethylsiloxane-dimethylsiloxane (VDT-731), 25-35% (methylhydrosiloxane) 65-70% (dimethylsiloxane) (HMS-301), and Pt divinyltetramethyldisiloxane (SIP6831.2) were purchased from Gelest Corp., and 184 PDMS from Dow Corning. 2,4,6,8-tetramethyl-2,4,6,8-tetravinylcyclotetra-siloxane, 30%  $\text{NH}_4\text{OH}$  (aq), 30%  $\text{H}_2\text{O}_2$  (aq),  $\text{KAuCl}_4 \cdot x\text{H}_2\text{O}$  (99.999%), 1,4-butanedithiol (>97%), trichloro(1H,1H,2H,2H-perfluorooctyl)silane (98%), 1,7-octadiene(>99.0%), 1-dodecene (>99.0%), 1H,1H,2H-perfluoro-1-decene (99.0%), 1-dodecyne (99.0%), 4-(Trifluoromethoxy)phenyl acetylene (99.0%), 3,4-dichlorophenylacetylene (99.0%), ethanethiol (97.0%), 1-butanethiol (99.0%), 1-hexanethiol (>98.0%), 1-dodecanethiol (99.0%), and 1-hexadecanethiol (99.0%) were obtained from Sigma-Aldrich, and used as received. 1-dodecene, 1,7-octadiene, 1H,1H,2H-perfluoro-1-decene, and 4-(Trifluoromethoxy)phenyl acetylene were passed through a hot alumina (the alumina was dried at 100  $^\circ\text{C}$  for over 24 h and used while still hot) column to remove water residues and peroxides, and then deoxygenated with a stream of nitrogen gas. Optical filters ( CW526 (centre band

wavelength: 526 nm); FWHM (full width at half max: 180 nm) were purchased from Edmund Inc.

**Fabrication of Plasmonic Stamp and Plasmonic Stamping** was described in the experimental sections in Chapters 2 and 3.

**FDTD Simulation.** Simulations were carried out using a trial version of the commercial software Lumerical FDTD Solutions. The gold nanoparticles were modelled as hemispheroids with a 10 nm radius. Center-to-center spacing of the particles was set to be 70 nm. A non-primitive rectangular unit cell was used for the simulation, and further refined using symmetric and periodic boundary conditions and the x and y directions. In the x-direction, the 70 nm-wide unit cell was broken into 160 mesh units of 0.438 nm, and in the y-direction the 120 nm tall unit cell was broken up into 280 mesh units of 0.429 nm. For the z-direction, the simulation had a span of 2000 nm centered around the gold nanoparticles. The maximum mesh was set to 0.2 nm for a range of 100 nm on each above and below the particles, and the remainder were free to mesh dynamically. The boundary conditions were set as perfectly matched layers at the z extremes. To simulate unpolarized light, two completed simulations were run with x- polarized and y- polarized light. The resultant time averaged electric field from each polarization was then added together, and then divided in half. The apparent four-fold symmetry located at the extremes in the top view of Figure 4.12 results from the discretization of the spheroid into

mesh cells. To confirm this, a simulation was carried out with light polarized at  $\pm 45^\circ$ , the time averaged electric field of each polarization was added together and divided in half.

# 5

## Summary and Outlook

In this thesis, surface plasmon-assisted nanolithography was demonstrated on flat silicon surface using block copolymer template plasmonic stamps, reflecting the distribution of electric field in the Au nanopatterns derived from the self-assembled block-copolymer templates. This approach demonstrates how localized surface plasmons can be used to enable functionalization of technologically relevant surfaces with nanoscale control. Mechanisms have been discussed and it is proposed that the plasmon induced resonant energy transfer drives the localized hydrosilylation on silicon surface. Observed chemical functionalization described here suggests that the form of an electric field of a plasmonic nanostructure can be captured, and imaged, *via* chemical means, on a surface, through hydrosilylation, and potentially, through any chemistry that involves charge carriers on a proximal semiconductor.

## 5.1 Summary of Chapters

### *Chapter 1*

Chapter 1 provided a brief overview of two main related topics, surface nanolithography and nanoplasmonics. For the topic of nanolithography, different types of lithographic approaches has been reviewed with examples, including typical top-down techniques (e.g. photolithography, electron-beam lithography, scanning probe lithography, etc.) and bottom-up techniques. (e.g. molecule self-assembly, nanoparticle self-assembly, etc.) Following the introduction of nanolithographic techniques, the topic of surface plasmons in the metal nanoparticles was briefly introduced and reviewed the progress on the plasmonic applications on photovoltaics, photocatalysis, and photothermal therapy owing to the surface plasmon resonance of noble nanoparticles upon visible light illuminations.

### *Chapter 2*

In Chapter 2, the fabrication of the plasmonic stamp , an optically transparent flexible PDMS stamp carrying gold nanopatterns produced *via* block copolymer self-assembly, was demonstrated with similar fabrication processes as the previous work in our group for catalytic stamp fabrication.<sup>162-164</sup> Ordered gold hemispheroid arrays can be obtained after gold salt metallization and subsequent plasma treatment of solvent annealed block copolymers. By varying the molecular weight of the block

copolymer templates, controllable size and spacings of Au nanopatterns in the plasmonic stamp can be achieved and captured by atomic force microscopy. The obtained gold nanoparticles in the plasmonic stamp have hemispherical shapes, as proven by tilted and cross-section SEM and AFM characterization, facilitating the subsequent stamping process with a flat surface and sharp edges of the patterned Au hemispheroids.

### *Chapter 3*

In Chapter 3, the plasmonic stamps were used to directly functionalize silicon surfaces on a sub-100 nm scale *via* hydrosilylation of 1-alkenes or 1-alkynes, leading to the nanopattern transfer from self-assembled block copolymer templates to the 1-alkyl or 1-alkenyl molecular patterns on flat silicon surfaces. With further surface modification *via* thiol-ene chemistry, these molecular nanopatterns were visualized *via* selective attachment of gold nanoparticles or gold electroless deposition in the thiol-terminated areas. The ring structures reveals the enhanced electric field of the gold hemispheroids in the plasmonic stamp, implying a mechanism involving LSPR assisted hydrosilylation on hydride terminated silicon surface. XPS and water contact angle measurements demonstrate the SPR-assisted surface functionalization *via* hydrosilylation of 1-alkenes and 1-alkynes.

### *Chapter 4*

Multiple mechanisms have been interpreted in the published works regarding energy transfer between metals and semiconductors. In Chapter 4, evidence was provided for doping effects and distance studies from experimental data as well as calculation and simulation, to discuss a number of mechanisms that could be at play in our system. Based on the experimental data and mechanistic discussion, it is proposed that upon illumination with low intensity green light, the strong electric field that induced by the localized surface plasmon resonance of the gold nanoparticles in the plasmonic stamps led to generation of electron-hole pairs near the silicon surface that drive spatially localized hydrosilylation.

## **5.2 Proposed Research Directions**

### **5.2.1 Plasmonic Structure in Photovoltaics**

BCP-templated metal nanopatterns can be applied in photovoltaics to achieve enhanced performance. As is mentioned in the introduction as well as in Chapter 1, solar energy is becoming increasingly significant and attractive because it is renewable and clean. This “green” energy could augment the conventional combustion of fossil fuels.<sup>126</sup> Fabrication of low-cost, high-efficiency solar cells is also the goal of the third generation photovoltaics.<sup>305</sup> In order to enhance the performance of solar cells, one of the important factors is to balance efficient light absorption with charge extraction by the photoactive layer.<sup>306</sup> Increasing film thickness of photovoltaic devices could harvest more light absorption, however, the

charge recombination in this case would be severe due to the low diffusion length of excitons, as well as a resulting increased series resistance. Therefore, the thickness of the photoactive layer is limited.<sup>305, 307</sup>

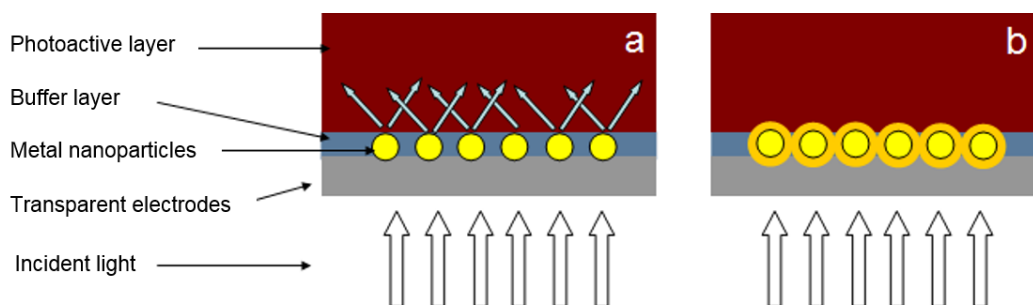


**Figure 5.1.** Schematic representation of Light trapping by: (a) Forward scattering, and (b) Local enhancement of electromagnetic field *via* LSPR

Enhanced photovoltaic performance can be expected by incorporating the pattern into the photovoltaic layer, for example, on the ITO substrate to form ITO/PEDOT:PSS with Au nanoparticles/P3HT:PCBM/LiF/Al structure in the organic solar cell. The enhancement is mainly due to the increase the light absorption by incorporating ordered patterns of plasmonic noble metal nanoparticles into the photoactive layer. As is shown in Figure 5.1, the surface plasmon resonance (SPR) of metal nanoparticles induced by incident light could effectively trap light by forward scattering (Figure 5.1a) and/or by local electromagnetic field enhancement by localized surface plasmon resonance (LSPR) (Figure 5.1b). The metal nanoparticles could be incorporated into the photovoltaic devices by using the self-assembly of block copolymers, which allow great control over the shape and

size of nanopatterns in photovoltaic devices. For example, Figure 5.2 shows that Au nanopatterns were fabricated on the surface of a plain ITO glass substrate *via* BCP self-assembly.

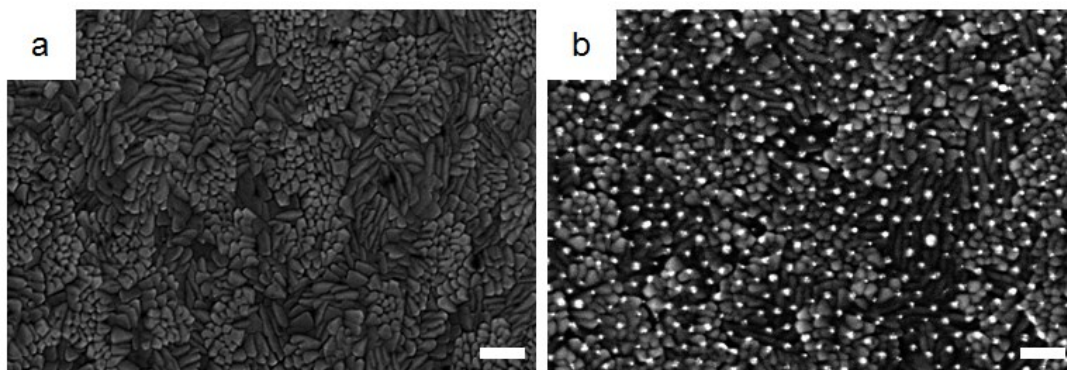


**Figure 5.2.** SEM images of plain ITO (a) and ITO glasses with gold nanopatterns. BCP: PS-*b*-P2VP (20 k-*b*-19 k). Scale bar: 100 nm

The UV-vis absorption and reflection were investigated by placing a thin film of nanopatterns on glass substrates. As shown in Chapter 2, the absorption peak induced by SPR of Au nanoparticles is around 530 nm. After adding a buffer layer of PEDOT:PSS on top, the SPR peak can still be observed and showed in Figure 5.3, indicating the gold nanoparticles can attached firmly on the substrates. The SPR induced absorption around 530 nm well matches with that of the photoactive layer (580 nm for P3HT), suggesting the light absorption enhancement by the SPR effects of gold nanoparticles can be expected in this device architecture.

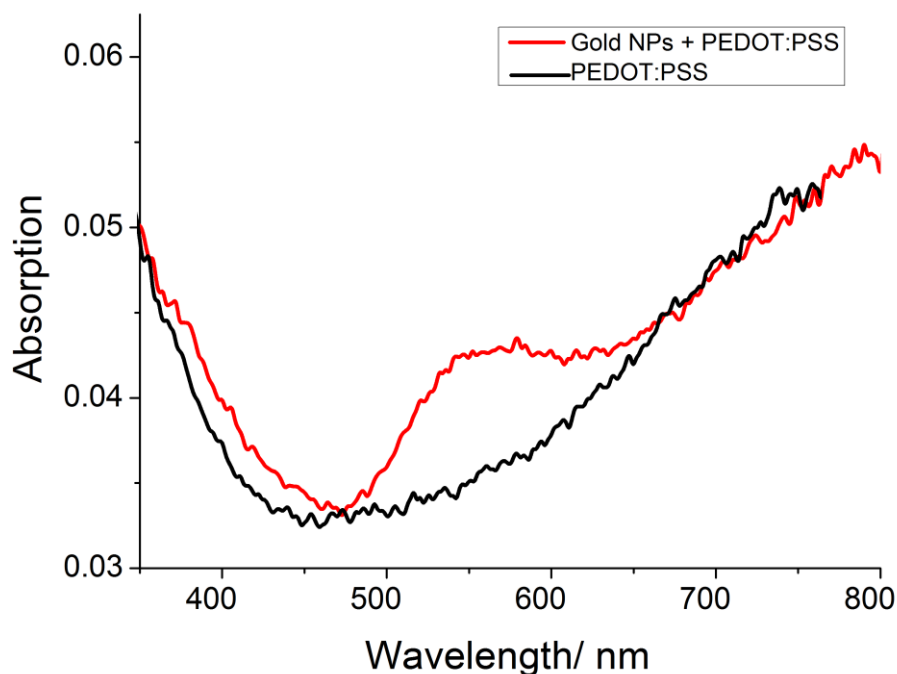


**Figure 5.3.** UV-vis spectroscopy of (a) gold nanoparticles with different sizes on glass substrates, and (b) PEDOT:PSS layer with and without gold nanoparticles.

### 5.2.2 Variation of Sizes of Au Nanopatterns

As previously discussed, the size of plasmonic particles is directly related to the position of their SPR peaks, as well as the scattering/absorption ratio in the extinction spectra.<sup>279</sup> For the plasmonic layer template derived from self-assembled block copolymers, the size of nanoparticles can also be tuned by different strategies. The simplest way is to vary the concentration of metal salts. In Figure 5.4, the size of gold nanoparticles increases from 5 nm to 12 nm by using different metal salt concentration. Higher concentration of metal salt solution could not lead to larger nanoparticles, due to the size limit of PS shell in block copolymers.

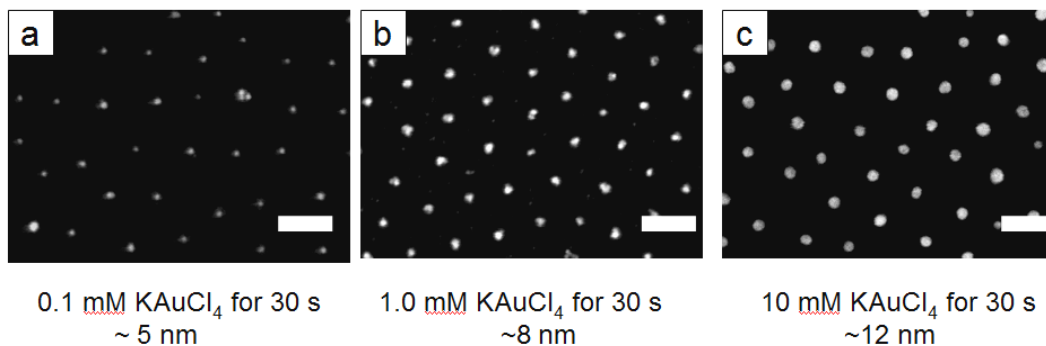


**Figure 5.4.** Enlargement of gold nanoparticles by varying the concentration of metal ions. BCP: PS-*b*-P2VP (20 k-*b*-19 k). Scale bar: 50 nm

For the preparation of larger nanoparticles, a classic seed-mediated growth approach could be applied,<sup>308</sup> and a method that was slightly modified by Spatz group for direct growth in the gold-salt loaded block copolymer films.<sup>198</sup> Specifically, a brief plasma activation step (i.e. less than 10-second plasma treatment) was applied on the as-casted polymer layer with pre-loaded metal salts to partially reduce metal ions while keep the polymer on the substrates, and the resulting nanoparticles are served as seeds. Then the substrates with metal nanopatterns were immersed into an aqueous growth solution containing metal salts and weak reducing agents to allow the seed-mediated growth process. The final size of nanoparticles can be controlled by the concentration of metal salts and reducing agents, as well as the immersing time. The scheme and corresponding SEM images are shown in Figure 5.5. So far,

gold nanoparticles can grow from 5 nm to 30 nm from different growth conditions and remain the same center-to-center spacings.

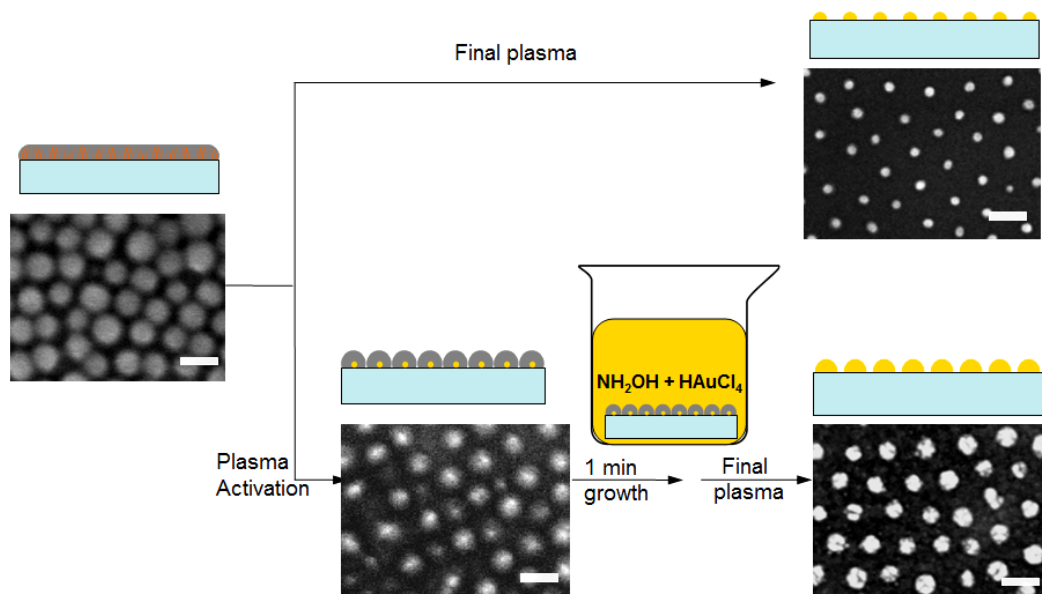


**Figure 5.5.** Schematic illustrations and corresponding SEM images of nanoparticle enlargement process. BCP: PS-*b*-P2VP (20 k-*b*-19 k). Scale bar: 50 nm.

### 5.2.3 Variation of Shapes of Au Nanopatterns

Fabrication of patterned plasmonic nanostructures with unique shapes can extend to plasmonic applications, as well as better understanding the SPR-driven mechanisms.

In terms of plasmonic stamp lithography, the combination of conventional top-down or bottom-up techniques to achieve various plasmonic metal patterns will in principle result in various hydrosilylated patterns on silicon surface. For example, Au triangle patterns can be obtained by using a layer of close-packed polystyrene microspheres as mask for the subsequent gold evaporation into the interstices.<sup>309</sup>

The SEM images of the polystyrene spheres and the corresponding Au triangle patterns are showed in Figure 5.7. Since the hot spots for the Au nanotriangles are distributed at three sharp corners, the hydrosilylated patterns may also take place in these regions under proper light illumination.

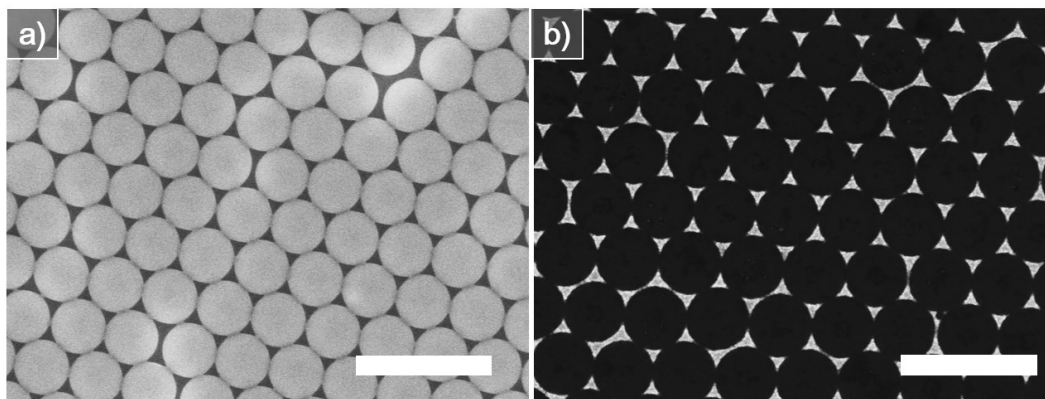


**Figure 5.6.** SEM images of polystyrene spheres ( $D=0.4 \mu\text{m}$ ) and patterned gold nanotriangles ( $a=100 \text{ nm}$ ) after gold evaporation and template removal. Scale bar:  $1 \mu\text{m}$ .

Several factors should be considered for this method. First, the fabrication of plasmonic stamp. Since the gold triangles were evaporated on the silicon surface, the Au tend to form Au@Si composite at the interface, making it harder to be peeled off. An alternative flat surface or surface modification prior to the fabrication should be considered. The second factor is the size of obtained gold nanotriangles. As showed in Figure 5.6b, the size of gold nanotriangles is  $100 \text{ nm}$ , in which the plasmonic scattering will be either dominant or compatible with the SPR absorption. This will add complexity to the driving forces as well as the mechanisms, since it is difficult to distinguish the contributions of scattering and absorption to the

system.<sup>120, 279, 310</sup> Lastly, from the perspective of plasmon induced resonant energy transfer mechanism, the plasmon stamp lithography may not be realized with Au triangles or gold nanorods. As mentioned in Chapter 4, the overlapping of energy levels between SPR of metals and semiconductor is also critical. As the longitudinal SPR absorption for Au nanotriangles and nanorods usually peaked at the wavelength range of 700 ~ 1600 nm, depending on their aspect ratios, their corresponding SPR absorption will have less or no overlaps due to the red shifts of the SPR peaks.<sup>311, 312</sup>

#### **5.2.4 Variation of Orders of Au Nanopatterns**

Nanopatterns from the plasmonic stamp lithography are derived from the block copolymer self-assembly. As discussed in the introduction in Chapters 1 and 2, the formed gold nanopatterns are lack of long-range orders. Therefore, hierarchical plasmonic structures with periodic arrays can be utilized for plasmonic stamping. Schatz and Odom demonstrated superlattice plasmon resonance using hierarchical Au NP arrays that obtained from nanoimprinting lithography.<sup>313</sup> As shown in Figure 5.7, the lattice SPR peak in the transmission spectra can be observed, and is more intense and sharper compared to the nanoparticle SPR peak. They found the coupling of multi-ordered Bragg diffractions and surface plasmon in the Au superlattice led to the enhanced absorption. The charge distribution of the hierarchical Au NP arrays excited by lasers with resonance wavelengths shown in

Figure 5.7c suggested the simulated patterns could be transferred and imaged *via* plasmonic stamp lithography.

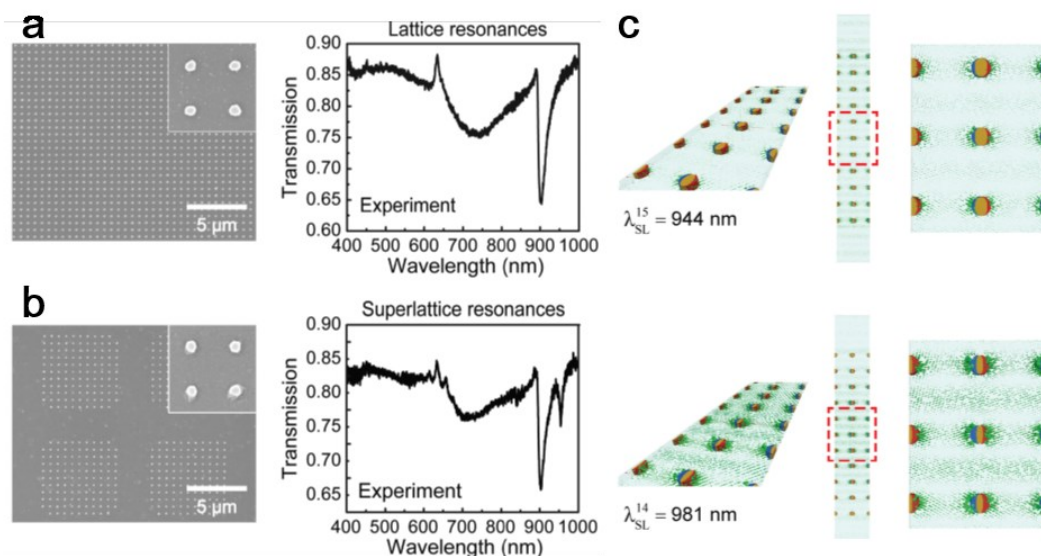


**Figure 5.7.** SEM images and transmission spectra of an infinite (a) and periodic (b) Au nanopatterns. c. FDTD simulations show the charge distributions of the lattice plasmons.

Reprinted with permission from ref. 313 Copyright © 2015 American Chemical Society

#### 5.2.4 Applications to other metals.

Most of the above fabrication routes are also suitable for other metals by changing the corresponding metal-ion solution in the metallization steps, such as silver, copper, platinum, and palladium. Figure 5.8 shows the different types of metal nanopatterns using the same block copolymer. With the various metal or bimetallic nanopatterns for the plasmonic stamp fabrication, application of the stamp lithography can be extended, owing to their controllable SPR peaks. Similar challenges can still exist as the previously discussed gold nanotriangles. The optimized metals should be

carefully selected with consideration of energy level alignment between metals and semiconductors.

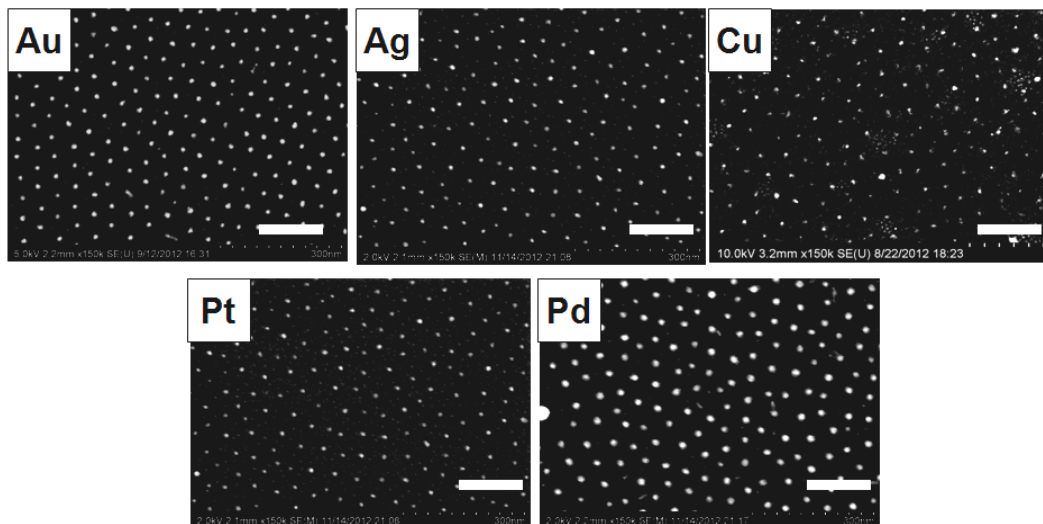


**Figure 5.8.** Ordered nanopatterns with different metals from the block copolymer PS-*b*-P4VP

(20 k-*b*-19 k). Scale bar: 200 nm

## References

1. Hirsch, S. C. *Printing from a Stone: The Story of Lithography*. New York: Viking Press: 1967.
2. Seo, J. H.; Park, J. H.; Kim, S. I.; Park, B. J.; Ma, Z. Q.; Choi, J.; Ju, B. K. Nanopatterning by Laser Interference Lithography: Applications to Optical Devices. *J. Nanosci. Nanotechnol.* **2014**, *14*, 1521-1532.
3. Xu, Y.; Matsumoto, N.; Wu, Q.; Shimatani, Y.; Kawata, H. Site-Specific Nanopatterning of Functional Metallic and Molecular Arbitrary Features in Nanofluidic Channels. *Lab Chip* **2015**, *15*, 1989-1993.
4. Chang, J.-B.; Choi, H. K.; Hannon, A. F.; Alexander-Katz, A.; Ross, C. A.; Berggren, K. K. Design Rules for Self-Assembled Block Copolymer Patterns Using Tiled Templates. *Nat. Commun.* **2014**, *5*, 3305.
5. Nanofabrication of Photonic Devices. <http://www.nanophab.com/nanofabrication>
6. Sabatier, P. A. Top-Down and Bottom-up Approaches to Implementation Research: A Critical Analysis and Suggested Synthesis. *J. Public Pol.* **1986**, *6*, 21-48.
7. Buschman, T. J.; Miller, E. K. Top-Down Versus Bottom-up Control of Attention in the Prefrontal and Posterior Parietal Cortices. *Science* **2007**, *315*, 1860-1862.
8. Mijatovic, D.; Eijkel, J.; Van Den Berg, A. Technologies for Nanofluidic Systems: Top-Down vs. Bottom-up—a Review. *Lab Chip* **2005**, *5*, 492-500.

9. Biswas, A.; Bayer, I. S.; Biris, A. S.; Wang, T.; Dervishi, E.; Faupel, F. Advances in Top–Down and Bottom–up Surface Nanofabrication: Techniques, Applications & Future Prospects. *Adv. Colloid Interface Sci.* **2012**, *170*, 2-27.
10. Gates, B. D.; Xu, Q.; Stewart, M.; Ryan, D.; Willson, C. G.; Whitesides, G. M. New Approaches to Nanofabrication: Molding, Printing, and Other Techniques. *Chem. Rev.* **2005**, *105*, 1171-1196.
11. Silva, G. A. Neuroscience Nanotechnology: Progress, Opportunities and Challenges. *Nat. Rev. Neurosci.* **2006**, *7*, 65-74.
12. Ruiz, R.; Kang, H.; Detcheverry, F. A.; Dobisz, E.; Kercher, D. S.; Albrecht, T. R.; de Pablo, J. J.; Nealey, P. F. Density Multiplication and Improved Lithography by Directed Block Copolymer Assembly. *Science* **2008**, *321*, 936-939.
13. Sundaramurthy, A.; Schuck, P. J.; Conley, N. R.; Fromm, D. P.; Kino, G. S.; Moerner, W. Toward Nanometer-Scale Optical Photolithography: Utilizing the Near-Field of Bowtie Optical Nanoantennas. *Nano Lett.* **2006**, *6*, 355-360.
14. Gather, M. C.; Koehnen, A.; Falcou, A.; Becker, H.; Meerholz, K. Solution-Processed Full-Color Polymer Organic Light-Emitting Diode Displays Fabricated by Direct Photolithography. *Adv. Funct. Mater.* **2007**, *17*, 191-200.
15. Revzin, A.; Russell, R. J.; Yadavalli, V. K.; Koh, W. G.; Deister, C.; Hile, D. D.; Mellott, M. B.; Pishko, M. V. Fabrication of Poly(Ethylene Glycol) Hydrogel Microstructures Using Photolithography. *Langmuir* **2001**, *17*, 5440-5447.
16. Sundaramurthy, A.; Schuck, P. J.; Conley, N. R.; Fromm, D. P.; Kino, G. S.; Moerner,

- W. E. Toward Nanometer-Scale Optical Photolithography: Utilizing the Near-Field of Bowtie Optical Nanoantennas. *Nano Lett.* **2006**, *6*, 355-360.
17. Mooney, J. F.; Hunt, A. J.; McIntosh, J. R.; Liberko, C. A.; Walba, D. M.; Rogers, C. T. Patterning of Functional Antibodies and Other Proteins by Photolithography of Silane Monolayers. *Proc. Natl. Acad. Sci. U. S. A.* **1996**, *93*, 12287-12291.
  18. Qiu, Z.-Y.; Chen, C.; Wang, X.-M.; Lee, I.-S. Advances in the Surface Modification Techniques of Bone-Related Implants for Last 10 Years. *Regen. Biomater.* **2014**, *1*, 67-79.
  19. Eck, W.; Stadler, V.; Geyer, W.; Zharnikov, M.; Golzhauser, A.; Grunze, M. Generation of Surface Amino Groups on Aromatic Self-Assembled Monolayers by Low Energy Electron Beams - A First Step Towards Chemical Lithography. *Adv. Mater.* **2000**, *12*, 805-808.
  20. Fan, M.; Andrade, G. F. S.; Brolo, A. G. A Review on the Fabrication of Substrates for Surface Enhanced Raman Spectroscopy and Their Applications in Analytical Chemistry. *Anal. Chim. Acta* **2011**, *693*, 7-25.
  21. Fujita, J.; Ohnishi, Y.; Ochiai, Y.; Matsui, S. Ultrahigh Resolution of Calixarene Negative Resist in Electron Beam Lithography. *Appl. Phys. Lett.* **1996**, *68*, 1297-1299.
  22. Chang, T. H. P. Proximity Effect in Electron-Beam Lithography. *J. Vac. Sci. Technol.* **1975**, *12*, 1271-1275.
  23. Drouin, D.; Couture, A. R.; Joly, D.; Tastet, X.; Aimez, V.; Gauvin, R. Casino V.

- 2.42 - A Fast and Easy-to-Use Modeling Tool for Scanning Electron Microscopy and Microanalysis Users. *Scanning* **2007**, *29*, 92-101.
24. Ahn, S. H.; Guo, L. J. Large-Area Roll-to-Roll and Roll-to-Plate Nanoimprint Lithography: A Step toward High-Throughput Application of Continuous Nanoimprinting. *ACS Nano* **2009**, *3*, 2304-2310.
25. Aryal, M.; Trivedi, K.; Hu, W. Nano-Confinement Induced Chain Alignment in Ordered P3HT Nanostructures Defined by Nanoimprint Lithography. *ACS Nano* **2009**, *3*, 3085-3090.
26. Ahn, S. H.; Guo, L. J. High-Speed Roll-to-Roll Nanoimprint Lithography on Flexible Plastic Substrates. *Adv. Mater.* **2008**, *20*, 2044-2049.
27. Guo, L. J. Nanoimprint Lithography: Methods and Material Requirements. *Adv. Mater.* **2007**, *19*, 495-513.
28. Austin, M. D.; Ge, H. X.; Wu, W.; Li, M. T.; Yu, Z. N.; Wasserman, D.; Lyon, S. A.; Chou, S. Y. Fabrication of 5 nm Linewidth and 14 nm Pitch Features by Nanoimprint Lithography. *Appl. Phys. Lett.* **2004**, *84*, 5299-5301.
29. Schiff, H. Nanoimprint Lithography: An Old Story in Modern Times? A Review. *J. Vac. Sci. Technol. B* **2008**, *26*, 458-480.
30. Jung, G. Y.; Li, Z. Y.; Wu, W.; Chen, Y.; Olynick, D. L.; Wang, S. Y.; Tong, W. M.; Williams, R. S. Vapor-Phase Self-Assembled Monolayer for Improved Mold Release in Nanoimprint Lithography. *Langmuir* **2005**, *21*, 1158-1161.
31. Jung, G. Y.; Johnston-Halperin, E.; Wu, W.; Yu, Z. N.; Wang, S. Y.; Tong, W. M.; Li,

- Z. Y.; Green, J. E.; Sheriff, B. A.; Boukai, A., *et al.* Circuit Fabrication at 17 nm Half-Pitch by Nanoimprint Lithography. *Nano Lett.* **2006**, *6*, 351-354.
32. Martensson, T.; Carlberg, P.; Borgstrom, M.; Montelius, L.; Seifert, W.; Samuelson, L. Nanowire Arrays Defined by Nanoimprint Lithography. *Nano Lett.* **2004**, *4*, 699-702.
33. Liu, G. Y.; Xu, S.; Qian, Y. L. Nanofabrication of Self-Assembled Monolayers Using Scanning Probe Lithography. *Acc. Chem. Res.* **2000**, *33*, 457-466.
34. Tully, D. C.; Wilder, K.; Frechet, J. M. J.; Trimble, A. R.; Quate, C. F. Dendrimer-Based Self-Assembled Monolayers as Resists for Scanning Probe Lithography. *Adv. Mater.* **1999**, *11*, 314-318.
35. Kramer, S.; Fuierer, R. R.; Gorman, C. B. Scanning Probe Lithography Using Self-Assembled Monolayers. *Chem. Rev.* **2003**, *103*, 4367-4418.
36. Tseng, A. A.; Notargiacomo, A.; Chen, T. P. Nanofabrication by Scanning Probe Microscope Lithography: A Review. *J. Vac. Sci. Technol. B* **2005**, *23*, 877-894.
37. Garno, J. C.; Yang, Y. Y.; Amro, N. A.; Cruchon-Dupeyrat, S.; Chen, S. W.; Liu, G. Y. Precise Positioning of Nanoparticles on Surfaces Using Scanning Probe Lithography. *Nano Lett.* **2003**, *3*, 389-395.
38. Kaholek, M.; Lee, W. K.; LaMattina, B.; Caster, K. C.; Zauscher, S. Fabrication of Stimulus-Responsive Nanopatterned Polymer Brushes by Scanning-Probe Lithography. *Nano Lett.* **2004**, *4*, 373-376.
39. Sun, S. Q.; Leggett, G. J. Generation of Nanostructures by Scanning Near-Field

- Photolithography of Self-Assembled Monolayers and Wet Chemical Etching. *Nano Lett.* **2002**, *2*, 1223-1227.
40. Sun, S.; Leggett, G. J. Matching the Resolution of Electron Beam Lithography by Scanning Near-Field Photolithography. *Nano Lett.* **2004**, *4*, 1381-1384.
41. Rogers, J. A.; Paul, K. E.; Jackman, R. J.; Whitesides, G. M. Using an Elastomeric Phase Mask for Sub-100 nm Photolithography in the Optical Near Field. *Appl. Phys. Lett.* **1997**, *70*, 2658-2660.
42. Scott, T. F.; Kowalski, B. A.; Sullivan, A. C.; Bowman, C. N.; McLeod, R. R. Two-Color Single-Photon Photoinitiation and Photoinhibition for Subdiffraction Photolithography. *Science* **2009**, *324*, 913-917.
43. Lorenz, H.; Despont, M.; Fahrni, N.; Brugger, J.; Vettiger, P.; Renaud, P. High-Aspect-Ratio, Ultrathick, Negative-Tone near-UV Photoresist and Its Applications for Mems. *Sens. Actuators A Physical* **1998**, *64*, 33-39.
44. del Campo, A.; Greiner, C. Su-8: A Photoresist for High-Aspect-Ratio and 3D Submicron Lithography. *J. Micromech. Microeng.* **2007**, *17*, R81-R95.
45. Ito, T.; Okazaki, S. Pushing the Limits of Lithography. *Nature* **2000**, *406*, 1027-1031.
46. Muramatsu, K.; Asakura, H.; Suzuki, K.; Tanizawa, K.; Toyama, M.; Ohtsuka, M.; Yokoyama, N.; Matsumaro, K.; Seki, M.; Koshino, K. Evaluation of the Phase Error in Si-Wire Arrayed-Waveguide Gratings Fabricated by ArF-Immersion Photolithography. *IEICE Electronics Express* **2015**.
47. Switkes, M.; Rothschild, M. Resolution Enhancement of 157 nm Lithography by

- Liquid Immersion. *J. Micro/Nanolithogr., MEMS, MOEMS* **2002**, *1*, 225-228.
48. Päivänranta, B.; Langner, A.; Kirk, E.; David, C.; Ekinici, Y. Sub-10 nm Patterning Using EUV Interference Lithography. *Nanotechnology* **2011**, *22*, 375302.
  49. Grigorescu, A. E.; Hagen, C. W. Resists for Sub-20-nm Electron Beam Lithography with a Focus on HSQ: State of the Art. *Nanotechnology* **2009**, *20*, 292001.
  50. Kim, S.; Marelli, B.; Brenckle, M. A.; Mitropoulos, A. N.; Gil, E.-S.; Tsioris, K.; Tao, H.; Kaplan, D. L.; Omenetto, F. G. All-Water-Based Electron-Beam Lithography Using Silk as a Resist. *Nat. Nanotechnol.* **2014**, *9*, 306-310.
  51. Tseng, A. A.; Chen, K.; Chen, C. D.; Ma, K. J. Electron Beam Lithography in Nanoscale Fabrication: Recent Development. *IEEE Trans. Electron. Packag. Manuf.* **2003**, *26*, 141-149.
  52. Leggett, G. J. Light-Directed Nanosynthesis: Near-Field Optical Approaches to Integration of the Top-Down and Bottom-up Fabrication Paradigms. *Nanoscale* **2012**, *4*, 1840-1855.
  53. Xie, X. N.; Chung, H. J.; Sow, C. H.; Wee, A. T. S. Nanoscale Materials Patterning and Engineering by Atomic Force Microscopy Nanolithography. *Mater. Sci. Eng., R* **2006**, *54*, 1-48.
  54. McConney, M. E.; Singamaneni, S.; Tsukruk, V. V. Probing Soft Matter with the Atomic Force Microscopies: Imaging and Force Spectroscopy. *Polym. Rev.* **2010**, *50*, 235-286.
  55. Schoer, J. K.; Crooks, R. M. Scanning Probe Lithography .4. Characterization of

Scanning Tunneling Microscope-Induced Patterns in n-Alkanethiol Self-Assembled Monolayers. *Langmuir* **1997**, *13*, 2323-2332.

56. Ishibashi, M.; Heike, S.; Kajiyama, H.; Wada, Y.; Hashizume, T. Characteristics of Scanning-Probe Lithography with a Current-Controlled Exposure System. *Appl. Phys. Lett.* **1998**, *72*, 1581-1583.
57. Sugimura, H.; Hanji, T.; Hayashi, K.; Takai, O. Surface Potential Nanopatterning Combining Alkyl and Fluoroalkylsilane Self-Assembled Monolayers Fabricated Via Scanning Probe Lithography. *Adv. Mater.* **2002**, *14*, 524-526.
58. Garcia, R.; Knoll, A. W.; Riedo, E. Advanced Scanning Probe Lithography. *Nat. Nanotechnol.* **2014**, *9*, 577-587.
59. Eigler, D. M.; Schweizer, E. K. Positioning Single Atoms with a Scanning Tunneling Microscope. *Nature* **1990**, *344*, 524-526.
60. Crommie, M. F.; Lutz, C. P.; Eigler, D. M. Confinement of Electrons to Quantum Corrals on a Metal Surface. *Science* **1993**, *262*, 218-220.
61. Hyun, J.; Ahn, S. J.; Lee, W. K.; Chilkoti, A.; Zauscher, S. Molecular Recognition-Mediated Fabrication of Protein Nanostructures by Dip-Pen Lithography. *Nano Lett.* **2002**, *2*, 1203-1207.
62. Son, J. Y.; Shin, Y.-H.; Ryu, S.; Kim, H.; Jang, H. M. Dip-Pen Lithography of Ferroelectric PbTiO<sub>3</sub> Nanodots. *J. Am. Chem. Soc.* **2009**, *131*, 14676-14678.
63. Huang, L.; Braunschweig, A. B.; Shim, W.; Qin, L.; Lim, J. K.; Hurst, S. J.; Huo, F.; Xue, C.; Jong, J.-W.; Mirkin, C. A. Matrix-Assisted Dip-Pen Nanolithography and

Polymer Pen Lithography. *Small* **2010**, *6*, 1077-1081.

64. Shi, J.; Chen, J.; Cremer, P. S. Sub-100 nm Patterning of Supported Bilayers by Nanoshaving Lithography. *J. Am. Chem. Soc.* **2008**, *130*, 2718-2719.
65. Rosa, L. G.; Liang, J. Atomic Force Microscope Nanolithography: Dip-Pen, Nanoshaving, Nanografting, Tapping Mode, Electrochemical and Thermal Nanolithography. *J. Phys.: Condens. Matter* **2009**, *21*, 483001.
66. Jian, S.-R.; Juang, J.-Y. Scanned Probe Oxidation on P-GaAs (100) Surface with an Atomic Force Microscopy. *Nanoscale Res. Lett.* **2008**, *3*, 249-254.
67. Kuramochi, H.; Ando, K.; Shikakura, Y.; Yasutake, M.; Tokizaki, T.; Yokoyama, H. Nano-Oxidation and in Situ Faradaic Current Detection Using Dynamic Carbon Nanotube Probes. *Nanotechnology* **2004**, *15*, 1126.
68. Wu, W.; Tong, W. M.; Bartman, J.; Chen, Y.; Walmsley, R.; Yu, Z.; Xia, Q.; Park, I.; Picciotto, C.; Gao, J. Sub-10 nm Nanoimprint Lithography by Wafer Bowing. *Nano Lett.* **2008**, *8*, 3865-3869.
69. Pisignano, D.; Di Benedetto, F.; Persano, L.; Gigli, G.; Cingolani, R. Rapid Soft Lithography by Bottom-up Enhanced Capillarity. *Langmuir* **2004**, *20*, 4802-4804.
70. Gabai, R.; Ismach, A.; Joselevich, E. Nanofacet Lithography: A New Bottom-up Approach to Nanopatterning and Nanofabrication by Soft Replication of Spontaneously Faceted Crystal Surfaces. *Adv. Mater.* **2007**, *19*, 1325-1330.
71. Haussmann, A.; Milde, P.; Erler, C.; Eng, L. M. Ferroelectric Lithography: Bottom-up Assembly and Electrical Performance of a Single Metallic Nanowire. *Nano Lett.*

2009, 9, 763-768.

72. Trujillo, N. J.; Baxamusa, S. H.; Gleason, K. K. Grafted Functional Polymer Nanostructures Patterned Bottom-up by Colloidal Lithography and Initiated Chemical Vapor Deposition (ICVD). *Chem. Mater.* **2009**, *21*, 742-750.
73. Stang, P. J.; Olenyuk, B. Self-Assembly, Symmetry, and Molecular Architecture: Coordination as the Motif in the Rational Design of Supramolecular Metallacyclic Polygons and Polyhedra. *Acc. Chem. Res.* **1997**, *30*, 502-518.
74. Elemans, J.; Van Hameren, R.; Nolte, R. J. M.; Rowan, A. E. Molecular Materials by Self-Assembly of Porphyrins, Phthalocyanines, and Perylenes. *Adv. Mater.* **2006**, *18*, 1251-1266.
75. Li, D.; Shlyahovsky, B.; Elbaz, J.; Willner, I. Amplified Analysis of Low-Molecular-Weight Substrates or Proteins by the Self-Assembly of Dnazyme-Aptamer Conjugates. *J. Am. Chem. Soc.* **2007**, *129*, 5804-5805.
76. Palmer, L. C.; Stupp, S. I. Molecular Self-Assembly into One-Dimensional Nanostructures. *Acc. Chem. Res.* **2008**, *41*, 1674-1684.
77. Faul, C. F.; Antonietti, M. Ionic Self-Assembly: Facile Synthesis of Supramolecular Materials. *Adv. Mater.* **2003**, *15*, 673-683.
78. Li, S.-L.; Xiao, T.; Lin, C.; Wang, L. Advanced Supramolecular Polymers Constructed by Orthogonal Self-Assembly. *Chem. Soc. Rev.* **2012**, *41*, 5950-5968.
79. Geim, A. K.; Grigorieva, I. V. van der Waals Heterostructures. *Nature* **2013**, *499*, 419-425.

80. Vauthey, S.; Santoso, S.; Gong, H.; Watson, N.; Zhang, S. Molecular Self-Assembly of Surfactant-Like Peptides to Form Nanotubes and Nanovesicles. *PNAS* **2002**, *99*, 5355-5360.
81. Chandler, D. Interfaces and the Driving Force of Hydrophobic Assembly. *Nature* **2005**, *437*, 640-647.
82. Corradi, E.; Meille, S. V.; Messina, M. T.; Mentrangolo, P.; Resnati, G. Halogen Bonding Versus Hydrogen Bonding in Driving Self-Assembly Processes. *Angew. Chem. Int. Ed.* **2000**, *112*, 1852-1856.
83. Paramonov, S. E.; Jun, H.-W.; Hartgerink, J. D. Self-Assembly of Peptide-Amphiphile Nanofibers: The Roles of Hydrogen Bonding and Amphiphilic Packing. *J. Am. Chem. Soc.* **2006**, *128*, 7291-7298.
84. Palermo, V.; Samori, P. Molecular Self-Assembly across Multiple Length Scales. *Angew. Chem. Int. Ed.* **2007**, *46*, 4428-4432.
85. Ulman, A. Formation and Structure of Self-Assembled Monolayers. *Chem. Rev.* **1996**, *96*, 1533-1554.
86. Love, J. C.; Estroff, L. A.; Kriebel, J. K.; Nuzzo, R. G.; Whitesides, G. M. Self-Assembled Monolayers of Thiolates on Metals as a Form of Nanotechnology. *Chem. Rev.* **2005**, *105*, 1103-1169.
87. Love, J. C.; Estroff, L. A.; Kriebel, J. K.; Nuzzo, R. G.; Whitesides, G. M. Self-Assembled Monolayers of Thiolates on Metals as a Form of Nanotechnology. *Chem. Rev.* **2005**, *105*, 1103-1170.

88. Arima, Y.; Iwata, H. Effect of Wettability and Surface Functional Groups on Protein Adsorption and Cell Adhesion Using Well-Defined Mixed Self-Assembled Monolayers. *Biomaterials* **2007**, *28*, 3074-3082.
89. Vericat, C.; Vela, M. E.; Benitez, G.; Carro, P.; Salvarezza, R. C. Self-Assembled Monolayers of Thiols and Dithiols on Gold: New Challenges for a Well-Known System. *Chem. Soc. Rev.* **2010**, *39*, 1805-1834.
90. Toworfe, G.; Composto, R.; Shapiro, I.; Ducheyne, P. Nucleation and Growth of Calcium Phosphate on Amine-, Carboxyl- and Hydroxyl-Silane Self-Assembled Monolayers. *Biomaterials* **2006**, *27*, 631-642.
91. Jordan, R.; Ulman, A.; Kang, J. F.; Rafailovich, M. H.; Sokolov, J. Surface-Initiated Anionic Polymerization of Styrene by Means of Self-Assembled Monolayers. *J. Am. Chem. Soc.* **1999**, *121*, 1016-1022.
92. Senaratne, W.; Andruzzi, L.; Ober, C. K. Self-Assembled Monolayers and Polymer Brushes in Biotechnology: Current Applications and Future Perspectives. *Biomacromolecules* **2005**, *6*, 2427-2448.
93. Tsubery, H.; Mrksich, M. Biochemical Assays of Immobilized Oligonucleotides with Mass Spectrometry. *Langmuir* **2008**, *24*, 5433-5438.
94. Zhang, M.; Xu, S.; Minter, S. D.; Baum, D. A. Investigation of a Deoxyribozyme as a Biofuel Cell Catalyst. *J. Am. Chem. Soc.* **2011**, *133*, 15890-15893.
95. Richard, C.; Balavoine, F.; Schultz, P.; Ebbesen, T. W.; Mioskowski, C. Supramolecular Self-Assembly of Lipid Derivatives on Carbon Nanotubes. *Science*

**2003**, *300*, 775-778.

96. Klok, H. A.; Lecommandoux, S. Supramolecular Materials Via Block Copolymer Self-Assembly. *Adv. Mater.* **2001**, *13*, 1217-1229.
97. He, Y.; Ye, T.; Su, M.; Zhang, C.; Ribbe, A. E.; Jiang, W.; Mao, C. Hierarchical Self-Assembly of DNA into Symmetric Supramolecular Polyhedra. *Nature* **2008**, *452*, 198-201.
98. Huang, F.; O'Reilly, R.; Zimmerman, S. C. Polymer Self-Assembly: A Web Themed Issue. *Chem. Commun.* **2014**, *50*, 13415-13416.
99. Park, S.; Lim, J.-H.; Chung, S.-W.; Mirkin, C. A. Self-Assembly of Mesoscopic Metal-Polymer Amphiphiles. *Science* **2004**, *303*, 348-351.
100. Hartgerink, J. D.; Beniash, E.; Stupp, S. I. Self-Assembly and Mineralization of Peptide-Amphiphile Nanofibers. *Science* **2001**, *294*, 1684-1688.
101. Liu, Y.; Yu, C.; Jin, H.; Jiang, B.; Zhu, X.; Zhou, Y.; Lu, Z.; Yan, D. A Supramolecular Janus Hyperbranched Polymer and Its Photoresponsive Self-Assembly of Vesicles with Narrow Size Distribution. *J. Am. Chem. Soc.* **2013**, *135*, 4765-4770.
102. Lin, Y.; Boker, A.; He, J. B.; Sill, K.; Xiang, H. Q.; Abetz, C.; Li, X. F.; Wang, J.; Emrick, T.; Long, S., *et al.* Self-Directed Self-Assembly of Nanoparticle/Copolymer Mixtures. *Nature* **2005**, *434*, 55-59.
103. Darling, S. B. Directing the Self-Assembly of Block Copolymers. *Prog. Polym. Sci.* **2007**, *32*, 1152-1204.

104. Grzelczak, M.; Vermant, J.; Furst, E. M.; Liz-Marzan, L. M. Directed Self-Assembly of Nanoparticles. *ACS Nano* **2010**, *4*, 3591-3605.
105. Chen, Q.; Bae, S. C.; Granick, S. Directed Self-Assembly of a Colloidal Kagome Lattice. *Nature* **2011**, *469*, 381-384.
106. Jeong, S.-J.; Kim, J. Y.; Kim, B. H.; Moon, H.-S.; Kim, S. O. Directed Self-Assembly of Block Copolymers for Next Generation Nanolithography. *Mater. Today* **2013**, *16*, 468-476.
107. Rosler, A.; Vandermeulen, G. W. M.; Klok, H. A. Advanced Drug Delivery Devices Via Self-Assembly of Amphiphilic Block Copolymers. *Adv. Drug Delivery Rev.* **2001**, *53*, 95-108.
108. Mai, Y.; Eisenberg, A. Self-Assembly of Block Copolymers. *Chem. Soc. Rev.* **2012**, *41*, 5969-5985.
109. Chai, J.; Wang, D.; Fan, X.; Buriak, J. M. Assembly of Aligned Linear Metallic Patterns on Silicon. *Nat. Nanotechnol.* **2007**, *2*, 500-506.
110. KG, A. T.; Gotrik, K.; Hannon, A.; Alexander-Katz, A.; Ross, C.; Berggren, K. Templating Three-Dimensional Self-Assembled Structures in Bilayer Block Copolymer Films. *Science* **2012**, *336*, 1294-1298.
111. Dong, A.; Ye, X.; Chen, J.; Murray, C. B. Two-Dimensional Binary and Ternary Nanocrystal Superlattices: The Case of Monolayers and Bilayers. *Nano Lett.* **2011**, *11*, 1804-1809.
112. Dong, A.; Chen, J.; Vora, P. M.; Kikkawa, J. M.; Murray, C. B. Binary Nanocrystal

- Superlattice Membranes Self-Assembled at the Liquid-Air Interface. *Nature* **2010**, *466*, 474-477.
113. Chen, J.; Ye, X.; Murray, C. B. Systematic Electron Crystallographic Studies of Self-Assembled Binary Nanocrystal Superlattices. *ACS Nano* **2010**, *4*, 2374-2381.
114. Mulvaney, P. Surface Plasmon Spectroscopy of Nanosized Metal Particles. *Langmuir* **1996**, *12*, 788-800.
115. Hutter, E.; Fendler, J. H. Exploitation of Localized Surface Plasmon Resonance. *Adv. Mater.* **2004**, *16*, 1685-1706.
116. Ghosh, S. K.; Pal, T. Interparticle Coupling Effect on the Surface Plasmon Resonance of Gold Nanoparticles: From Theory to Applications. *Chem. Rev.* **2007**, *107*, 4797-4862.
117. Pillai, S.; Catchpole, K. R.; Trupke, T.; Green, M. A. Surface Plasmon Enhanced Silicon Solar Cells. *J. Appl. Phys.* **2007**, *101*, 093105.
118. Homola, J. Surface Plasmon Resonance Sensors for Detection of Chemical and Biological Species. *Chem. Rev.* **2008**, *108*, 462-493.
119. Mayer, K. M.; Hafner, J. H. Localized Surface Plasmon Resonance Sensors. *Chem. Rev.* **2011**, *111*, 3828-3857.
120. Linic, S.; Christopher, P.; Ingram, D. B. Plasmonic-Metal Nanostructures for Efficient Conversion of Solar to Chemical Energy. *Nat. Mater.* **2011**, *10*, 911-921.
121. Wang, H.; Brandl, D. W.; Le, F.; Nordlander, P.; Halas, N. J. Nanorice: A Hybrid Plasmonic Nanostructure. *Nano Lett.* **2006**, *6*, 827-832.

122. Halas, N. J.; Lal, S.; Chang, W.-S.; Link, S.; Nordlander, P. Plasmons in Strongly Coupled Metallic Nanostructures. *Chem. Rev.* **2011**, *111*, 3913-3961.
123. Knight, M. W.; Sobhani, H.; Nordlander, P.; Halas, N. J. Photodetection with Active Optical Antennas. *Science* **2011**, *332*, 702-704.
124. Mukherjee, S.; Libisch, F.; Large, N.; Neumann, O.; Brown, L. V.; Cheng, J.; Lassiter, J. B.; Carter, E. A.; Nordlander, P.; Halas, N. J. Hot Electrons Do the Impossible: Plasmon-Induced Dissociation of H<sub>2</sub> on Au. *Nano Lett.* **2013**, *13*, 240-247.
125. Brongersma, M. L.; Halas, N. J.; Nordlander, P. Plasmon-Induced Hot Carrier Science and Technology. *Nat. Nanotechnol.* **2015**, *10*, 25-34.
126. Atwater, H. A.; Polman, A. Plasmonics for Improved Photovoltaic Devices. *Nat. Mater.* **2010**, *9*, 205-213.
127. Huang, X. H.; El-Sayed, I. H.; Qian, W.; El-Sayed, M. A. Cancer Cell Imaging and Photothermal Therapy in the near-Infrared Region by Using Gold Nanorods. *J. Am. Chem. Soc.* **2006**, *128*, 2115-2120.
128. Huang, X.; Jain, P. K.; El-Sayed, I. H.; El-Sayed, M. A. Gold Nanoparticles: Interesting Optical Properties and Recent Applications in Cancer Diagnostic and Therapy. *Nanomedicine* **2007**, *2*, 681-693.
129. Jain, P. K.; El-Sayed, I. H.; El-Sayed, M. A. Au Nanoparticles Target Cancer. *Nano Today* **2007**, *2*, 18-29.
130. Jain, P. K.; Huang, X.; El-Sayed, I. H.; El-Sayad, M. A. Review of Some Interesting

Surface Plasmon Resonance-Enhanced Properties of Noble Metal Nanoparticles and Their Applications to Biosystems. *Plasmonics* **2007**, *2*, 107-118.

131. Dickerson, E. B.; Dreaden, E. C.; Huang, X.; El-Sayed, I. H.; Chu, H.; Pushpanketh, S.; McDonald, J. F.; El-Sayed, M. A. Gold Nanorod Assisted near-Infrared Plasmonic Photothermal Therapy (PPTT) of Squamous Cell Carcinoma in Mice. *Cancer Letters* **2008**, *269*, 57-66.
132. Huang, X.; Jain, P. K.; El-Sayed, I. H.; El-Sayed, M. A. Plasmonic Photothermal Therapy (PPTT) Using Gold Nanoparticles. *Lasers Med Sci* **2008**, *23*, 217-228.
133. Jain, P. K.; Huang, X.; El-Sayed, I. H.; El-Sayed, M. A. Noble Metals on the Nanoscale: Optical and Photothermal Properties and Some Applications in Imaging, Sensing, Biology, and Medicine. *Acc. Chem. Res.* **2008**, *41*, 1578-1586.
134. Boisselier, E.; Astruc, D. Gold Nanoparticles in Nanomedicine: Preparations, Imaging, Diagnostics, Therapies and Toxicity. *Chem. Soc. Rev.* **2009**, *38*, 1759-1782.
135. Nakayama, K.; Tanabe, K.; Atwater, H. A. Plasmonic Nanoparticle Enhanced Light Absorption in Gaas Solar Cells. *Appl. Phys. Lett.* **2008**, *93*, 121904.
136. Pala, R. A.; White, J.; Barnard, E.; Liu, J.; Brongersma, M. L. Design of Plasmonic Thin-Film Solar Cells with Broadband Absorption Enhancements. *Adv. Mater.* **2009**, *21*, 3504-3509.
137. Aydin, K.; Ferry, V. E.; Briggs, R. M.; Atwater, H. A. Broadband Polarization-Independent Resonant Light Absorption Using Ultrathin Plasmonic Super Absorbers. *Nat. Commun.* **2011**, *2*, 517.

138. Baek, S.-W.; Park, G.; Noh, J.; Cho, C.; Lee, C.-H.; Seo, M.-K.; Song, H.; Lee, J.-Y. Au@Ag Core–Shell Nanocubes for Efficient Plasmonic Light Scattering Effect in Low Bandgap Organic Solar Cells. *ACS Nano* **2014**, *8*, 3302-3312.
139. Thomann, I.; Pinaud, B. A.; Chen, Z.; Clemens, B. M.; Jaramillo, T. F.; Brongersma, M. L. Plasmon Enhanced Solar-to-Fuel Energy Conversion. *Nano Lett.* **2011**, *11*, 3440-3446.
140. Liu, Z.; Hou, W.; Pavaskar, P.; Aykol, M.; Cronin, S. B. Plasmon Resonant Enhancement of Photocatalytic Water Splitting under Visible Illumination. *Nano Lett.* **2011**, *11*, 1111-1116.
141. Tian, Y.; Tatsuma, T. Mechanisms and Applications of Plasmon-Induced Charge Separation at TiO<sub>2</sub> Films Loaded with Gold Nanoparticles. *J. Am. Chem. Soc.* **2005**, *127*, 7632-7637.
142. Hou, W.; Hung, W. H.; Pavaskar, P.; Goepfert, A.; Aykol, M.; Cronin, S. B. Photocatalytic Conversion of CO<sub>2</sub> to Hydrocarbon Fuels Via Plasmon-Enhanced Absorption and Metallic Interband Transitions. *ACS Catalysis* **2011**, *1*, 929-936.
143. Roy, S. C.; Varghese, O. K.; Paulose, M.; Grimes, C. A. Toward Solar Fuels: Photocatalytic Conversion of Carbon Dioxide to Hydrocarbons. *ACS Nano* **2010**, *4*, 1259-1278.
144. Tu, W.; Zhou, Y.; Zou, Z. Photocatalytic Conversion of CO<sub>2</sub> into Renewable Hydrocarbon Fuels: State-of-the-Art Accomplishment, Challenges, and Prospects. *Adv. Mater.* **2014**, *26*, 4607-4626.

145. An, C.; Wang, J.; Jiang, W.; Zhang, M.; Ming, X.; Wang, S.; Zhang, Q. Strongly Visible-Light Responsive Plasmonic Shaped AgX:Ag (X = Cl, Br) Nanoparticles for Reduction of CO<sub>2</sub> to Methanol. *Nanoscale* **2012**, *4*, 5646-5650.
146. Liu, E.; Kang, L.; Wu, F.; Sun, T.; Hu, X.; Yang, Y.; Liu, H.; Fan, J. Photocatalytic Reduction of CO<sub>2</sub> into Methanol over Ag/TiO<sub>2</sub> Nanocomposites Enhanced by Surface Plasmon Resonance. *Plasmonics* **2014**, *9*, 61-70.
147. Liu, E.; Qi, L.; Bian, J.; Chen, Y.; Hu, X.; Fan, J.; Liu, H.; Zhu, C.; Wang, Q. A Facile Strategy to Fabricate Plasmonic Cu Modified TiO<sub>2</sub> Nano-Flower Films for Photocatalytic Reduction of CO<sub>2</sub> to Methanol. *Mater. Res. Bull.* **2015**, *68*, 203-209.
148. Cole, E. B.; Lakkaraju, P. S.; Rampulla, D. M.; Morris, A. J.; Abelev, E.; Bocarsly, A. B. Using a One-Electron Shuttle for the Multielectron Reduction of CO<sub>2</sub> to Methanol: Kinetic, Mechanistic, and Structural Insights. *J. Am. Chem. Soc.* **2010**, *132*, 11539-11551.
149. von Maltzahn, G.; Park, J.-H.; Agrawal, A.; Bandaru, N. K.; Das, S. K.; Sailor, M. J.; Bhatia, S. N. Computationally Guided Photothermal Tumor Therapy Using Long-Circulating Gold Nanorod Antennas. *Cancer Res.* **2009**, *69*, 3892-3900.
150. Hessel, C. M.; Pattani, V. P.; Rasch, M.; Panthani, M. G.; Koo, B.; Tunnell, J. W.; Korgel, B. A. Copper Selenide Nanocrystals for Photothermal Therapy. *Nano Lett.* **2011**, *11*, 2560-2566.
151. Huschka, R.; Barhoumi, A.; Liu, Q.; Roth, J. A.; Ji, L.; Halas, N. J. Gene Silencing by Gold Nanoshell-Mediated Delivery and Laser-Triggered Release of Antisense

- Oligonucleotide and Sirna. *ACS Nano* **2012**, *6*, 7681-7691.
152. Chen, Z.; Wang, Q.; Wang, H.; Zhang, L.; Song, G.; Song, L.; Hu, J.; Wang, H.; Liu, J.; Zhu, M., *et al.* Ultrathin Pegylated W<sub>18</sub>O<sub>49</sub> Nanowires as a New 980 nm-Laser-Driven Photothermal Agent for Efficient Ablation of Cancer Cells *in vivo*. *Adv. Mater.* **2013**, *25*, 2095-2100.
153. Zedan, A. F.; Moussa, S.; Turner, J.; Atkinson, G.; El-Shall, M. S. Ultrasmall Gold Nanoparticles Anchored to Graphene and Enhanced Photothermal Effects by Laser Irradiation of Gold Nanostructures in Graphene Oxide Solutions. *ACS Nano* **2013**, *7*, 627-636.
154. Fang, Z.; Zhen, Y.-R.; Neumann, O.; Polman, A.; Javier Garcia de Abajo, F.; Nordlander, P.; Halas, N. J. Evolution of Light-Induced Vapor Generation at a Liquid-Immersed Metallic Nanoparticle. *Nano Lett.* **2013**, *13*, 1736-1742.
155. Huang, P.; Lin, J.; Li, W.; Rong, P.; Wang, Z.; Wang, S.; Wang, X.; Sun, X.; Aronova, M.; Niu, G. Biodegradable Gold Nanovesicles with an Ultrastrong Plasmonic Coupling Effect for Photoacoustic Imaging and Photothermal Therapy. *Angew. Chem.* **2013**, *125*, 14208-14214.
156. Liu, F.; Lubber, E. J.; Huck, L. A.; Olsen, B. C.; Buriak, J. M. Nanoscale Plasmonic Stamp Lithography on Silicon. *ACS Nano* **2015**, *9*, 2184-2193.
157. Jin, C.; Olsen, B. C.; Wu, N. L. Y.; Lubber, E. J.; Buriak, J. M. Sequential Nanopatterned Block Copolymer Self-Assembly on Surfaces. *Langmuir* **2016**, *32*, 5890-5898.

158. Wu, N. L. Y.; Harris, K. D.; Buriak, J. M. Conversion of Bilayers of PS-*b*-PDMS Block Copolymer into Closely Packed, Aligned Silica Nanopatterns. *ACS Nano* **2013**, *7*, 5595-5606.
159. Wu, N. L. Y.; Zhang, X.; Murphy, J. N.; Chai, J.; Harris, K. D.; Buriak, J. M. Density Doubling of Block Copolymer Templated Features. *Nano Lett.* **2012**, *12*, 264-268.
160. Zhang, X.; Harris, K. D.; Wu, N. L. Y.; Murphy, J. N.; Buriak, J. M. Fast Assembly of Ordered Block Copolymer Nanostructures through Microwave Annealing. *ACS Nano* **2010**, *4*, 7021-7029.
161. Sayed, S. Y.; Buriak, J. M. Epitaxial Growth of Nanostructured Gold Films on Germanium *via* Galvanic Displacement. *ACS Appl. Mater. Interfaces* **2010**, *2*, 3515-3524.
162. Mizuno, H.; Buriak, J. M. Building Upon Patterned Organic Mono Layers Produced *via* Catalytic Stamp Lithography. *ACS Appl. Mater. Interfaces* **2010**, *2*, 2301-2307.
163. Mizuno, H.; Buriak, J. M. Nanoscale Patterning of Organic Monolayers by Catalytic Stamp Lithography: Scope and Limitations. *ACS Appl. Mater. Interfaces* **2009**, *1*, 2711-2720.
164. Mizuno, H.; Buriak, J. M. Catalytic Stamp Lithography for Sub-100 nm Patterning of Organic Monolayers. *J. Am. Chem. Soc.* **2008**, *130*, 17656-17657.
165. Chai, J.; Buriak, J. M. Using Cylindrical Domains of Block Copolymers to Self-Assemble and Align Metallic Nanowires. *ACS Nano* **2008**, *2*, 489-501.
166. Aizawa, M.; Buriak, J. M. Block Copolymer Templated Chemistry for the

- Formation of Metallic Nanoparticle Arrays on Semiconductor Surfaces. *Chem. Mater.* **2007**, *19*, 5090-5101.
167. Zhang, X.; Qiao, Y.; Xu, L.; Buriak, J. M. Constructing Metal-Based Structures on Nanopatterned Etched Silicon. *ACS Nano* **2011**, *5*, 5015-5024.
168. Cui, H.; Chen, Z.; Zhong, S.; Wooley, K. L.; Pochan, D. J. Block Copolymer Assembly via Kinetic Control. *Science* **2007**, *317*, 647-650.
169. Fasolka, M. J.; Mayes, A. M. Block Copolymer Thin Films: Physics and Applications. *Annu. Rev. Mater. Res.* **2001**, *31*, 323-355.
170. Park, M.; Harrison, C.; Chaikin, P. M.; Register, R. A.; Adamson, D. H. Block Copolymer Lithography: Periodic Arrays of Similar to 10(11) Holes in 1 Square Centimeter. *Science* **1997**, *276*, 1401-1404.
171. Bates, F. S.; Fredrickson, G. Block Copolymers-Designer Soft Materials. *Phys. Today* **1999**, *52*, 32-38.
172. Jain, S.; Bates, F. S. On the Origins of Morphological Complexity in Block Copolymer Surfactants. *Science* **2003**, *300*, 460-464.
173. Chen, J.; Thomas, E.; Ober, C.; Mao, G. Self-Assembled Smectic Phases in Rod-Coil Block Copolymers. *Science* **1996**, *273*, 343-346.
174. Kim, S. H.; Misner, M. J.; Xu, T.; Kimura, M.; Russell, T. P. Highly Oriented and Ordered Arrays from Block Copolymers via Solvent Evaporation. *Adv. Mater.* **2004**, *16*, 226-231.
175. Cheng, J. Y.; Mayes, A. M.; Ross, C. A. Nanostructure Engineering by Templated

- Self-Assembly of Block Copolymers. *Nat. Mater.* **2004**, *3*, 823-828.
176. Glass, R.; Möller, M.; Spatz, J. P. Block Copolymer Micelle Nanolithography. *Nanotechnology* **2003**, *14*, 1153-1160.
177. Cheng, J. Y.; Rettner, C. T.; Sanders, D. P.; Kim, H.-C.; Hinsberg, W. D. Dense Self-Assembly on Sparse Chemical Patterns: Rectifying and Multiplying Lithographic Patterns Using Block Copolymers. *Adv. Mater.* **2008**, *20*, 3155-3158.
178. Stoykovich, M. P.; Kang, H.; Daoulas, K. C.; Liu, G.; Liu, C.-C.; de Pablo, J. J.; Mueller, M.; Nealey, P. F. Directed Self-Assembly of Block Copolymers for Nanolithography: Fabrication of Isolated Features and Essential Integrated Circuit Geometries. *ACS Nano* **2007**, *1*, 168-175.
179. Stoykovich, M. P.; Nealey, P. F. Block Copolymers and Conventional Lithography. *Mater. Today* **2006**, *9*, 20-29.
180. Hawker, C. J.; Russell, T. P. Block Copolymer Lithography: Merging "Bottom-up" with "Top-Down" Processes. *MRS Bull.* **2005**, *30*, 952-966.
181. Kim, S. O.; Solak, H. H.; Stoykovich, M. P.; Ferrier, N. J.; de Pablo, J. J.; Nealey, P. F. Epitaxial Self-Assembly of Block Copolymers on Lithographically Defined Nanopatterned Substrates. *Nature* **2003**, *424*, 411-414.
182. Glass, R.; Moller, M.; Spatz, J. P. Block Copolymer Micelle Nanolithography. *Nanotechnology* **2003**, *14*, 1153-1160.
183. Cheng, J. Y.; Ross, C. A.; Thomas, E. L.; Smith, H. I.; Vancso, G. J. Fabrication of Nanostructures with Long-Range Order Using Block Copolymer Lithography. *Appl.*

- Phys. Lett.* **2002**, *81*, 3657-3659.
184. Cheng, J. Y.; Ross, C. A.; Chan, V. Z. H.; Thomas, E. L.; Lammertink, R. G. H.; Vancso, G. J. Formation of a Cobalt Magnetic Dot Array *via* Block Copolymer Lithography. *Adv. Mater.* **2001**, *13*, 1174-1178.
185. Qin, D.; Xia, Y.; Whitesides, G. M. Soft Lithography for Micro-and Nanoscale Patterning. *Nat. Protoc.* **2010**, *5*, 491-502.
186. Kim, D. H.; Lee, H.; Lee, Y. K.; Nam, J. M.; Levchenko, A. Biomimetic Nanopatterns as Enabling Tools for Analysis and Control of Live Cells. *Adv. Mater.* **2010**, *22*, 4551-4566.
187. Hakim, M. M.; Lombardini, M.; Sun, K.; Giustiniano, F.; Roach, P. L.; Davies, D. E.; Howarth, P. H.; de Planque, M. R.; Morgan, H.; Ashburn, P. Thin Film Polycrystalline Silicon Nanowire Biosensors. *Nano Lett.* **2012**, *12*, 1868-1872.
188. Trompoukis, C.; El Daif, O.; Depauw, V.; Gordon, I.; Poortmans, J. Photonic Assisted Light Trapping Integrated in Ultrathin Crystalline Silicon Solar Cells by Nanoimprint Lithography. *Appl. Phys. Lett.* **2012**, *101*, 103901.
189. Hahn, M. S.; Taite, L. J.; Moon, J. J.; Rowland, M. C.; Ruffino, K. A.; West, J. L. Photolithographic Patterning of Polyethylene Glycol Hydrogels. *Biomaterials* **2006**, *27*, 2519-2524.
190. Hu, W. C.; Sarveswaran, K.; Lieberman, M.; Bernstein, G. H. Sub-10 nm Electron Beam Lithography Using Cold Development of Poly(Methylmethacrylate). *J. Vac. Sci. Technol. B* **2004**, *22*, 1711-1716.

191. Hong, S.; Zhu, J.; Mirkin, C. A. Multiple Ink Nanolithography: Toward a Multiple-Pen Nano-Plotter. *Science* **1999**, *286*, 523-525.
192. Stoykovich, M. P.; Muller, M.; Kim, S. O.; Solak, H. H.; Edwards, E. W.; de Pablo, J. J.; Nealey, P. F. Directed Assembly of Block Copolymer Blends into Nonregular Device-Oriented Structures. *Science* **2005**, *308*, 1442-1446.
193. Mann, S. Self-Assembly and Transformation of Hybrid Nano-Objects and Nanostructures under Equilibrium and Non-Equilibrium Conditions. *Nat. Mater.* **2009**, *8*, 781-792.
194. *International Technology Roadmap for Semiconductors*. 2013 ed.; Semiconductor Industry Association: San Jose CA, 2013.
195. Bates, C. M.; Maher, M. J.; Janes, D. W.; Ellison, C. J.; Willson, C. G. Block Copolymer Lithography. *Macromolecules* **2013**, *47*, 2-12.
196. Shin, D. O.; Mun, J. H.; Hwang, G.-T.; Yoon, J. M.; Kim, J. Y.; Yun, J. M.; Yang, Y.-B.; Oh, Y.; Lee, J. Y.; Shin, J. Multicomponent Nanopatterns by Directed Block Copolymer Self-Assembly. *ACS Nano* **2013**, *7*, 8899-8907.
197. Ross, C. A.; Berggren, K. K.; Cheng, J. Y.; Jung, Y. S.; Chang, J. B. Three-Dimensional Nanofabrication by Block Copolymer Self-Assembly. *Adv. Mater.* **2014**, *26*, 4386-4396.
198. Lohmueller, T.; Bock, E.; Spatz, J. P. Synthesis of Quasi-Hexagonal Ordered Arrays of Metallic Nanoparticles with Tuneable Particle Size. *Adv. Mater.* **2008**, *20*, 2297-2302.

199. Liu, C.-C.; Ramírez-Hernández, A.; Han, E.; Craig, G. S.; Tada, Y.; Yoshida, H.; Kang, H.; Ji, S.; Gopalan, P.; de Pablo, J. J. Chemical Patterns for Directed Self-Assembly of Lamellae-Forming Block Copolymers with Density Multiplication of Features. *Macromolecules* **2013**, *46*, 1415-1424.
200. Jung, H.; Hwang, D.; Kim, E.; Kim, B.-J.; Lee, W. B.; Poelma, J. E.; Kim, J.; Hawker, C. J.; Huh, J.; Ryu, D. Y. Three-Dimensional Multilayered Nanostructures with Controlled Orientation of Microdomains from Cross-Linkable Block Copolymers. *ACS Nano* **2011**, *5*, 6164-6173.
201. Gu, W.; Zhao, H.; Wei, Q.; Coughlin, E. B.; Theato, P.; Russell, T. P. Line Patterns from Cylinder-Forming Photocleavable Block Copolymers. *Adv. Mater.* **2013**, *25*, 4690-4695.
202. Bosworth, J. K.; Paik, M. Y.; Ruiz, R.; Schwartz, E. L.; Huang, J. Q.; Ko, A. W.; Smilgies, D.-M.; Black, C. T.; Ober, C. K. Control of Self-Assembly of Lithographically Patternable Block Copolymer Films. *ACS Nano* **2008**, *2*, 1396-1402.
203. Black, C. T.; Ruiz, R.; Breyta, G.; Cheng, J. Y.; Colburn, M. E.; Guarini, K. W.; Kim, H.-C.; Zhang, Y. Polymer Self Assembly in Semiconductor Microelectronics. *IBM J. Res. Dev.* **2007**, *51*, 605-633.
204. He, C.; Stoykovich, M. P. Profile Control in Block Copolymer Nanostructures Using Bilayer Thin Films for Enhanced Pattern Transfer Processes. *Adv. Funct. Mater.* **2014**, *24*, 7078-7084.

205. Jung, Y. S.; Ross, C. A. Solvent-Vapor-Induced Tunability of Self-Assembled Block Copolymer Patterns. *Adv. Mater.* **2009**, *21*, 2540-2545.
206. Herr, D. J. C. Directed Block Copolymer Self-Assembly for Nanoelectronics Fabrication. *J. Mater. Res.* **2011**, *26*, 122-139.
207. Aizawa, M.; Buriak, J. M. Block Copolymer-Templated Chemistry on Si, Ge, InP, and GaAs Surfaces. *J. Am. Chem. Soc.* **2005**, *127*, 8932-8933.
208. Huang, Y.; Kim, T. W.; Xiong, S.; Mawst, L. J.; Kuech, T. F.; Nealey, P. F.; Dai, Y.; Wang, Z.; Guo, W.; Forbes, D. Inas Nanowires Grown by Metal–Organic Vapor-Phase Epitaxy (MOVPE) Employing Ps/Pmma Diblock Copolymer Nanopatterning. *Nano Lett.* **2013**, *13*, 5979-5984.
209. Kuech, T. F.; Mawst, L. J. Nanofabrication of III–V Semiconductors Employing Diblock Copolymer Lithography. *J. Phys. D: Appl. Phys.* **2010**, *43*, 183001.
210. Ji, S.; Liu, C.-C.; Liu, G.; Nealey, P. F. Molecular Transfer Printing Using Block Copolymers. *ACS Nano* **2009**, *4*, 599-609.
211. Deng, X.; Buriak, J. M.; Dai, P.-X.; Wan, L.-J.; Wang, D. Block Copolymer-Templated Chemical Nanopatterning on Pyrolyzed Photoresist Carbon Films. *Chem. Commun.* **2012**, *48*, 9741-9743.
212. Snow, E.; Campbell, P. Afm Fabrication of Sub-10-Nanometer Metal-Oxide Devices with in Situ Control of Electrical Properties. *Science* **1995**, *270*, 1639-1641.
213. Aronsson, B. O.; Lausmaa, J.; Kasemo, B. Glow Discharge Plasma Treatment for Surface Cleaning and Modification of Metallic Biomaterials. *J. Biomedical Mater.*

- Res.* **1997**, *35*, 49-73.
214. Øiseth, S. K.; Krozer, A.; Kasemo, B.; Lausmaa, J. Surface Modification of Spin-Coated High-Density Polyethylene Films by Argon and Oxygen Glow Discharge Plasma Treatments. *Appl. Surf. Sci.* **2002**, *202*, 92-103.
215. Shirley, D. A. High-Resolution X-Ray Photoemission Spectrum of the Valence Bands of Gold. *Phys.Rev. B* **1972**, *5*, 4709-4709.
216. Linford, M. R.; Chidsey, C. E. D. Alkyl Monolayers Covalently Bonded to Silicon Surfaces. *J. Am. Chem. Soc.* **1993**, *115*, 12631-12632.
217. Chatgililoglu, C. Structural and Chemical-Properties of Silyl Radicals. *Chem. Rev.* **1995**, *95*, 1229-1251.
218. Stewart, M. P.; Buriak, J. M. Exciton-Mediated Hydrosilylation on Photoluminescent Nanocrystalline Silicon. *J. Am. Chem. Soc.* **2001**, *123*, 7821-7830.
219. Wang, X.; Ruther, R. E.; Streifer, J. A.; Hamers, R. J. UV-Induced Grafting of Alkenes to Silicon Surfaces: Photoemission Versus Excitons. *J. Am. Chem. Soc.* **2010**, *132*, 4048-4049.
220. Gooding, J. J.; Ciampi, S. The Molecular Level Modification of Surfaces: From Self-Assembled Monolayers to Complex Molecular Assemblies. *Chem. Soc. Rev.* **2011**, *40*, 2704-2718.
221. Stein, J.; Lewis, L. N.; Gao, Y.; Scott, R. A. In Situ Determination of the Active Catalyst in Hydrosilylation Reactions Using Highly Reactive Pt(0) Catalyst Precursors. *J. Am. Chem. Soc.* **1999**, *121*, 3693-3703.

222. Lewis, L. N.; Lewis, N. Platinum-Catalyzed Hydrosilylation - Colloid Formation as the Essential Step. *J. Am. Chem. Soc.* **1986**, *108*, 7228-7231.
223. Diez-Gonzalez, S.; Nolan, S. P. Copper, Silver, and Gold Complexes in Hydrosilylation Reactions. *Acc. Chem. Res.* **2008**, *41*, 349-358.
224. Buriak, J. M. Organometallic Chemistry on Silicon and Germanium Surfaces. *Chem. Rev.* **2002**, *102*, 1271-1308.
225. Buriak, J. M. Illuminating Silicon Surface Hydrosilylation: An Unexpected Plurality of Mechanisms. *Chem. Mater.* **2014**, *26*, 763-772.
226. Sieval, A.; Demirel, A.; Nissink, J.; Linford, M.; Van der Maas, J.; De Jeu, W.; Zuilhof, H.; Sudhölter, E. Highly Stable Si-C Linked Functionalized Monolayers on the Silicon (100) Surface. *Langmuir* **1998**, *14*, 1759-1768.
227. Linford, M. R.; Fenter, P.; Eisenberger, P. M.; Chidsey, C. E. Alkyl Monolayers on Silicon Prepared from 1-Alkenes and Hydrogen-Terminated Silicon. *J. Am. Chem. Soc.* **1995**, *117*, 3145-3155.
228. Zhong, Y. L.; Bernasek, S. L. Mild and Efficient Functionalization of Hydrogen-Terminated Si (111) via Sonochemical Activated Hydrosilylation. *J. Am. Chem. Soc.* **2011**, *133*, 8118-8121.
229. Scheres, L.; Giesbers, M.; Zuilhof, H. Self-Assembly of Organic Monolayers onto Hydrogen-Terminated Silicon: 1-Alkynes Are Better Than 1-Alkenes. *Langmuir* **2010**, *26*, 10924-10929.
230. Boukherroub, R.; Petit, A.; Loupy, A.; Chazalviel, J.-N.; Ozanam, F. Microwave-

- Assisted Chemical Functionalization of Hydrogen-Terminated Porous Silicon Surfaces. *J. Phys. Chem. B* **2003**, *107*, 13459-13462.
231. Buriak, J. M.; Stewart, M. P.; Geders, T. W.; Allen, M. J.; Choi, H. C.; Smith, J.; Raftery, D.; Canham, L. T. Lewis Acid Mediated Hydrosilylation on Porous Silicon Surfaces. *J. Am. Chem. Soc.* **1999**, *121*, 11491-11502.
232. Buriak, J. M.; Allen, M. J. Lewis Acid Mediated Functionalization of Porous Silicon with Substituted Alkenes and Alkynes. *J. Am. Chem. Soc.* **1998**, *120*, 1339-1340.
233. Bateman, J. E.; Eagling, R. D.; Worrall, D. R.; Horrocks, B. R.; Houlton, A. Alkylation of Porous Silicon by Direct Reaction with Alkenes and Alkynes. *Angew. Chem. Int. Ed.* **1998**, *37*, 2683-2685.
234. Michalak, D. J.; Amy, S. R.; Aureau, D.; Dai, M.; Estève, A.; Chabal, Y. J. Nanopatterning Si (111) Surfaces as a Selective Surface-Chemistry Route. *Nat. Mater.* **2010**, *9*, 266-271.
235. Wong, K. T.; Lewis, N. S. What a Difference a Bond Makes: The Structural, Chemical, and Physical Properties of Methyl-Terminated Si(111) Surfaces. *Acc. Chem. Res.* **2014**, *47*, 3037-3044.
236. Yang, Z.; Iqbal, M.; Dobbie, A. R.; Veinot, J. G. Surface-Induced Alkene Oligomerization: Does Thermal Hydrosilylation Really Lead to Monolayer Protected Silicon Nanocrystals? *J. Am. Chem. Soc.* **2013**, *135*, 17595-17601.
237. Wang, X.; Landis, E. C.; Franking, R.; Hamers, R. J. Surface Chemistry for Stable and Smart Molecular and Biomolecular Interfaces *via* Photochemical Grafting of

Alkenes. *Acc. Chem. Res.* **2010**, *43*, 1205-1215.

238. Terry, J.; Linford, M. R.; Wigren, C.; Cao, R.; Pianetta, P.; Chidsey, C. E. Determination of the Bonding of Alkyl Monolayers to the Si (111) Surface Using Chemical-Shift, Scanned-Energy Photoelectron Diffraction. *Appl. Phys. Lett.* **1997**, *71*, 1056-1058.
239. Terry, J.; Linford, M. R.; Wigren, C.; Cao, R.; Pianetta, P.; Chidsey, C. E. Alkyl-Terminated Si (111) Surfaces: A High-Resolution, Core Level Photoelectron Spectroscopy Study. *J. Appl. Phys.* **1999**, *85*, 213-221.
240. Cicero, R. L.; Linford, M. R.; Chidsey, C. E. Photoreactivity of Unsaturated Compounds with Hydrogen-Terminated Silicon (111). *Langmuir* **2000**, *16*, 5688-5695.
241. Khung, Y. L.; Ngalim, S. H.; Scaccabarozi, A.; Narducci, D. Thermal and Uv Hydrosilylation of Alcohol-Based Bifunctional Alkynes on Si (111) Surfaces: How Surface Radicals Influence Surface Bond Formation. *Sci. Rep.* **2015**, *5*, 11299.
242. Huck, L. A.; Buriak, J. M. Uv-Initiated Hydrosilylation on Hydrogen-Terminated Silicon (111): Rate Coefficient Increase of Two Orders of Magnitude in the Presence of Aromatic Electron Acceptors. *Langmuir* **2012**, *28*, 16285-16293.
243. Stewart, M. P.; Buriak, J. M. Photopatterned Hydrosilylation on Porous Silicon. *Angew. Chem. Int. Ed.* **1998**, *37*, 3257-3260.
244. Huck, L. A.; Buriak, J. M. Toward a Mechanistic Understanding of Exciton-Mediated Hydrosilylation on Nanocrystalline Silicon. *J. Am. Chem. Soc.* **2012**, *134*,

489-497.

245. Stewart, M. P.; Buriak, J. M. Photopatterned Hydrosilylation on Porous Silicon. *Angew. Chem. Int. Ed.* **1998**, *37*, 3257-3260.
246. Buriak, J. M. Silicon-Carbon Bonds on Porous Silicon Surfaces. *Adv. Mater.* **1999**, *11*, 265-267.
247. Kolasinski, K. W. The Mechanism of Photohydrosilylation on Silicon and Porous Silicon Surfaces. *J. Am. Chem. Soc.* **2013**, *135*, 11408-11412.
248. Sun, Q. Y.; de Smet, L.; van Lagen, B.; Wright, A.; Zuilhof, H.; Sudholter, E. J. R. Covalently Attached Monolayers on Hydrogen Terminated Si(100): Extremely Mild Attachment by Visible Light. *Angew. Chem. Int. Ed.* **2004**, *43*, 1352-1355.
249. Sun, Q. Y.; de Smet, L.; van Lagen, B.; Giesbers, M.; Thune, P. C.; van Engelenburg, J.; de Wolf, F. A.; Zuilhof, H.; Sudholter, E. J. R. Covalently Attached Monolayers on Crystalline Hydrogen-Terminated Silicon: Extremely Mild Attachment by Visible Light. *J. Am. Chem. Soc.* **2005**, *127*, 2514-2523.
250. Eves, B. J.; Sun, Q.-Y.; Lopinski, G. P.; Zuilhof, H. Photochemical Attachment of Organic Monolayers onto H-Terminated Si (111): Radical Chain Propagation Observed *via* STM Studies. *J. Am. Chem. Soc.* **2004**, *126*, 14318-14319.
251. Sugimura, H.; Mo, S.; Yamashiro, K.; Ichii, T.; Murase, K. Photochemical Assembly of Gold Nanoparticle Arrays Covalently Attached to Silicon Surface Assisted by Localized Plasmon in the Nanoparticles. *J. Phys. Chem. C* **2013**, *117*, 2480-2485.
252. Strohmeier, B. R. Copper/Silver/Gold Alloy by XPS. *Surf. Sci. Spectra* **1994**, *3*, 175-

181.

253. Louette, P.; Bodino, F.; Pireaux, J.-J. Poly (Dimethyl Siloxane)(PDMS) XPS Reference Core Level and Energy Loss Spectra. *Surf. Sci. Spectra* **2005**, *12*, 38-43.
254. Li, Y.-h.; Wang, D.; Buriak, J. M. Molecular Layer Deposition of Thiol–Ene Multilayers on Semiconductor Surfaces. *Langmuir* **2009**, *26*, 1232-1238.
255. Jana, N. R.; Gearheart, L.; Murphy, C. J. Seeding Growth for Size Control of 5-40 nm Diameter Gold Nanoparticles. *Langmuir* **2001**, *17*, 6782-6786.
256. Li, J. T.; Cushing, S. K.; Meng, F. K.; Senty, T. R.; Bristow, A. D.; Wu, N. Q. Plasmon-Induced Resonance Energy Transfer for Solar Energy Conversion. *Nat. Photonics* **2015**, *9*, 601-607.
257. Clavero, C. Plasmon-Induced Hot-Electron Generation at Nanoparticle/Metal-Oxide Interfaces for Photovoltaic and Photocatalytic Devices. *Nat. Photonics* **2014**, *8*, 95-103.
258. Zhang, P.; Wang, T.; Gong, J. Mechanistic Understanding of the Plasmonic Enhancement for Solar Water Splitting. *Adv. Mater.* **2015**, *27*, 5328-5342.
259. van Dijk, L.; van de Groep, J.; Veldhuizen, L. W.; Di Vece, M.; Polman, A.; Schropp, R. E. Plasmonic Scattering Back Reflector for Light Trapping in Flat Nanocrystalline Silicon Solar Cells. *ACS Photonics* **2016**, *3*, 685-691.
260. Baek, S.-W.; Park, G.; Noh, J.; Cho, C.; Lee, C.-H.; Seo, M.-K.; Song, H.; Lee, J.-Y. Au@Ag Core-Shell Nanocubes for Efficient Plasmonic Light Scattering Effect in Low Bandgap Organic Solar Cells. *ACS Nano* **2014**, *8*, 3302-3312.

261. Baek, S.-W.; Noh, J.; Lee, C.-H.; Kim, B.; Seo, M.-K.; Lee, J.-Y. Plasmonic Forward Scattering Effect in Organic Solar Cells: A Powerful Optical Engineering Method. *Sci. Rep.* **2013**, *3*, 1726
262. Rotenberg, N.; Spasenović, M.; Krijger, T.; Le Feber, B.; de Abajo, F. G.; Kuipers, L. Plasmon Scattering from Single Subwavelength Holes. *Phys. Rev. Lett.* **2012**, *108*, 127402.
263. Mukherjee, S.; Zhou, L. A.; Goodman, A. M.; Large, N.; Ayala-Orozco, C.; Zhang, Y.; Nordlander, P.; Halas, N. J. Hot-Electron-Induced Dissociation of H<sub>2</sub> on Gold Nanoparticles Supported on SiO<sub>2</sub>. *J. Am. Chem. Soc.* **2014**, *136*, 64-67.
264. Sundararaman, R.; Narang, P.; Jermyn, A. S.; Goddard III, W. A.; Atwater, H. A. Theoretical Predictions for Hot-Carrier Generation from Surface Plasmon Decay. *Nat. Commun.* **2014**, *5*, 5788.
265. Mukherjee, S.; Libisch, F.; Large, N.; Neumann, O.; Brown, L. V.; Cheng, J.; Lassiter, J. B.; Carter, E. A.; Nordlander, P.; Halas, N. J. Hot Electrons Do the Impossible: Plasmon-Induced Dissociation of H<sub>2</sub> on Au. *Nano Lett.* **2012**, *13*, 240-247.
266. Fang, Z.; Zhen, Y.-R.; Neumann, O.; Polman, A.; García de Abajo, F. J.; Nordlander, P.; Halas, N. J. Evolution of Light-Induced Vapor Generation at a Liquid-Immersed Metallic Nanoparticle. *Nano Lett.* **2013**, *13*, 1736-1742.
267. Baffou, G.; Berto, P.; Urena, E. B.; Quidant, R.; Monneret, S.; Polleux, J.; Rigneault, H. Photoinduced Heating of Nanoparticle Arrays. *ACS Nano* **2013**, *7*, 6478-6488.

268. Neumann, O.; Urban, A. S.; Day, J.; Lal, S.; Nordlander, P.; Halas, N. J. Solar Vapor Generation Enabled by Nanoparticles. *ACS Nano* **2012**, *7*, 42-49.
269. Cushing, S. K.; Wu, N. Progress and Perspectives of Plasmon-Enhanced Solar Energy Conversion. *J. Phys. Chem. Lett.* **2016**, *7*, 666-675.
270. Li, J.; Cushing, S. K.; Zheng, P.; Meng, F.; Chu, D.; Wu, N. Plasmon-Induced Photonic and Energy-Transfer Enhancement of Solar Water Splitting by a Hematite Nanorod Array. *Nat. Commun.* **2013**, *4*, 2651.
271. Cushing, S. K.; Li, J.; Meng, F.; Senty, T. R.; Suri, S.; Zhi, M.; Li, M.; Bristow, A. D.; Wu, N. Photocatalytic Activity Enhanced by Plasmonic Resonant Energy Transfer from Metal to Semiconductor. *J. Am. Chem. Soc.* **2012**, *134*, 15033-15041.
272. Wang, M.; Bangalore Rajeeva, B.; Scarabelli, L.; Perillo, E. P.; Dunn, A.; Liz-Marzán, L. M.; Zheng, Y. Molecular-Fluorescence Enhancement via Blue-Shifted Plasmon-Induced Resonance Energy Transfer. *J. Phys. Chem. C* **2016**, *120*, 14820-14827.
273. You, J.; Li, X.; Xie, F. x.; Sha, W. E.; Kwong, J. H.; Li, G.; Choy, W. C.; Yang, Y. Surface Plasmon and Scattering-Enhanced Low-Bandgap Polymer Solar Cell by a Metal Grating Back Electrode. *Adv. Energy Mater.* **2012**, *2*, 1203-1207.
274. Tan, H.; Santbergen, R.; Smets, A. H.; Zeman, M. Plasmonic Light Trapping in Thin-Film Silicon Solar Cells with Improved Self-Assembled Silver Nanoparticles. *Nano Lett.* **2012**, *12*, 4070-4076.
275. Yang, X.; Chueh, C. C.; Li, C. Z.; Yip, H. L.; Yin, P.; Chen, H.; Chen, W. C.; Jen, A.

- K. Y. High-Efficiency Polymer Solar Cells Achieved by Doping Plasmonic Metallic Nanoparticles into Dual Charge Selecting Interfacial Layers to Enhance Light Trapping. *Adv. Energy Mater.* **2013**, *3*, 666-673.
276. Warren, S. C.; Thimsen, E. Plasmonic Solar Water Splitting. *Energy Environ. Sci.* **2012**, *5*, 5133-5146.
277. Kim, S.-S.; Na, S.-I.; Jo, J.; Kim, D.-Y.; Nah, Y.-C. Plasmon Enhanced Performance of Organic Solar Cells Using Electrodeposited Ag Nanoparticles. *Appl. Phys. Lett.* **2008**, *93*, 073307.
278. Burda, C.; Chen, X.; Narayanan, R.; El-Sayed, M. A. Chemistry and Properties of Nanocrystals of Different Shapes. *Chem. Rev.* **2005**, *105*, 1025-1102.
279. Jain, P. K.; Lee, K. S.; El-Sayed, I. H.; El-Sayed, M. A. Calculated Absorption and Scattering Properties of Gold Nanoparticles of Different Size, Shape, and Composition: Applications in Biological Imaging and Biomedicine. *J. Phys. Chem. B* **2006**, *110*, 7238-7248.
280. Rhoderick, E. H.; Williams, R. H. *Metal-Semiconductor Contacts*. Clarendon Press Oxford: 1988; Vol. 129.
281. Vickers, V. Model of Schottky Barrier Hot-Electron-Mode Photodetection. *Appl. Opt.* **1971**, *10*, 2190-2192.
282. Jia, C.; Li, X.; Xin, N.; Gong, Y.; Guan, J.; Meng, L.; Meng, S.; Guo, X. Interface-Engineered Plasmonics in Metal/Semiconductor Heterostructures. *Adv. Energy Mater.* **2016**, 1600431.

283. Shi, Y.; Wang, J.; Wang, C.; Zhai, T.-T.; Bao, W.-J.; Xu, J.-J.; Xia, X.-H.; Chen, H.-Y. Hot Electron of Au Nanorods Activates the Electrocatalysis of Hydrogen Evolution on MoS<sub>2</sub> Nanosheets. *J. Am. Chem. Soc.* **2015**, *137*, 7365-7370.
284. Li, J.; Cushing, S. K.; Zheng, P.; Senty, T.; Meng, F.; Bristow, A. D.; Manivannan, A.; Wu, N. Solar Hydrogen Generation by a CdS-Au-TiO<sub>2</sub> Sandwich Nanorod Array Enhanced with Au Nanoparticle as Electron Relay and Plasmonic Photosensitizer. *J. Am. Chem. Soc.* **2014**, *136*, 8438-8449.
285. DuChene, J. S.; Sweeny, B. C.; Johnston-Peck, A. C.; Su, D.; Stach, E. A.; Wei, W. D. Prolonged Hot Electron Dynamics in Plasmonic-Metal/Semiconductor Heterostructures with Implications for Solar Photocatalysis. *Angew. Chem. Int. Ed.* **2014**, *53*, 7887-7891.
286. Mubeen, S.; Lee, J.; Singh, N.; Kraemer, S.; Stucky, G. D.; Moskovits, M. An Autonomous Photosynthetic Device in Which All Charge Carriers Derive from Surface Plasmons. *Nat. Nanotechnol.* **2013**, *8*, 247-251.
287. Lee, J.; Mubeen, S.; Ji, X.; Stucky, G. D.; Moskovits, M. Plasmonic Photoanodes for Solar Water Splitting with Visible Light. *Nano Lett.* **2012**, *12*, 5014-5019.
288. Govorov, A. O.; Richardson, H. H. Generating Heat with Metal Nanoparticles. *Nano Today* **2007**, *2*, 30-38.
289. Anger, P.; Bharadwaj, P.; Novotny, L. Enhancement and Quenching of Single-Molecule Fluorescence. *Phys. Rev. Lett.* **2006**, *96*, 113002.
290. Lee, J.; Javed, T.; Skeini, T.; Govorov, A. O.; Bryant, G. W.; Kotov, N. A.

- Bioconjugated Ag Nanoparticles and Cdte Nanowires: Metamaterials with Field-Enhanced Light Absorption. *Angew. Chem. Int. Ed.* **2006**, *45*, 4819-4823.
291. Sil, D.; Gilroy, K. D.; Niaux, A.; Boulesbaa, A.; Neretina, S.; Borguet, E. Seeing Is Believing: Hot Electron Based Gold Nanoplasmonic Optical Hydrogen Sensor. *ACS Nano* **2014**, *8*, 7755-7762.
292. Schmid, M.; Grandidier, J.; Atwater, H. A. Scanning Near-Field Optical Microscopy on Dense Random Assemblies of Metal Nanoparticles. *J. Optics* **2013**, *15*, 125001.
293. Ozhikandathil, J.; Packirisamy, M. Simulation and Implementation of a Morphology-Tuned Gold Nano-Islands Integrated Plasmonic Sensor. *Sensors* **2014**, *14*, 10497-10513.
294. Lu, R.; Konzelmann, A.; Xu, F.; Gong, Y.; Liu, J.; Liu, Q.; Xin, M.; Hui, R.; Wu, J. Z. High Sensitivity Surface Enhanced Raman Spectroscopy of R6g on *in situ* Fabricated Au Nanoparticle/Graphene Plasmonic Substrates. *Carbon* **2015**, *86*, 78-85.
295. Skoog, D. A.; West, D. M. *Principles of Instrumental Analysis*. Saunders College Philadelphia: 1980; Vol. 158.
296. Dixon, J. M.; Taniguchi, M.; Lindsey, J. S. Photochemcad 2: A Refined Program with Accompanying Spectral Databases for Photochemical Calculations. *Photochem. Photobiol.* **2005**, *81*, 212-213.
297. Zhang, X.; Zhu, Y.; Yang, X.; Wang, S.; Shen, J.; Lin, B.; Li, C. Enhanced Visible Light Photocatalytic Activity of Interlayer-Isolated Triplex Ag@ SiO<sub>2</sub>@ TiO<sub>2</sub> Core-

- Shell Nanoparticles. *Nanoscale* **2013**, *5*, 3359-3366.
298. Toma, K.; Vala, M.; Adam, P.; Homola, J.; Knoll, W.; Dostálek, J. Compact Surface Plasmon-Enhanced Fluorescence Biochip. *Opt. Express* **2013**, *21*, 10121-10132.
299. Anger, P.; Bharadwaj, P.; Novotny, L. In *Enhancement and Quenching of Single Molecule Fluorescence near a Gold Nanoparticle*, Laser Science, Optical Society of America: 2005; p LTuC3.
300. McKay, K.; McAfee, K. Electron Multiplication in Silicon and Germanium. *Phys. Rev.* **1953**, *91*, 1079.
301. Wolff, P. Theory of Electron Multiplication in Silicon and Germanium. *Phys. Rev.* **1954**, *95*, 1415.
302. Maes, W.; De Meyer, K.; Van Overstraeten, R. Impact Ionization in Silicon: A Review and Update. *Solid-State Electron.* **1990**, *33*, 705-718.
303. Novotny, L.; Hecht, B. *Principles of Nano-Optics*. Cambridge university press: 2012.
304. Richter, A.; Glunz, S. W.; Werner, F.; Schmidt, J.; Cuevas, A. Improved Quantitative Description of Auger Recombination in Crystalline Silicon. *Phys. Rev. B* **2012**, *86*, 165202.
305. Gan, Q.; Bartoli, F. J.; Kafafi, Z. H. Plasmonic-Enhanced Organic Photovoltaics: Breaking the 10% Efficiency Barrier. *Adv. Mater.* **2013**, *25*, 2385-2396.
306. Li, X.; Choy, W. C.; Huo, L.; Xie, F.; Sha, W. E.; Ding, B.; Guo, X.; Li, Y.; Hou, J.; You, J. Dual Plasmonic Nanostructures for High Performance Inverted Organic Solar Cells. *Adv. Mater.* **2012**, *24*, 3046-3052.

307. Stratakis, E.; Kymakis, E. Nanoparticle-Based Plasmonic Organic Photovoltaic Devices. *Mater. Today* **2013**, *16*, 133-146.
308. Jana, N. R.; Gearheart, L.; Murphy, C. J. Seed-Mediated Growth Approach for Shape-Controlled Synthesis of Spheroidal and Rod-Like Gold Nanoparticles Using a Surfactant Template. *Adv. Mater.* **2001**, *13*, 1389-1393.
309. Lohmüller, T.; Iversen, L.; Schmidt, M.; Rhodes, C.; Tu, H.-L.; Lin, W.-C.; Groves, J. Single Molecule Tracking on Supported Membranes with Arrays of Optical Nanoantennas. *Nano Lett.* **2012**, *12*, 1717-1721.
310. Crut, A.; Maioli, P.; Del Fatti, N.; Vallee, F. Optical Absorption and Scattering Spectroscopies of Single Nano-Objects. *Chem. Soc. Rev.* **2014**, *43*, 3921-3956.
311. Chen, H.; Shao, L.; Li, Q.; Wang, J. Gold Nanorods and Their Plasmonic Properties. *Chem. Soc. Rev.* **2013**, *42*, 2679-2724.
312. Patoka, P.; Giersig, M. Self-Assembly of Latex Particles for the Creation of Nanostructures with Tunable Plasmonic Properties. *J. Mater. Chem.* **2011**, *21*, 16783-16796.
313. Wang, D.; Yang, A.; Hryn, A. J.; Schatz, G. C.; Odom, T. W. Superlattice Plasmons in Hierarchical Au Nanoparticle Arrays. *ACS Photonics* **2015**, *2*, 1789-1794.